Order N°: **Year: 2017/2018**

PEOPLE'S DEMOCRATIC REPUBLIC OF ALGERIA

MINISTRY OF HIGHER EDUCATION AND SCIENTIFIC RESEARCH

DJILLALI LIABES UNIVERSITY-SIDI BEL ABBES

Faculty of electrical Engineering

Electronics Department

THESIS

To obtain the degree of

DOCTOR OF SCIENCE

Doctoral school " **Materials and components** ".

OPTION

" **Materials and optoelectronics components** "

Presented by

Ms. BENZINA Amina

Theme

STUDY THE STRUCTURAL, ELECTRONIC AND OPTICAL PROPERTIES OF NEW NITRIDE MATERIAL AlGaInN BY THE AB-INITIO METHOD (FP-LAPW).

At / /2017 with the board of examiners:

Mr. M. ANANI	Professor at Sidi Bel-abbes University	President
Mr. A. LACHEBI	Professor at Sidi Bel-abbes University	Thesis Advisor
Mr. A. SHUHAIMI	Doctor at University Malaya, Malaysia	Thesis Co-Advisor
Mr. M. SAHNOUN	Professor at Mascara University	Examiner
Mr. O. ARBOUCHE	M.C.A at Saida University	Examiner
Mr. H. ABID	Professor at Sidi Bel-abbes University	Invited

الملخص

الهدف الرئيسي من هذه المذكرة يكمن في البحث عن مواد جديدة من فئة nitrides ,في البداية نتطرق لمعالجة الجانب النظري كدراسة اولية وذلك باستعمال طريقة الحساب بالموجات المنبسطة المتزايدة الخطية (FP-LAPW) في اطار نظرية الكثافة الوظيفية (DFT) حيث تم تنفيذها في برنامج المحاكاة WIEN2K لاستخدامها في جميع الأعمال المنجزة في هذه الأطروحة لدراسة مختلف الخصائص البنيوية، الإلكترونية وكذا البصرية للمركبات ذات الطبيعة البنيوية zinc-blende، الثنائية (GaN, AlN, InN)) الثلاثية $(Al_{1-y}Ga_yN)$والرباعية $Al_xGa_yIn_{1-x-y}N$ مطابقة على الركيزةAlN ، زيادة على دراسة الخصائص البنيوية والألكتروبصرية للمركبات الثلاثية $In_xGa_{1-x}N$ ذات الطبيعة البنيوية wurtzite المطابقة للركيزةGaN باستعمال supercell 16- ذرة. تقريب التدرج الذي طوره WU et Cohen (WC-GGA)، تقريب الكثافة المحلية (LDA) زيادة على امكانية التبادلBecke-Johnson المعدلة [F. Tran et P. Blaha] (TB-mBJ)طبقو لتحسين هيكل شريط الطاقة اضافة الى الخصائص البصرية للمركبات. تمت مقارنة النتائج التى تم الحصول عليها من خلال دراسات تطبيقية واعمال سابقة مدرجة بنظريات مختلفة.

القسم الثاني من هذه الاطروحة وهو التجريبي الذي يعتبر تطبيق للمواد المدروسة III/V ذات التركيبة البنيوية للثالثي $In_xGa_{1-x}N$ بواسطة خلية شمسية أنشأت بواسطة ترسب الابخرة الكيميائية المعدنية SR2000KS (MOCVD) ذات مفاعل افقي مصنعة من طرف Taiyo Nippon Sanso . الخلية الشمسية $InGaN/ GaN$ تنشأ على ركيزة سليكون 2- بوصة ذات (111) توجه بلوري .

تم إجراء المقطع العرضي باستخدام تقنية المسح الضوئي المجهري الإلكتروني(FESEM) وهذا لتأكيد التجانس بين الطبقات المنشاةعلى ركيزة السليكونSi (111) كطبقة النوىAlN ، متعدد الطبقات(ML) إضافة الى (MQW) متعدد الاحواض الكمية.

الكلمات المفتاحية : TB-mBJ, $Al_xGa_yIn_{1-x-y}N$, $In_xGa_{1-x}N$,MOCVD, خلية شمسية,FP-LAPW .

Abstract

In this thesis, the main objective is to investigate new nitrides materials, at first a theoretical part based on the full-potential linearized augmented plane wave method (FP-LAPW) based density functional theory (DFT) which was implemented in WIEN2K code employed throughout the work to investigate the structural, electronic and optical properties of the compound GaN, AlN, InN, ternary $Al_{1-y}Ga_yN$, and quaternary $Al_xGa_yIn_{1-x-y}N$ zinc-blende alloys matched on AlN substrate using 64-atom supercell. As well as the study of the structural and optoelectronic properties of the Wurtzite $In_xGa_{1-x}N$ matched on GaN substrate using 16-atom supercell.
The generalized gradient approximation of Wu and Cohen (WC-GGA), the standard local density approach (LDA) and the modified Becke-Johnson exchange potential [F. Tran and P. Blaha] (TB-mBJ) were applied to improve the band structure and optical properties for the compounds. Whenever conceivable, we compare the obtained results by experiments and computations performed with diverse computational schemes.
The second part is the experiment which is the application of the wurtzite structure III/V nitride ternary alloys $In_xGa_{1-x}N$, by a solar cell grown by metal-organic chemical vapor deposition (MOCVD) equipment SR2000KS with a horizontal reactor manufactured by Taiyo Nippon Sanso. The $InGaN/ GaN$ solar cells structures were growth on 2-inch Si substrate with (111)-crystal orientation.

Cross-section scanning using field effect scanning electron microscopy (FESEM) technique was conducted to further confirm the homogeneity of grown the AlN nucleation layer, multi-layer (ML) and multi quantum well (MQW) on Si (111) substrate.

Key words: TB-mBJ, $Al_xGa_yIn_{1-x-y}N$, $In_xGa_{1-x}N$, MOCVD, solar cell, FP-LAPW.

Résumé

Dans cette thèse, l'objectif principal est d'étudier de nouveaux matériaux de nitrures, d'abord une partie théorique basée sur la méthode des ondes planes augmentées linéarisées (FP-LAPW) dans le cadre de la théorie de la densité fonctionnelle (DFT), a été implémentée dans le code WIEN2K dans tous les travaux accomplis de cette thèse afin d'examiner les différentes propriétés structurelles, électroniques et optiques des composants pour une structure zinc-blende des binaires (GaN, AlN, InN), ternaires ($Al_{1-y}Ga_yN$) et quaternaires $Al_xGa_yIn_{1-x-y}N$ croître sur un substrat AlN, ainsi qu'une étude des propriétés structurales et optoélectroniques de l'alliage ternaire $In_xGa_{1-x}N$, pour une structure wurtzite de 16 atomes croître sur un substrat GaN . L'approximation du gradient généralisée développée par WU et Cohen (WC-GGA), l'approximation de la densité locale (LDA) et le potentiel d'échange de Becke-Johnson modifié [F. Tran et P. Blaha] (TB-mBJ), ont été appliqués pour améliorer la structure de bande et les propriétés optiques pour les composés, en comparant les résultats obtenus par d'autres expérimentaux et des calculs effectués avec divers méthodes de calculs.

La deuxième partie est l'expérimentale qui est l'application des nitrures III/V en structure wurtzite de l'alliage ternaire $In_xGa_{1-x}N$ par une cellule solaire épitaxié par l'équipement de l'épitaxie en phase vapeur aux organométalliques (MOCVD) SR2000KS réacteur fabriqué par Taiyo Nippon Sanso. La croissance de la cellule solaire $InGaN/ GaN$ sur un substrat en Silicium (Si) de 2-pouces pour une orientation cristalline (111).

Analyse de section transversale en utilisant la technique de Microscopie électronique à balayage à émission de champ (FESEM) a été menée pour confirmer de plus l'homogénéité des couches épitaxies, la couche de nucléation AlN, multicouches (ML) et les puits multi-quantiques (MQW) sur le substrat Si (111).

Mots clés : TB-mBJ, $Al_xGa_yIn_{1-x-y}N$, $In_xGa_{1-x}N$, MOCVD, cellule solaire, FP-LAPW.

Dedication

To

The soul of My father

My mother

To my brothers and sisters

To my nephews: Aymen, Nour, Douae,

Abderrahmane and Farouk

To all my professors and teachers

To all my friends and colleagues

Acknowledgments

This thesis has been carried out at the Applied Materials Laboratory (AML), Faculty of Electrical engineering, Djillali Liabes University – Sidi Bel Abbes, under the supervision of prof. Abdelhadi LACHEBI.

First and foremost, praises and thanks go to Allah, the Almighty, for his unlimited and uncountable blessings in my whole life and throughout my research work especially.

I wish to express my sincere gratitude and deep indebtedness to my research supervisor, Professor Abdelhadi LACHABI from University Djillali Liabes of Sidi Bel Abess, for giving me the opportunities to have a very interesting research works in Nitride semiconductor field, for his permanent follow-up, his attentive readings like for his confidence and the liberty that he has left me during these years of research.

I am especially grateful and would like to express my very great appreciation, deep gratitude and sincere thanks to Prof. Datin Dr. Saadah Binti abdul Rahman, Head of Low Dimensional Materials Research Centre (LDMRC), Department of Physics, Faculty of Science, University of Malaya, for her help, I have been extremely lucky to have accepted me in (LDMRC) and sent me the Offer Letter form University Malaya as a non-graduating student (research), for her time that she has provided to me throughout my preparation before my visit to LDMRC, thank you my professor for everything you have done for me 'Terima kasih banyak'.

I hold to express my deep gratitude to Dr. Ahmad SHUHAIMI from Low Dimensional Materials Research Centre (LDMRC), Department of Physics, Faculty of Science, University of Malaya, for his sincere guidance and valuable comments and to learn from his valuable expertise and to have the fruitful discussions with him.

Besides my supervisor, I would like also to offer my thanks to the thesis committee for reviewing my thesis and giving their insightful and useful comments.

Special thanks are to Professor Macho ANANI from University of Sidi Bel Abbess to have accepted to chair the jury of this thesis.

I hold to present my thanks to Professor Mohamed SAHNOUN, from the University of Mascara, Dr. Omar ARBOUCHE lecturer at University of Saida, that makes me an honor to judge this thesis.

I thank particularly Professor Hamza ABID at University of Sidi Bel Abbes, Director of Applied Materials Laboratory to accept the invitation.

I also wish to appreciate all ex-members and colleagues from Applied Materials Laboratory as well as Low Dimensional Materials Research Centre (LDMRC), especially to Silicon team for their collaboration and guidance on InGaN-based solar cells growth.

I am also grateful to University Djillali Liabes (UDL), Algeria, and Ministry of Higher Education, Algeria, for financial support to accomplish my study at Low Dimensional Materials Research Centre (LDMRC), Department of Physics, Faculty of Science, University of Malaya, Malaysia.

At last, I would like to thank my family members, friends and well-wishers for their constant hearty support and encouragements.

CONTENTS

Contents

NOMENCLATURE i

LIST OF FIGURES iii

LIST OF TABLES vi

GENERAL INTRODUCTION 1

1. General properties of nitrides

1.1 INTRODUCTION 8

1.2 DEFINITION OF GROUP III-NITRIDE SEMICONDUCTORS 8

1.3 CRYSTAL STRUCTURE OF NITRIDES 8

1.3.1 THE ZINC-BLENDE STRUCTURE 9

1.3.2 THE WURTZITE STRUCTURE 10

1.4 BRILLOUIN ZONE 10

1.5 ENERGY-BAND STRUCTURE 12

1.6 THE ALLOYS 13

1.6.1 ALLOY DEFINITION 13

1.6.2 ALLOYS CLASSIFICATION 14

1.6.2.1BINARY ALLOYS 14

1.6.2.2 TERNARY ALLOYS 15

2.6.2.3 QUATERNARY ALLOYS 16

1.7 APPLICATIONS OF III-NITRIDES FOR OPTOELECTRONICS 17

1.7.1 ULTRAVIOLET PHOTODETECTORS 17

1.7.2 VISIBLE LIGHT EMITTING DIODES 18

1.7.3 LASER DIODES 19

1.7.4 SOLAR CELLS 20

1.8 CONCLUSION 20

REFERENCES 21

2. Density Functional Theory

2.1 INTRODUCTION…….. 25

2.2 DEFINITION OF DFT…... 25

2.3 EQUATION OF SCHRÖDINGER…… 26

2.4 ESSENTIAL ASPECTS OF DFT…… 27

2.5 EXCHANGE-CORRELATION POTENTIALS…… 28

2.5.1 THE LOCAL DENSITY APPROXIMATION (LDA)…… 28

2.5.2 THE GENERALIZED GRADIENT APPROXIMATION (GGA)…….. 29

2.6 SOLVING THE KOHN-SHAM EQUATIONS…… 30

2.7 BASIS FUNCTIONS FOR DFT…….. 30

2.7.1 PSEUDOPOTENTIAL METHODS…… 30

2.7.2 FULL-POTENTIAL PLANE WAVE METHODS…….. 31

2.8 OUR USE OF DFT CALCULATIONS IN OUR OWN RESEARCH…….. 32

2.9 THE WIEN2K CODE APPROACH…… 33

2.10 CONCLUSIONS…….. 35

REFERENCES …… 36

3. The properties of the zinc-blende $AlGaInN$ alloys

3.1 INTRODUCTION…….. 38

3.2 COMPUTATIONAL DETAIL…….. 38

3.3 RESULTS AND DISCUSSION…… 39

3.3.1 STRUCTURAL PROPERTIES…… 39

3.3.2 ELECTRONIC PROPERTIES…….. 43

3.3.2.1 BAND STRUCTURE…… 43

3.3.2 .2 DENSITIES OF STATES DOS…….. 48

a. FOR THE TERNARY…... 48

b. FOR THE QUATERNARY…… 50

3.3.3 OPTICAL PROPERTIES…… 51

3.4 CONCLUSION…….. 59

REFERENCES …… 60

4. The properties of the wurtzite $InGaN$ alloys

4.1 INTRODUCTION........ 64

4.2 COMPUTATIONAL DETAIL........ 64

4.3 RESULTS AND DISCUSSION........ 66

4.3.1 STRUCTURAL PROPERTIES........ 66

4.3.2 ELECTRONIC PROPERTIES........ 68

4.3.3 OPTICAL PROPERTIES........ 73

4.4 CONCLUSION........ 79

REFERENCES........ 80

5. Experimental techniques and device fabrication process

5.1 INTRODUCTION........ 84

5.2 METAL ORGANIC CHEMICAL VAPOR DEPOSITION (MOCVD)........ 84

5.3 MOCVD SYSTEMS FOR PRODUCTION........ 85

5.4 THIN FILMS DEPOSITION........ 87

5.4.1 SUBSTRATE CLEANING........ 87

5.4.1.1 ORGANIC CLEANING METHOD........ 87

5.4.1.2 RADIO CORPORATION OF AMERICA STANDARD CLEANING METHOD........ 87

5.4.1.3 HYDROFLUORIC ACID (HF) DIPPING METHOD........ 88

5.4.2 HYDROGEN CLEANING (BAKING)........ 89

5.4.3 CONTROLLED PRELIMINARY GROWTH OF GAN ON SI (111) SUBSTRATES........ 89

5.5 THE BULK $InGaN$ SOLAR CELL........ 90

5.5.1 GROWTH CONDITION........ 90

5.5.2 SAMPLE CHARACTERIZATION........ 91

5.6 THE SEMI-BULK $InGaN$ SOLAR CELL........ 94

5.6.1 GROWTH CONDITION........ 94

5.6.2 SAMPLE CHARACTERIZATION........ 95

5.7 CONCLUSION........ 97

REFERENCES........ 98

GENERAL CONCLUSION........ 99

NOMENCLATURE

Nomenclature

UV	Ultra violet
GaN	Gallium nitride
InN	Indium nitride
AlN	Aluminum nitride
Si	Silicon
LED	light emitting diode
LD	laser diode
$GaAs$	Gallium Arsenide
InP	Indium Phosphide
NIR	Near-infra-red
IR	Infra-red
nm	Nanometer
DVD	Digital versatile disc
eV	Electronvolt
DUV	Deep ultra violet
$InGaN$	Indium Gallium nitride
$AlGaInN$	Aluminum Gallium Indium nitride
BD	Blue-ray Disc
PV	Photovoltaic devices
In	Indium
m_e^*	Electron effective mass
μ_e	High electron mobility
$Al_{1-y}Ga_yN$	Aluminum Gallium nitride
DFT	Density functional theory
WIEN2K code	Computer program written in Fortran
$AlInN$	Aluminum Indium nitride
MQW	Multiple quantum well
DOS	Density of states
FP-LAPW	Full-potential linearized augmented plane wave method
MOCVD	Metal-organic chemical vapour deposition
$InAlN$	Indium Aluminum Nitride
BN	Boron Nitride
BP	Boron Phosphide
BAs	Boron Arsenide
AlP	Aluminum Phosphide
$AlAs$	Aluminum Arsenide
$AlSb$	Aluminum Antimony

$GaSb$	Gallium Antimony
$InAs$	Indium Arsenide
$InSb$	Arsenide antimony
$SiO2$	Silicon dioxide
MgO	Magnesium Oxide
ZB	Zinc blende structure
Wz	Wurtzite structure
fcc	Face-centered cubic
hcp	Hexagonal close-packed
Ec	Conduction band
Ev	Valence band
DBR	Distributed Bragg reflector
GGA	Generalized Gradient Approximation
LDA	Local-Density Approximation
DOS	Density of States
PDOS	Partial Density of States
LAPW	Linearized Augmented Plane Wave
TB-mBJ	The modified Becke-Johnson exchange potential
MT	Muffin-Tin
RMT	The Radius of Muffin-Tin
$Kmax$	largest K vector in the plane wave expansion
E_g	The energy band gap
BZ	Brillouin zone
$\varepsilon(\omega)$	The dielectric function
$\varepsilon_1(\omega)$	The real dielectric function
$\varepsilon_2(\omega)$	The imaginary dielectric function
$\alpha(\omega)$	The absorption coefficient
$R(\omega)$	The reflectivity coefficient
$n(\omega)$	The refractive index coefficient
$k(\omega)$	The extinction coefficient

LISTS OF FIGURES

Lists of figures

Figure.1.1 Atomic positions in zinc- blende(a) and wurtzite crystal(b)………………… 9

Figure.1.2 Miller indices of some important planes in a cubic crystal………………….. 11

Figure.1.3 (a) Brillouin zone for diamond and zinc-blende lattices, (b) Brillouin zone for wurtzite ……………………………………………………………... 12

Figure.1.4 The reduced-zone representation…………………………………………….. 13

Figure.1.5 AB semiconductor compounds with the zinc-blende structure………………. 14

Figure.1.6 (a) $A_xB_{1-x}C$ and (b) AB_xC_{1-x} Alloys with the zinc-blende structure……… 15

Figure.1.7 $A_xB_yC_{1-x-y}D$ alloys with the zinc-blende structure……………………… 16

Figure.2.1 Schematic representation of the muffin-tin scheme for full-potential plane wave bases……………………………………………………………………. 31

Figure.2.2 Flow chart of WIEN2k code………………………………………………… 34

Figure.3.1 Illustration of a 1×1×1 conventional zinc-blende cell: (a) AlN, (b) GaN and (c) InN……………………………………………………………………... 38

Figure.3.2 Illustration of a 2×2×2 zinc blende $Al_{0.343}Ga_{0.625}In_{0.031}N$ supercell, also for the other structure…………………………………………………………….. 39

Figure.3.3 Total energy of AlN, GaN and InN as a function of volume………………….. 40-41

Figure.3.4 Total energy of $Al_{0.375}Ga_{0.625}N$, $Al_{0.5}Ga_{0.5}N$ and $Al_{0.625}Ga_{0.375}N$as a function of volume……………………………………………………………. 41

Figure.3.5 Total energy of $Al_{0.343}Ga_{0.625}In_{0.031}N$, $Al_{0.468}Ga_{0.5}In_{0.031}N$ and $Al_{0.593}Ga_{0.25}In_{0.031}N$ as a function of volume……………………………… 42

Figure.3.6 Band structures within TB-mBJ at the lattice constant for (a) $Al_{0.375}Ga_{0.625}N$, (b) $Al_{0.5}Ga_{0.5}N$ and (c) $Al_{0.625}Ga_{0.375}N$……………………………………... 46

Figure.3.7 Band structures within TB-mBJ at the lattice constant for (a) $Al_{0.343}Ga_{0.625}In_{0.031}N$, (b) $Al_{0.468}Ga_{0.5}In_{0.031}N$ and (c) $Al_{0.593}Ga_{0.25}In_{0.031}N$……………………………………………………... 47

Figure.3.8 Total and partial densities of states for(a) $Al_{0.375}Ga_{0.625}N$, (b) $Al_{0.5}Ga_{0.5}N$ and (c) $Al_{0.625}Ga_{0.375}N$………………………………………………………. 49

Figure.3.9 Total and partial densities of states for (a) $Al_{0.343}Ga_{0.625}In_{0.031}N$, (b) $Al_{0.468}Ga_{0.5}In_{0.031}N$ and (c) $Al_{0.593}Ga_{0.25}In_{0.031}N$ compounds………… 50-51

Figure.3.10 Real part $\varepsilon_1(\omega)$ (a) and imaginary part $\varepsilon_2(\omega)$ (b) $Al_{0.375}Ga_{0.625}N$, $Al_{0.5}Ga_{0.5}N$ and $Al_{0.625}Ga_{0.375}N$ for compounds................................ 53

Figure.3.11 Real part $\varepsilon_1(\omega)$ (a) and imaginary part $\varepsilon_2(\omega)$ (b) for $Al_{0.343}Ga_{0.625}In_{0.031}N$, $Al_{0.468}Ga_{0.5}In_{0.031}N$ and $Al_{0.593}Ga_{0.25}In_{0.031}N$ compounds.................. 54

Figure.3.12 refractive index $n(\omega)$ (a) and reflectivity $R(\omega)$ (b) for$Al_{0.375}Ga_{0.625}N$, $Al_{0.5}Ga_{0.5}N$ and $Al_{0.625}Ga_{0.375}N$ for compounds................................ 56

Figure.3.13 refractive index $n(\omega)$ (a) and reflectivity $R(\omega)$ (b) for $Al_{0.343}Ga_{0.625}In_{0.031}N$, $Al_{0.468}Ga_{0.5}In_{0.031}N$ and $Al_{0.593}Ga_{0.25}In_{0.031}N$ compounds.. 57

Figure.3.14 Absorption coefficient *α(ω)* for $Al_{0.375}Ga_{0.625}N$, $Al_{0.5}Ga_{0.5}N$ and $Al_{0.625}Ga_{0.375}N$ for compounds... 58

Figure.3.15 Absorption coefficient *α(ω)*for $Al_{0.343}Ga_{0.625}In_{0.031}N$, $Al_{0.468}Ga_{0.5}In_{0.031}N$ and $Al_{0.593}Ga_{0.25}In_{0.031}N$ compounds... 58

Figure.4.1 Illustration of a 1×1×1 conventional hexagonal cell- wurtzite: (a) InN and (b) GaN... 64

Figure.4.2 Illustration of a 2×2×2 wurtzite $In_{0,375}Ga_{0,625}N$ supercell..................... 65

Figure.4.3 Total energies as a function of volume for the InN and GaN for zb and wz phases.. 66

Figure.4.4 Band structures within TB-mBJ for (a)$In_{0,125}Ga_{0,875}N$, (b) $In_{0,375}Ga_{0,625}N$,(c) $In_{0,625}Ga_{0,375}N$ and (d) $In_{0,875}Ga_{0,125}N$ 69-70

Figure.4.5 Band gap energy as a function of Indium concentration.......................... 70

Figure.4.6 Total and partial densities of states for (a) $In_{0,125}Ga_{0,875}N$, (b) $In_{0,375}Ga_{0,625}N$, (c) $In_{0,625}Ga_{0,375}N$ and (d) $In_{0,875}Ga_{0,125}N$ compounds.. 71-73

Figure.4.7 Real part *ε₁(ω)* (a) and imaginary part *ε₂(ω)* (b) for $In_{0,125}Ga_{0,875}N$, $In_{0,375}Ga_{0,625}N$, $In_{0,625}Ga_{0,375}N$ and $In_{0,875}Ga_{0,125}N$ 75

Figure.4.8 reflectivity $R(\omega)$ (a) and (b) refractive index $n(\omega)$ for $In_{0,125}Ga_{0,875}N$, $In_{0,375}Ga_{0,625}N$, $In_{0,625}Ga_{0,375}N$ and $In_{0,875}Ga_{0,125}N$ 77

Figure.4.9 Absorption coefficient *α(ω)*for $In_{0,125}Ga_{0,875}N$, $In_{0,375}Ga_{0,625}N$, $In_{0,625}Ga_{0,375}N$ and $In_{0,875}Ga_{0,125}N$ 78

Figure.5.1 Process gases enter the horizontal flow reactor through the three-layered gas injection nozzle inlet... 86

Figure.5.2 schematic illustration of MOCVD process.. 87

Figure.5.3 Schematic flow of silicon (111) cleaning process................................ 88

Figure.5.4 shows the growth structure of the bulk $InGaN$ solar cell sample............... 91

Figure.5.5 shows the cross-section images of the sample for the ML (AlN/GaN)......... 92

Figure.5.6	shows the cross-section images of the sample for the ML (AlN/GaN) and the bulk $InGaN$ ………………………………………………………………..	92
Figure.5.7	shows the FESEM images of the cracks generated on the topmost GaN layer.	93
Figure.5.8	shows the schematic growth structure of the semi-bulk $InGaN/GaN$ solar cell sample…………………………………………………………………………	94
Figure.5.9	shows the cross-section images of the sample for the ML (AlN/GaN) and the semi-bulk $InGaN$ (MQW) with P-GaN growth………………………………	95
Figure.5.10	shows the FESEM images which shows crack free…………………………..	96

LISTS OF TABLES

Lists of Tables

Table.3.1 The lattice constant a, bulk modulus B and its first derivative B' of AlN, GaN, InN, $Al_{1-y}Ga_yN$ and $Al_xGa_yIn_{1-x-y}N$ compared to other experimental or theoretical data. VL indicated Vegard's law results in the table………………………………………….. 43

Table.3.2 The energy band gap E_g of AlN, GaN, InN, $Al_{1-y}Ga_yN$ and $Al_xGa_yIn_{1-x-y}N$ calculated with WC-GGA, TB-mBJ and Vegard's law compared to other experimental or theoretical data. 45

Table.3.3 Collected the peak positions of $\varepsilon_2(\omega)$, static dielectric constant $\varepsilon_1(0)$, refractive index $n(0)$ and Static reflectivity $R(0)$ for $Al_{0.343}Ga_{0.625}In_{0.031}N$, $Al_{0.468}Ga_{0.5}In_{0.031}N$ and $Al_{0.593}Ga_{0.25}In_{0.031}N$ compounds…………………………………… 55

Table.4.1 The lattice constant a and c, bulk modulus B and its first derivative B' of InN and GaN, compared to other experimental or theoretical data, the lattice mismatch $\Delta(a_o)$ and $\Delta(c_o)$ are indicated in the table…….. 66

Table.4.2 The lattice constant a and c calculated by The Vegard's law of $In_xGa_{1-x}N$, compared to other experimental work results…………… 67

Table.4.3 The energy band gap Eg of GaN, InN and $In_xGa_{1-x}N$ calculated with WC-GGA, LDA, TB-mBJ and Vegard's law compared to other experimental or theoretical data……………………………………… 68

Table.4.4 Collected the peak positions of $\varepsilon_2(\omega)$, static dielectric constant $\varepsilon_1(0)$, refractive index $n(0)$ and Static reflectivity $R(0)$ $In_{0,125}Ga_{0,875}N$, $In_{0,375}Ga_{0,625}N$, $In_{0,625}Ga_{0,375}N$ and $In_{0,875}Ga_{0,125}N$ …………... 74

Table.5.1 Growth parameter of each layer of the samples……………………… 89

GENERAL INTRODUCTION

INTRODUCTION

We are facing tremendous progress in materials development and design of advanced materials, driven by technical needs in all fields of modern production. A real revolution in materials science, however, could be observed during very recent years, a great leap from understanding bulk materials to the study, development, and application of nanostructured materials.

Materials today, aside from metals and alloys, include such different substances as ceramics, liquid crystals, polymers, foams, nano-tubes, nano-composites . . . and it is justified to ask: ‘‘What is the importance of alloys in the field of modern materials today? What role do alloys play in the fascinating advance toward nanostructurization?’’ [1].

Condensed matter physics and materials science are essentially related to the understanding and exploiting the properties of systems of interacting electrons and atomic nuclei. In principle, all the properties of materials can be addressed given suitable computational tools for solving this quantum mechanics issue. In fact, through the knowledge of the electronic properties it is possible to get information on structural, mechanical, electrical, vibrational, thermal and optical properties. However, the electrons and nuclei that compose materials constitute a strongly interacting many body systems and unfortunately this makes the direct solution of the Schrödinger's equation [2] an impractical proposition.

Semiconductor materials constitute today basic building blocks of emitters and receivers in cellular, satellite. Among them, the III- nitrides which are nowadays widely used by the industry. With respect to ‘classical’ III-V semiconductors, the group III- nitrides semiconductors have attracted much attention in recent years to their great potential for technological applications [3].

Nitrides are currently the most promising materials for blue, green, and UV optoelectronics. GaN as a representative of its binary cousins, InN and AlN, and their ternary along with the quaternary, is considered one of the most important semiconductors after Si. It is no wonder that it finds ample applications in lighting and displays of all kinds biosensors, medical imaging, optical data storage, lasers, detectors, and high-power amplifiers. These applications stem from the excellent optical and electrical properties of nitride semiconductors. One of the important methods of controlling properties of these materials relies on alloying instead of employing pure AlN, GaN, or InN [4-5].

In contrast, III-nitrides (III-Ns) have begun to gain considerable attention for use in photovoltaic (PV) devices [6]. InN is a suited semiconductor material because its low temperature dependence, high carrier mobility and low electron effective mass, that can be applied in photovoltaic devices, high frequency transmitters and high frequency detectors [7]. The band gap of InN was recently discovered to be 0.7 eV as opposed to the previously believed 1.3 eV. Since the band gap of $In_xGa_{1-x}N$ covering almost the entire spectral range, tunable from 0.7 eV for pure InN to 3.4 eV for pure GaN. Thus, enabling design of multi-junction solar cell structures with near ideal band gap for maximum efficiency [8].

The wurtzite structure is suitable for growing most III-nitride semiconductors [9]. Growth of $InGaN$ with sufficiently high In content (in particular to achieve green emission) has proved problematic however: The lattice mismatch between GaN and InN is =10% [10]. InN and In-rich $InGaN$ alloys have not been investigated thoroughly because of difficulties associated with the growth of these compound [11]. With increasing the thickness of $InGaN$ layer with high indium (In) content for absorbing light, the material quality becomes even worse [12].

PROBLEM STATEMENT

Recently, the $Al_xGa_yIn_{1-x-y}N$ quaternary alloy appeared as an attractive material for device applications [13]. The AlN and GaN lattice parameters are approaching each other, and significantly smaller than that of InN [14]. However, there is a problem of the lattice mismatch both between the epitaxial layers and between epitaxial layers and substrate, the challenge of the lattice mismatch can be solved by introduced a small amount of InN [15-16]. As a narrow gap semiconductor InN is expected to have a low electron effective mass m_e^* and thus a high mobility μ_e. This is very promising for the design of fast electronic and optoelectronic devices in the future [15].

Only recent sophisticated ab-initio band structure simulations have been able to provide a complete picture in agreement with the available experimental values for the energy gap and band parameters. The study is to investigate the structural, electronic and optical properties of the binary (AlN,GaN and InN), the ternary $Al_{1-y}Ga_yN$,the quaternary $Al_xGa_yIn_{1-x-y}N$ zinc-blende alloy and Wurtzite $In_xGa_{1-x}N$ using first-principles calculations. The plane-wave pseudopotential-based density functional theory (DFT) was implemented in the WIEN2K code [17] employed throughout the work.

Indium gallium nitride ($InGaN$) based alloys are widely used in the field of optoelectronics, such as light-emitting diodes (LEDs) and laser diodes (LDs). Recently, $InGaN$-based alloys have also interested much research attention in solar cell application [12]. In addition, the smaller direct bandgap of InN promotes the applications in solar energy conversion and optoelectronic [15].

Some results of the band structure of the III-nitrides AlN, GaN and InN of the two phases was calculated and reported by Rashid Ahmed et *al* [18] using GGA and obtained good results, for the ternary $AlGaN$, $InGaN$ and $AlInN$ some studies in wurtzite phase by Bo-Ting Liou et *al* [19] and the $AlGaN$ in the cubic phase by Z Dridi et *al* [20].

In addition, the $Al_xGa_yIn_{1-x-y}N$ quaternary studies in the wurtzite phase by M. Lopuszynski et *al* [21].

To date, the $InGaN/GaN$ multiple quantum well (MQW) solar cells with vertical structure using aluminum (Al) reflectors by Zhi-Wei Zheng et *al* [12], InGaN heterojunction solar cells using a semi-bulk absorber (multi-layered $InGaN/GaN$ structure) by M. Arif et *al* [22]. Textured surface has been performed on $InGaN$-based solar cells by J. Bai et *al* [23]. $In_xGa_{1-x}N/GaN$ double heterojunction solar cells by Carl J. Neufeld et *al* [8].

RESEARCH OBJECTIVES AND ORGANIZATION OF DISSERTATION

Accurate knowledge of the bandgap and optical properties of the III–V compounds is very important for the design and analysis of various optoelectronic and photonic devices. It is important to understand fundamental optical properties over a wide range of wavelengths. In reality, optical properties reflect density of states DOS of a compound and their analysis is one of the most effective tools to understand the electronic structure of a material [4].

The main objective of this theoretical study based on the full-potential linearized augmented plane wave method (FP-LAPW) based density functional theory (DFT) which was implemented in WIEN2K code [16-24] employed throughout the work, is to investigate the structural, electronic and optical properties of the compound GaN, AlN, InN, ternary $Al_{1-y}Ga_yN$, and quaternary $Al_xGa_yIn_{1-x-y}N$ zinc-blende alloys matched on AlN substrate and FP-LAPW calculations is applied and study of the structural and optoelectronic properties of the Wurtzite $In_xGa_{1-x}N$ matched on GaN substrate using 16-atom supercell.

The experiment part, is the application of the wurtzite structure III/V nitride ternary alloys $In_xGa_{1-x}N$, solar cells grown by metal-organic chemical vapor deposition (MOCVD) equipment. The $InGaN/GaN$ solar cells structures were on (111) silicon substrate.

The dissertation composed of five chapters and each of them is summarized as follows.

Chapter 1 gives brief introduction about the group III-nitrides semiconductors continuing great interest due to their vast technical application, which demands for a more cost efficient electronic and optoelectronic devices.

Chapter 2 is devoted to deal with the current advances in the theoretical modeling of DFT. The basic principles of this method are more detailed. The exchange correlation part of this functional is discussed, including both the local density approximation and generalized gradient approximation.

Chapter 3 describes the structural, electrical, and optical properties of GaN and its binary cousins as well as their related quaternary alloys in zinc-blende structure.

Chapter 4 illustrate the structural and optoelectronic properties of $In_xGa_{1-x}N$ ternary alloys in wurtzite structure.

Chapter 5 will describe the details and the process parameters of the experimental work which involved the process of cleaning the substrates, epitaxial growth and the characterizations method used to obtain the result for this thesis.

Finally, a general conclusion of this research is presented.

References

[1] W. Pfeiler, "Introduction," in *Alloy Physics: A Comprehensive Reference*, WILEY-VCH Verlag GmbH & Co. KGaA, Weinheim, 2007, pp. 1–18.

[2] E. Schrödinger, "An undulatory theory of the mechanics of atoms and molecules," *Phys. Rev.*, vol. 28, no. 6, pp. 1049–1070, 1926.

[3] M. B. Kanoun, *First-Principles study of Structural , Elastic and Electronic Properties of AlN and GaN Semiconductors under Pressure Effect and Magnetism in AlN : Mn and GaN : Mn systems*. 2004.

[4] B. Amin, I. Ahmad, M. Maqbool, S. Goumri-Said, and R. Ahmad, "Ab initio study of the bandgap engineering of $Al_{1-x}Ga_xN$ for optoelectronic applications," *J. Appl. Phys.*, vol. 109, no. 2, p. 023109, 2011.

[5] S. N. Lee, T. Jang, J. K. Son, H. S. Paek, T. Sakong, E. Yoon, O. H. Nam, and Y. Park, "Carrier transport by formation of two-dimensional hole gas in p-type Al0.1Ga0.9N/GaN superlattice for AlGaInN-based laser diode," *J. Cryst. Growth*, vol. 287, no. 2, pp. 554–557, 2006.

[6] Y. J. Dong, B. Z. Tian, T. J. Kempa, and C. M. Lieber, "Coaxial Group III- Nitride Nanowire Photovoltaics," *Nano Lett.*, vol. 9, pp. 2183–2187, 2009.

[7] M. Aslan, A. H. Reshak, B. G. Yalcin, S. Bagci, and M. Ustundag, "Structural and electronic properties of InN_xP_{1-x} alloy in full range ($0 \leq x \leq 1$)," *Philos. Mag.*, vol. 6435, no. March, pp. 1–15, 2016.

[8] C. J. Neufeld, N. G. Toledo, S. C. Cruz, M. Iza, S. P. DenBaars, and U. K. Mishra, "High quantum efficiency InGaN/GaN solar cells with 2.95 eV band gap," *Appl. Phys. Lett.*, vol. 93, no. 14, pp. 14–17, 2008.

[9] A. Laref, A. Altujar, and S. J. Luo, "The electronic and optical properties of InGaN-based solar cells alloys: First-principles investigations via mBJLDA approach," *Eur. Phys. J. B*, vol. 86, no. 11, pp. 1–11, 2013.

[10] A. I. Duff, L. Lymperakis, and J. Neugebauer, "Ab initio-based bulk and surface thermodynamics of InGaN alloys: Investigating the effects of strain and surface polarity," *Phys. Status Solidi Basic Res.*, vol. 252, no. 5, pp. 855–865, 2015.

[11] V. Y. Davydov, A. A. Klochikhin, V. V Emtsev, S. V Ivanov, V. V Vekshin, F. Bechstedt, J. Furthmuller, and H. Harima, "Band gap of InN and In-rich InGaN alloys," *Phys. Status Solidi B*, vol. 230, no. 2003, p. R4, 2002.

[12] Z.-W. Zheng, M.-H. Lai, L.-Y. Ying, and B.-P. Zhang, "High-efficiency vertical-type InGaN/GaN multiple quantum well solar cells using aluminum reflectors," *2016 IEEE 16th Int. Conf. Nanotechnol.*, pp. 91–93, 2016.

[13] M. Marques, L. K. Teles, L. M. R. Scolfaro, J. R. Leite, J. Furthmüller, and F. Bechstedt, "Lattice parameter and energy band gap of cubic AlxGayIn1-x-yN quaternary alloys," *Appl. Phys. Lett.*, vol. 83, no. 5, pp. 890–892, 2003.

[14] I. Vurgaftman and J. R. Meyer, "Band parameters for nitrogen-containing semiconductors," *J. Appl. Phys.*, vol. 94, no. 6, pp. 3675–3696, 2003.

[15] V. A. Elyukhin, "On spinodal decomposition of $B_xAl_yGa_{1-x-y}N$, $B_xGa_yIn_{1-x-y}N$ and $B_xAl_yIn_{1-x-y}N$ alloys," *Phys. Status Solidi*, vol. 2, no. 10, pp. 3556–3559, 2005.

[16] M. Millot, N. Ubrig, J. M. Poumirol, I. Gherasoiu, W. Walukiewicz, S. George, O. Portugall, J. Léotin, M. Goiran, and J. M. Broto, "Determination of effective mass in InN by high-field oscillatory magnetoabsorption spectroscopy," *Phys. Rev. B - Condens. Matter Mater. Phys.*, vol. 83, no. 12, pp. 1–5, 2011.

[17] K. Schwarz and P. Blaha, "Solid state calculations using WIEN2k," *Comput. Mater. Sci.*, vol. 28, no. 2, pp. 259–273, 2003.

[18] R. Ahmed and H. Akbarzadeh, "A first principle study of band structure of III-nitride compounds," vol. 370, pp. 52–60, 2005.

[19] B.-T. Liou, S.-H. Yen, and Y.-K. Kuo, "Vegard's law deviation in band gaps and bowing parameters of the wurtzite III-nitride ternary alloys," *Semicond. Lasers Appl. II*, vol. 5628, pp. 296–305, 2005.

[20] Z. Dridi, B. Bouhafs, and P. Ruterana, "First-principles study of cubic AlxGa1-xN alloys," *Comput. Mater. Sci.*, vol. 33, no. 1–3, pp. 136–140, 2005.

[21] M. Łopuszyński and J. A. Majewski, "Composition dependence of elastic constants in wurtzite AlGaInN alloys," *J. Appl. Phys.*, vol. 111, no. 3, pp. 1–5, 2012.

[22] M. Arif, W. Elhuni, J. Streque, S. Sundaram, S. Belahsene, Y. El Gmili, M. Jordan, X. Li, G. Patriarche, A. Slaoui, A. Migan, R. Abderrahim, Z. Djebbour, P. L. Voss, J. P. Salvestrini, and A. Ougazzaden, "Improving InGaN heterojunction solar cells efficiency using a semibulk absorber," *Sol. Energy Mater. Sol. Cells*, vol. 159, no. September 2016, pp. 405–411, 2017.

[23] J. Bai, M. Athanasiou, and T. Wang, "Solar Energy Materials & Solar Cells Influence of the ITO current spreading layer on ef fi ciencies of InGaN-based solar cells," *Sol. Energy Mater. Sol. Cells*, vol. 145, pp. 226–230, 2016.

[24] S. Valedbagi, A. Fathalian, and S. Mohammad Elahi, "Electronic and optical properties of AlN nanosheet: An ab initio study," *Opt. Commun.*, vol. 309, pp. 153–157, 2013.

CHAPTER 1
GENERAL PROPERTIES OF NITRIDES

1.1 INTRODUCTION

Research advances in III-nitride semiconductor materials and their alloys have recently emerged as a strategic materials system to an exponential increase inactivity directed towards electronic and optoelectronic applications. There is also great scientific interest in this class of materials because they appear to form the first semiconductor system in which extended defects do not severely affect the optical properties of devices [1-2].

We attempt in this chapter to draw the motivation and aims of our study. This chapter begins with the Definition of Group III-Nitride semiconductors. In the next section, we will present the Alloys definition and classification. The last section is devoted to the presentation of the different technological applications of III-Nitrides for optoelectronics.

1.2 DEFINITION OF GROUP III-NITRIDE SEMICONDUCTORS

The conjecture that the III-V compounds should be semiconductors is amply confirmed. Following the group III and Group V columns of the periodic table from the top down, one obtains the following compounds semiconductors: BN, BP, BAs, AlN, AlP, $AlAs$, $AlSb$, GaN, GaP, $GaAs$, $GaSb$, InN, InP, $InAs$ and $InSb$. Except for the nitrides all these compounds crystallize into the zinc-blende structure. The nitrides are stable in the wurtzite structure; BN and GaN also have metastable zinc-blende phases. Just, as in the case of the elemental semiconductors of group IV, the mixed crystals made of binary III-V compounds also have semiconducting properties. Examples are $(Ga, Al)As$, $Ga(As, P)$, $(In, Ga)As$ and $(In, Ga)(As, P)$. The principal applications of the III-V semiconductors and their alloys lie in the field of optoelectronics. $(Ga, Al)As$ and $Ga(As, P)$ are used, for example, in light emitting diodes (LEDs) and laser diodes for the near infrared to green spectral region. GaN, is a promising material for blue LEDs and laser diodes. The quaternary alloy system (Ga, In), (As, P) is used in making lasers and photodiodes for optical fiber communications at 1.55μm wavelengths, which provides maximum transmission for $SiO2$-based fibers. $GaAs$ and, also $(Ga, Al)As$ are employed for transistors with extremely short time delay. BN and GaN can be used for electronic devices to be operated at high temperatures [3].

1.3 CRYSTAL STRUCTURE OF NITRIDES

Gallium nitride and its related compounds can crystallize both in the zinc-blende as well as in the wurtzite structure and rocksalt structures. At ambient conditions, the thermodynamically stable structure is wurtzite for bulk AlN, GaN, and InN [4-5]. The zinc-

blende (ZB) structure for GaN and InN has been stabilized by epitaxial growth of thin films on {011} crystal planes of cubic substrates such as Si, MgO, and $GaAs$. In these cases, the intrinsic tendency to form the wurtzite (Wz) structure is overcome by topological compatibility [4-6]. The electronic properties of wurtzite and zinc-blende modifications of GaN, InN, and AlN are related, but show significant differences, which add an additional dimension to this field of research. Crystallographically, the zinc-blende structure and wurtzite structure are very closely related [5].

The rocksalt, or $NaCl$, structure can be induced in AlN, GaN, and InN at very high pressures.

1.3.1 THE ZINC-BLENDE STRUCTURE

The zinc-blende structure has a cubic unit cell, containing four group III elements and four nitrogen elements. The space group for the zinc-blende (ZB) structure is $F43\,mc\ (T_d^2)$ The position of the atoms within the unit cell is identical to the diamond crystal structure, has the same sublattices, except that the anions (the non-metal elements) occupy one sublattice, while the cations (the metal atoms) sit on the other. Both structures consist of two interpenetrating face-centered cubic sublattices, have an fcc lattice with two atoms per unit cell. Figure.1.1(a) shows the arrangement of the atoms inside a cube of the zinc-blende structure.

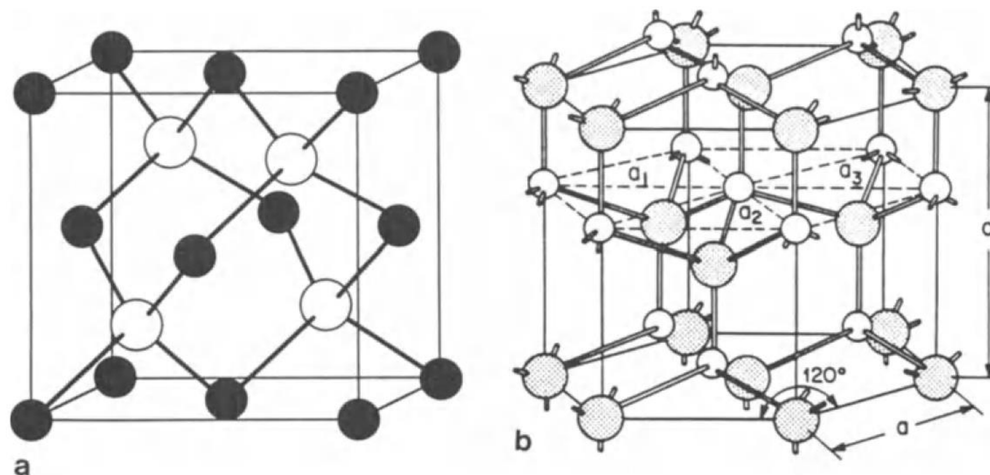

Figure.1.1 Atomic positions in zinc- blende(a) and wurtzite crystal(b) [7]

Each atom in the structure may be viewed as positioned at the center of a tetrahedron, with its four nearest neighbors defining the four corners of the tetrahedron [7-8].

1.3.2 THE WURTZITE STRUCTURE

The wurtzite polytype has a hexagonal unit cell Figure.1.1.(b) and thus two lattice constants, c and a. It should be noted that while the ideal hcp has a hexagon eight c to edge length a (c/a) ratio of $(8/3)^{1/2} = 1.633$, most wurtzite semiconductors have slightly different c/a ratios. Unlike the zinc-blende structure, which only requires a single parameter (the lattice constant a) to specify the crystal, the wurtzite structure requires three: the lattice constant a, the c/a ratio, and the ratio γ of the bond length along the c direction to the other three (equal) bond lengths. The space group for the wurtzite structure is $P6_3mc(C_{6v}^4)$ [7-8].

Wurtzite is similar to the zinc-blende structure; both are fourfold coordinated, except that the former has a hexagonal close-packed (hcp) Bravais lattice rather than an fcc. The difference between wurtzite and zinc-blende can be described most easily by examining the stacking sequence of planes of close-packed spheres of the same radius along the (111) direction. The fcc lattice repeats a characteristic tacking sequence every three layers, while the hcp repeats the stacking sequence every two layers. After the one sublattice is specified, say the anion, sublattice, between every two anion planes a plane of cations can be inserted such that each cation is surrounded by four anions in a tetrahedral arrangement, and vice versa. Thus, as far as the local tetrahedral bonding is concerned, there is no difference between zinc-blende and wurtzite structures. The difference comes when the second and farther neighboring atoms are considered. The other difference is that there are four atoms per unit cell in a wurtzite semiconductor, because each hcp unit cell contains two non-equivalent atomic sites [7].

In both cases, each group-III atom is coordinated by four nitrogen atoms. Conversely, each nitrogen atom is coordinated by four group-III atoms. The main difference between these two structures lies in the stacking sequence of closest packed diatomic planes [4]. For the wurtzite structure, the stacking sequence of (0001) planes is ABABAB in the <0001> direction. For the zinc-blende structure, the stacking sequence of (111) planes is ABCABC in the <111> direction.

1.4 BRILLOUIN ZONE

A convenient method of defining the various planes in a crystal is to use Miller indices, which are determined by first finding the intercepts of the plane with the three basis axes in terms of the lattice constants, and then taking the reciprocals of these numbers and reducing them to the smallest three integers having the same ratio. The result is enclosed in parentheses

(hkl) as the Miller indices for a single plane or a set of parallel planes. Figure.1.2 shows the Miller indices of important planes in a cubic crystal [9].

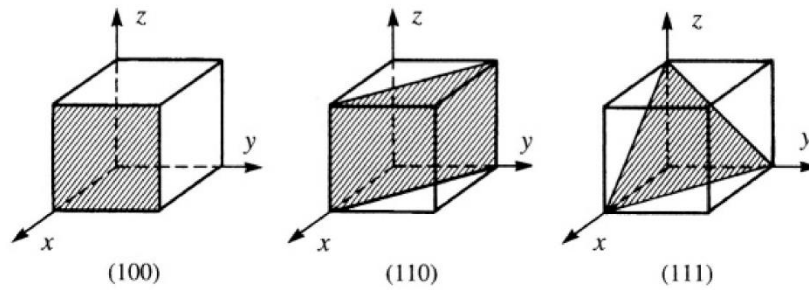

Figure.1.2 Miller indices of some important planes in a cubic crystal [9-10].

Some other conventions are given as follows:

$(\bar{h}kl)$: for a plane that intercepts the x axis on the negative side of the origin. When an intercept along any axis is negative, a bar is placed over that index.

$\{hkl\}$: The set of symmetrically (structurally) equivalent planes such as $\{100\}$ for (100), (010), (001), $(\bar{1}00)$, $(0\bar{1}0)$, and $(00\bar{1})$ in cubic symmetry.

$\langle hkl \rangle$: for a full set of equivalent directions.

$[a_1 a_2 a_3\ c]$: . In the hexagonal structure, the planes are referred to three coplanar a-axes, at 120° to each other, and a fourth c-axis normal to them; the indices in this case are $(hkil)$,

Where $i = -\ (h\ +\ k)$ and the index l is related to the intercept on the c-axis. Here it is customary to use four axes

For the two semiconductor elements, germanium and silicon, the easiest breakage, or cleavage, planes are the $\{111\}$ planes. In contrast, gallium arsenide, which has a similar lattice structure but also has a slight ionic component in the bonds, cleaves on $\{110\}$ planes.

The unit cell for a reciprocal lattice can be represented by a Wigner-Seitz cell. The Wigner-Seitz cell is constructed by drawing perpendicular bisector planes in the reciprocal lattice from the chosen center to the nearest equivalent reciprocal lattice sites. Figure.1.3 (a) shows a typical example for a face centered cubic structure. If one first draws lines from the center point (Γ) to the eight corners of the cube, then forms the bisector planes, the result is the truncated octahedron within the cube-a Wigner-Seitz cell. It can be shown that a face centered cubic (fcc)

direct lattice with lattice constant a has a body-centered cubic (bcc) reciprocal lattice with spacing $4\pi/a$. Thus, the Wigner-Seitz cell shown in Figure.1.3 (a) is the unit cell of the reciprocal lattice of an fcc direct lattice. The Wigner-Seitz cell for a wurtzite structure can be similarly constructed, Figure.1.3 (b) shows the result for the wurtzite structure [3-9-10].

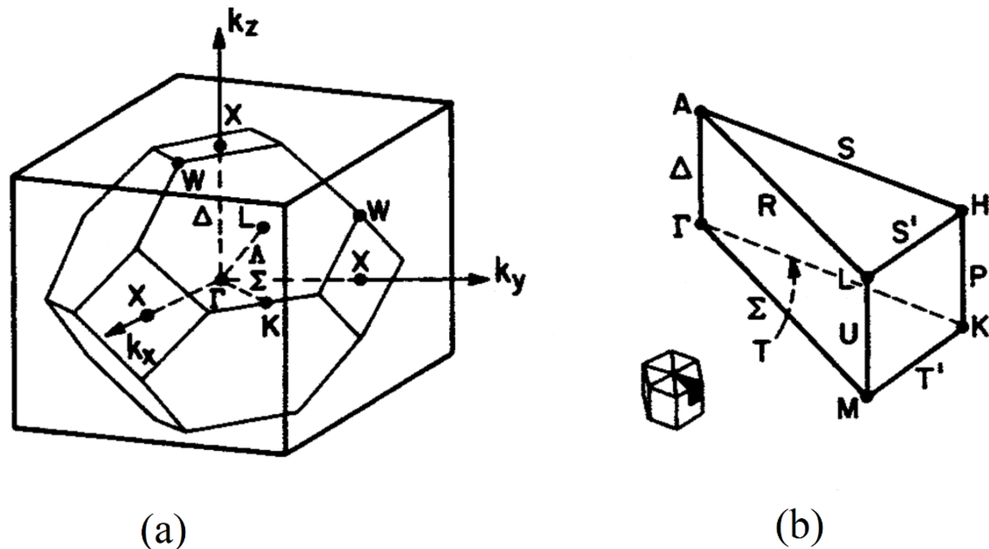

Figure.1.3 (a) Brillouin zone for diamond and zinc-blende lattices, (b) Brillouin zone for wurtzite [10].

The most important symmetry points and symmetry lines, are also indicated: Γ: $2\pi/a(0,0,0)$, zone center; L: $2\pi/a(1/2, 1/2, 1/2)$, zone edge along $\langle 111 \rangle$ axes (Λ); X: $2\pi/a(0,0,1)$, zone edge along $\langle 100 \rangle$ axes Δ; K: $2\pi/a(3/4, 3/4, 0)$, zone edge along $\langle 110 \rangle$ axes ($\sum$) [9].

1.5 ENERGY-BAND STRUCTURE

The information on the electronic band structure can be illustrated by employing the first Brillouin zone, or as often referred to as Brillouin zone, which is expressed for one period of the reciprocal lattice centered about the origin of the k-space (see Figure.1.3). In this case, the edges of the bands are described using the boundaries of a three-dimensional figure in k-space. In other words, this representation provides a three-dimensional description of the band theory by using Brillouin zones [10].

The band structure of a crystalline solid, that is, the energy-momentum $(E - K)$ relationship, is usually obtained by solving the Schrödinger equation of an approximate one-electron problem. The Bloch theorem, one of the most important theorems basic to band

structure, states that if a potential energy $V(r)$ is periodic with the periodicity of the lattice, then the solutions $\phi_K(r)$ of the Schrödinger equation (1.1) [9]

$$\left[-\frac{\hbar}{2m}\nabla^2 + V(r)\right]\phi_K(r) = E_k\phi_K(r) \quad (1.1),$$

are of the form $\phi_K(r) = e^{jk.r}U_n(k,r)$ Bloch function. (1.2).

Energy regions or energy bands are permitted above and below this energy gap. The upper bands are called the conduction bands, the lower bands are the valence bands. There is a forbidden energy region, which is referred to as the energy gap, which separates the conduction band from the valence band. More specifically, the energy gap is defined as the energy separation between the highest valence band maximum and the lowest conduction band minimum, which is the most important parameter in semiconductor physics, we consider the simplified-band picture shown in Figure.1.4.

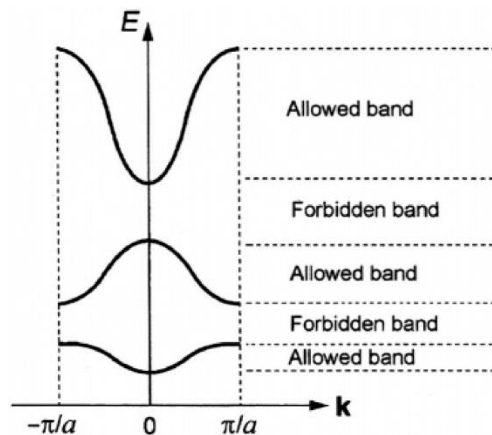

Figure.1.4 The reduced-zone representation [10].

In this figure the bottom of the conduction band is designated Ec, and the top of the valence band Ev [9-10].

1.6 THE ALLOYS

1.6.1 ALLOY DEFINITION

An alloy is a 'mixture' or a combination, either in solution or compound of two or more chemical elements that are chemically combined in fixed proportions, one of which at least is a metal. The alloying element can be distributed over the crystal lattice sites of the host element and yield a solid solution, or it can form different phases showing up as particles in a ''matrix.'' Whereas the physical properties of a solid solution are essentially determined by the chemical

composition of the constituents (the ratio of each element is usually expressed by chemical formula), the properties of a multiphase alloy are determined largely by the spatial distribution of the second-phase particles. This possibility of ''designing'' physical and technical properties of a material by a careful selection of alloying elements and alloying concentrations put alloys in the forefront of materials from early human history up to our time at the beginning of the third millennium [8-11].

Simply, an alloy is formed from a physical mixture of two or more substances, while a compound is formed from a chemical reaction. An alloy crystal is sometimes called a mixed crystal or a solid solution. For example, $GaAs$ is a compound consisting of Ga atoms bonded to As atoms.

1.6.2 Alloys classification

An alloy with two components is called a binary alloy; one with three is a ternary alloy and one with four is a quaternary alloy.

1.6.2.1 Binary alloys

Reaction of a compound A with another B leads in general to the formation of ordered stoichiometric compounds A_nB_m, disordered solid solutions A_xB_{1-x} of composition x, and /or phase separation [12]. Binary compounds consisting of atoms belonging to Groups III and V of the periodic table ($A^{III}B^{V}$ semiconductors) such as crystallize with the zinc-blende structure such as BN, AlN, GaN, and InN. The elemental cell of the zinc-blende structure is shown in Figure.1.5 [13].

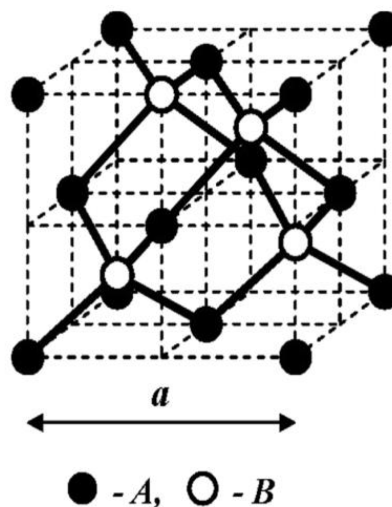

Figure.1.5 AB semiconductor compounds with the zinc-blende structure.

This crystal is composed of these two elements A and B that occupy at random the regular lattice sites of the structure, in propositions x and $(1-x)$ for the compositions A_xB_{1-x} is the binary alloy [14].

1.6.2.2 TERNARY ALLOYS

Two types of atoms in ternary alloys of two binary compounds may be Group II, Group III, or Group IV atoms, and the third type of atoms should be Group V or Group VI atoms in $A_x^{II}\ B_{1-x}^{II}C^{VI}$, $A_x^{III}\ B_{1-x}^{III}C^{V}$, and $A_x^{IV}\ B_{1-x}^{IV}C^{VI}$ alloys, and, vice versa, in $A^{II}\ B_x^{VI}C_{1-x}^{VI}$, $A^{III}\ B_x^{V}C_{1-X}^{V}$, and $A^{IV}B_x^{VI}C_{1-x}^{VI}$ alloys.

There are two types of the concentrations that can be used for ternary semiconductor alloys of binary compounds. The concentrations of the first type are the concentrations of chemical bonds between the nearest neighbors or concentrations of compounds or the chemical composition of an alloy. Therefore, a ternary alloy of two binary compounds is written as $A_xB_{1-x}C$ or AB_xC_{1-x}. The unit cells of $A_xB_{1-x}C$ or AB_xC_{1-x} atomically disordered alloys with the zinc-blende structure are shown in Figure.1.6 (a) and (b), where x is the concentration of atoms A in the cation-mixed sublattice of $A_xB_{1-x}C$ alloys and the concentration of B atoms in the anion-mixed sublattice of AB_xC_{1-x} alloys, respectively.

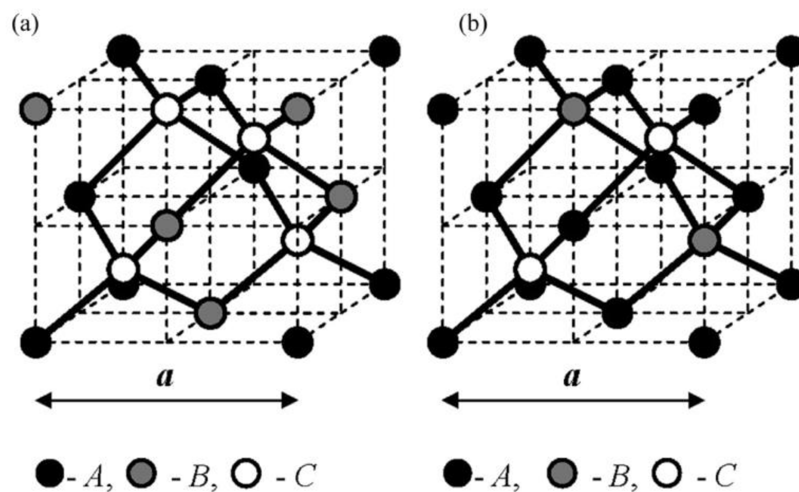

Figure.1.6 (a) $A_xB_{1-x}C$ and (b) AB_xC_{1-x} Alloys with the zinc-blende structure.

The ternary is a Pseudo-binary semiconductor alloys such as $A_x^{\mathrm{III}}B_{1-x}^{\mathrm{III}}C^{\mathrm{V}}$ [15], obeys quadratic dependence on the molar fraction x, lattice parameters that are close to the composition (x) weighted average

$$a(x) \cong xa_{AC} + (1-x)a_{BC} \quad (1.3),$$

of the AC and BCcompounds (Vegard's rule) [16] and band gaps that are smaller than the composition weighted average (positive “optical bowing”)

$$E_g(x) = xE_{g.AC} + (1-x)E_{gBC} - bx(1-x) \quad (1.4),$$

where E_{gAC} and E_{gBC} are the direct-energy gap of constituent AC and BC compounds respectively, and b is the bowing parameter [17].

2.6.2.3 QUATERNARY ALLOYS

There has been some interest for the arrangement of III-V quaternary alloy systems that are shaped by selecting either three group Ill elements and one group V element, or one group III element and three group V elements. In quaternary alloys of three binary compounds, three types of atoms are placed in the mixed sublattice and atoms of the fourth type form another sublattice. These alloys are written as $A_xB_yC_{1-x-y}D$ or $AB_xC_yD_{1-x-y}$, where x is the concentration of atoms A or atoms B in the mixed sublattice, correspondingly, y is the concentration of atoms B or atoms C in the same sublattice, respectively [13]. $A_xB_yC_{1-x-y}D$ alloy with the zinc-blende structure is shown in Figure.1.7.

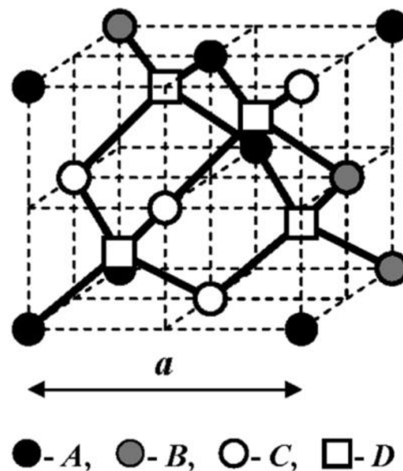

Figure.1.7 $A_xB_yC_{1-x-y}D$ alloys with the zinc-blende structure.

These are here-after referred to as $3:1$ or $1:3$ quaternary alloys. The following convention is adopted: the composition variables associated with the three variable elements are in the order x, y, and z. These are compelling by: $x + y + z = 1$.

A $1:3$ quaternary alloy will be described as $AB_xC_yD_z$, where A is a group III element and B, C and D are group V elements listed according to increasing atomic number. A $3:1$

quaternary alloy will be described as $A_xB_yC_zD$, where A, B and C are group III elements listed in increasing atomic number and D is a group V element.

In this work, we implemented the $3:1$ quaternary alloy described as $A_xB_yC_{1-x-y}D$ is thought to be constructed from three binaries: AD, BD and CD. The corresponding linear interpolation is given by [18]:

$$a(x) \cong xa_{AD} + (1-x)a_{BD} + (1-x-y)a_{CD} \quad (1.5).$$

The band gap location of the ternary and quaternary alloys can be linearly interpolated form the binary data as below [19]:

For the $A_{1-x}B_xC_{1-x}D_y$,

$$E_{ABCD} = (1-x)(1-y)E_{AC} + x(1-y)E_{BC} + (1-x)yE_{AD} \quad (1.6),$$

and for the $AB_xC_yD_{1-x-y}$,

$$E_{ABCD} = xE_{AB} + yE_{AC} + (1-x-y)E_{AD} \quad (1.7),$$

where, E_{AB} is the energy of the top of the valence band of AB binary alloy.

1.7 APPLICATIONS OF III-NITRIDES FOR OPTOELECTRONICS

Some III–V compounds, such as GaN and AlN, are the wide energy-gap semiconductors that are useful materials in optoelectronic devices operating in the visible and ultraviolet spectral regions, as well as in high–temperature and high-power devices [10].

III-Nitride semiconductors have been widely employed for energy-efficiency technologies; one of the main forces behind the excellent enthusiasm for Ill-Nitride materials has been their potential for optoelectronic devices applications including light-emitting diodes (LEDs) for solid-state lighting, photovoltaics, and thermoelectric applications. Two sorts of devices are the concentration of the exploration work in this area: ultraviolet (UV) photo-detectors and violet-blue-green light emitters [20-21].

1.7.1 ULTRAVIOLET PHOTODETECTORS

A photodetector is a semiconductor device that can detect optical signals [22]. The sun produces a great quantity of UV, which a great part is absorbed by the ozone and gas layer of the atmosphere. Alone radiation whose wavelength is large than 280 nm get on earth. Detectors of UV radiation produced on earth [23], these ultraviolet sensitive detectors do not respond to

the visible solar spectrum, and are known as solar-blind [24], have to detect radiations between 265nm and 280nm, zone presenting the less parasitic radiation. Recently, there has currently been considerable interest in ultraviolet (UV) photodetectors owing to their versatile applications, such as missile warning and tracking, engine/flame monitoring, chemical/biological agent detection, and space-to-space communication [22].

The nitrides of elements of column III present a strong interest for optical detection, the III-Nitride based UV photodetectors remain a very promising field for research and development for the future [21], $AlInGaN$ has also attracted much attention as a material for optoelectronic devices operating in UV region [25].

Compared with ternary $AlGaN$, the quaternary $AlInGaN$ provides an extra degree of freedom by allowing independent control of the band gap and lattice constant [26] can vary between 1,9eV (650nm) and 6,2eV (200nm).

The progression to a higher wavelength flexibility, faster response, higher rejection of visible light, lower noise interference, and better response are all indicative of not only improved designs, but also a continued increase in the quality of material [21].

1.7.2 VISIBLE LIGHT EMITTING DIODES

LED is a semiconductor p–n junction diode, which employs radiative recombination of injected minority carriers with the majority carriers and subsequent emission of light from the polarized junction. This effect is also referred as an injection electroluminescence, i.e., the conversion of electrical energy into light [10], the frequency (color) of the photon is governed by the band gap of the semiconductor as given by the Planck relation, $hv = E_g$, which, in appropriate units, can be expressed as [27]:

$$E_g(eV) = 1.24/\lambda(\mu m) \quad (1.8).$$

The III-nitride semiconductor has received much attention in the past, since they have important applications in light emitting diodes (LEDs) [28], they have been successfully used in commercial bright blue and green light emitting diodes (LEDs). Nitride-based blue and green light emitting diodes (LEDs) have already been extensively used in traffic light lamps and full color displays [25].

GaN and related materials such as $AlGaInN$ are III-V nitride semiconductors with the wurtzite crystal structure and a direct energy band gap which is suitable for light emitting

devices. The band gap energy of $AlGaInN$ varies between 6.2 eV and 1.95 eV depending on its composition at room temperature. Therefore, III-V nitride semiconductors are particularly useful for light emitting devices in the short wavelength regions [5].

To date, Mathew C et al [29] violet LED (405 nm), M. Binder et al [30] and Yen-Kuang Kuo et al [31] blue LED (425/450 nm), Shuichiro Yamamoto et al [32] green (520 nm), the $InGaN$ quantum-well green light-emitting diodes with large-bandgap $AlGaInN$ thin barriers, chosen as lattice-matched $AlGaInN$ alloys by Guangyu Liu et al [20], the yellow and even amber LEDs using III-Nitride materials have been demonstrated. Even white LEDs by P. Waltereit et al [33] have recently been demonstrated by combining a bright blue LEDs based on III-nitride semiconductors have already paved the way for full-color displays and for mixing three primary colors to obtain white light for illumination [28].

1.7.3 Laser diodes

The first current-injection III-V nitride based LDs were fabricated by Nakamura et al. using an $InGaN$ multi-quantum-well (MQW) structure as the active layer, the LDs have found applications in optical storage, projection displays, and other areas. Future applications may include visible light communication and laser-based white lighting. For lighting applications, LDs have advantages over LEDs, including higher power per chip area and the absence of efficiency droop above threshold [5-34].

As compared to the LEDs, the semiconductor diode lasers typically provide light output with narrower wavelength range, higher powers, and more directionality [10].

The $InGaN$ and $AlGaN$ ternary nitride semiconductors have been studied extensively, because the $InGaN$ is the main material of blue-violet light LDs such as $InGaN$ emitting at blue ($\lambda = 450\ nm$) [35] and $InGaN/GaN$ multiple quantum well (MQW) emitting at 439 nm [34].

(UV) semiconductor laser diodes are of great interest for a wide range of applications including medical diagnostics, gas sensing, biochemical agent detection and materials processing [36]. The $AlGaN$ is the material of ultraviolet (UV), and the $AlGaN$ is often taken as barrier layer, cladding layer, and distributed Bragg reflector (DBR) in semiconductor lasers having quantum wells [28], $AlGaN$ Laser heterostructures emitting in the UV-C spectral range between 272 and 279 nm [36], $AlGaN$ MQW LD emitting in 380 nm [37].

1.7.4 SOLAR CELLS

Solar cells at present furnish the most important long duration power supply for satellites and space vehicules. Solar cells have also been successfully employed in small scale terrestrial applications. The sollar cell is considered a major condidate for obtaining energy from the sun. the sollar cell is considered a major candidate for obtaining energy, this energy supply for a solar cell is photons coming from the sun, since it can convert sunlight directly to electricity with high conversion efficiency, can provide nearly permanent power at low operating cost and it virtully free of pollution [9].

The low band gap values of two phases of InN have become a test to identify the general chemical trends of semiconductor band gaps. Small band gap value of InN is particularly useful as it will provide an extra dimension in the application of this compound. As a small band gap material, InN and its III-nitride alloys could be suitable for low future-generation solar cells.

To date, the $InGaN/GaN$ multiple quantum well (MQW) solar cells with vertical structure using aluminum (Al) reflectors by Zhi-Wei Zheng et *al* [38], $InGaN$ heterojunction solar cells using a semibulk absorber (multi-layered $InGaN/GaN$ structure) by M. Arif et *al* [39]. Textured surface has been performed on $InGaN$-based solar cells by J. Bai et *al* [40]. $In_xGa_{1-x}N/GaN$ double heterojunction solar cells by Carl J. Neufeld et *al* [41].

1.8 CONCLUSION

In this chapter, the physical and electronic properties of the III-Nitrides materials, the several obvious differences between the nitrides and the better known III-V compound semiconductors have been presented as well as the theory of the alloys. The exceptional physical properties of these materials and their use in numerous optoelectronics applications such as ultraviolet photodetectors and violet-blue-green light emitting devices have been reviewed.

REFERENCES

[1] F. Bernardini and V. Fiorentini, "Nonlinear macroscopic polarization in III-V nitride alloys," *Phys. Rev. B*, vol. 64, pp. 85207-1–7, 2001.

[2] M.O.MANASREH, *III-V Nitride Semiconductors: Defects and structural Properties*, vol. 22. Elsevier Science B.V, 2000.

[3] R. Enderlein, *Fundamentals of Semiconductor Physics and devices*. World Scientific Publishing Co. Re. Ltd, 1997.

[4] H. Morkoc, *Handbook of Nitride Semiconductors and Devices*, vol. 1. WILEY-VCH Verlag GmbH & Co. KGaA, Weinheim, 2008.

[5] S. Nakamura, M. Senoh, S. Nagahama, N. Iwasa, T. Yamada, T. Matsushita, H. Kiyoku, and Y. Sugimoto, "InGaN-Based Multi-Quantum-Well-Structure Laser Diodes," *Jpn. J. Appl. Phys.*, vol. 35, no. Part 2, No. 1B, pp. L74–L76, 1996.

[6] S. Han, X. Feng, Z. H. Lu, D. Johnson, and R. Wood, "Erratum: 'Transparent-cathode for top-emission organic light-emitting diodes,'" *Appl. Phys. Lett.*, vol. 83, no. 13, pp. 2719–2719, 2003.

[7] A.-B. Chen and A. Sher, *Semiconductor Alloys Physics and Materials Engineering*. Plenum Press, 1995.

[8] S. Adachi, *Properties of Semiconductor Alloys : Group-IV , III – V and II – VI Semiconductors*. John Wiley & Sons, Ltd, 2009.

[9] S.M.Sze, *Physics of Semiconductor Devices*, Second edi. John Wiley & Sons, Ltd, 1981.

[10] B.G.Yacobi, *Semiconductor Materials An Introduction to Basic Principles*. Kluwer Academic Publishers, 2004.

[11] W. Pfeiler, "Introduction," in *Alloy Physics: A Comprehensive Reference*, WILEY-VCH Verlag GmbH & Co. KGaA, Weinheim, 2007, pp. 1–18.

[12] A. A. Mbaye, L. G. Ferreira, and A. Zunger, "First-principles calculation of semiconductor-alloy phase diagrams," *Phys. Rev. Lett.*, vol. 58, no. 1, pp. 49–52, 1987.

[13] Vy. A.ElYUKHIN, *Statistical Thermodynamics of Semiconductor Alloys*. Elsevier Inc, 2016.

[14] C. Kittel, *Introduction to Solid State Physics*, 8th ed. John Wiley & Sons, Inc, 2005.

[15] G.P.Srivastava, J. luis Martins, and A. Zunger, "Atomic structure and ordering in semiconductor alloys," *Phys. Rev. B*, vol. 31, no. 4, pp. 2561–2564, 1985.

[16] L. Vegard, "Die Konstitution der Mischkristalle und die Raumfullung der Atome," *Zeitschrift fur Phys.*, vol. 5, no. 1, pp. 17–26, 1921.

[17] Y. Koide, H. Itoh, M. R. H. Khan, K. Hiramatu, N. Sawaki, and I. Akasaki, "Energy band-gap bowing parameter in an Al_xGa_{1-x} N alloy," *J. Appl. Phys.*, vol. 61, no. 9, pp. 4540–4543, 1987.

[18] C. K. Williams, T. H. Glisson, J. R. Hauser, and M. A. Littlejohn, "ENERGY BANDGAP AND LATTICE CONSTANT CONTOURS OF lll-V QUATERNARY ALLOYS OF THE FORM $A_xB_yC_zD$ or $AB_xC_yD_z$," *J. Electron. Mater.*, vol. 7, no. 5, pp. 639–646, 1978.

[19] S. Sakai, Y. Ueta, and Y. Terauchi, "Band gap energy and band lineup of III-V alloy semiconductors incorporating Nitrogen and Boron," *Jpn. J. Appl. Phys.*, vol. 32, no. 10, pp. 4413–4417, 1993.

[20] G. Liu, J. Zhang, C. K. Tan, and N. Tansu, "Efficiency-droop suppression by using large-bandgap AlGaInN thin barrier layers in InGaN quantum-well light-emitting diodes," *IEEE Photonics J.*, vol. 5, no. 2, 2013.

[21] Yoon-Soo Park, "Wide bandgap III-Nitride semiconductors: opportunities for future optoelectronics," 2001, vol. 4413, no. 5, pp. 282–292.

[22] J. Zhang, Y. Naoi, S. Sakai, A. Fukano, and S. Tanaka, "Fabrication and photovoltaic measurements of surface nanostructure of AlGaInN-based photodetector," *Jpn. J. Appl. Phys.*, vol. 48, no. 11, 2009.

[23] M. B. Kanoun, *First-Principles study of Structural , Elastic and Electronic Properties of AlN and GaN Semiconductors under Pressure Effect and Magnetism in AlN : Mn and GaN : Mn systems*. 2004.

[24] V. Kuryatkov, A. Chandolu, B. Borisov, G. Kipshidze, K. Zhu, S. Nikishin, H. Temkin, and M. Holtz, "Solar-blind ultraviolet photodetectors based on superlattices of AlN/AlGa(In)N," *Appl. Phys. Lett.*, vol. 82, no. 9, pp. 1323–1325, 2003.

[25] Y. D. Jhou, S. J. Chang, Y. K. Su, C. H. Chen, H. C. Lee, Y. Y. Lee, and C. H. Liu, “Quaternary AlInGaN-based photodetectors,” *Optoelectron. IET*, vol. 2, no. 1, pp. 42–45, 2008.

[26] W. Lai, S. Chang, M. Yokoyam, J. Sheu, and J. F. Chen, “InGaN – AlInGaN Multiquantum-Well LEDs,” *IEEE Photonics Technol. Lett.*, vol. 13, no. 6, pp. 559–561, 2001.

[27] B. G. Streetman and S. K. Banerjee, *Solid State Electronic devices*, 6th editio. PHI Learning, 2009.

[28] B. T. Liou and C. W. Liu, “Electronic and structural properties of zincblende $Al_xIn_{1-x}N$,” *Opt. Commun.*, vol. 274, no. 2, pp. 361–365, 2007.

[29] M. C. Schmidt, K. C. Kim, H. Sato, N. Fellows, H. Masui, S. Nakamura, S. P. DenBaars, and J. S. Speck, “High power and high external efficiency m-plane InGaN light emitting diodes,” *Japanese J. Appl. Physics, Part 2 Lett.*, vol. 46, no. 7, pp. L126–L128, 2007.

[30] M. Binder, B. Galler, M. Furitsch, J. Off, J. Wagner, R. Zeisel, and S. Katz, “Investigations on correlation between I-V characteristic and internal quantum efficiency of blue (AlGaIn)N light-emitting diodes,” *Appl. Phys. Lett.*, vol. 103, no. 22, pp. 221110-1–4, 2013.

[31] Y. K. Kuo, M. C. Tsai, and S. H. Yen, “Numerical simulation of blue InGaN light-emitting diodes with polarization-matched AlGaInN electron-blocking layer and barrier layer,” *Opt. Commun.*, vol. 282, no. 21, pp. 4252–4255, 2009.

[32] S. Yamamoto, Y. Zhao, C. C. Pan, R. B. Chung, K. Fujito, J. Sonoda, S. P. DenBaars, and S. Nakamura, “High-efficiency single-quantum-well green and yellow-green light-emitting diodes on semipolar (20$\bar{2}$1) GaN substrates,” *Appl. Phys. Express*, vol. 3, no. 12, pp. 122102-1–3, 2010.

[33] P. Waltereit, O. Brandt, A. Trampert, H. T. Grahn, J. Menniger, M. Ramsteiner, M. Reiche, and K. . Ploog, “Nitride semiconductors free of electrostatic fields for efficient white light-emitting diodes,” *Nature*, vol. 406, no. 6798, pp. 865–868, 2000.

[34] D. L. Becerra, L. Y. Kuritzky, J. Nedy, A. Saud Abbas, A. Pourhashemi, R. M. Farrell, D. A. Cohen, S. P. DenBaars, J. S. Speck, and S. Nakamura, “Measurement and analysis of internal loss and injection efficiency for continuous-wave blue semipolar (2021) III-

nitride laser diodes with chemically assisted ion beam etched facets," *Appl. Phys. Lett.*, vol. 108, no. 9, pp. 91106-1–5, 2016.

[35] G. Muziol, M. Siekacz, H. Turski, P. Wolny, S. Grzanka, E. Grzanka, A. Nowakowska-siwi, I. Makarowa, P. Perlin, and C. Skierbiszewski, "High power nitride laser diodes grown by plasma assisted molecular beam epitaxy," *J. Cryst. Growth*, vol. 425, pp. 398–400, 2015.

[36] M. Martens, F. Mehnke, C. Kuhn, C. Reich, V. Kueller, A. Knauer, C. Netzel, C. Hartmann, J. Wollweber, J. Rass, T. Wernicke, M. Bickermann, M. Weyers, and M. Kneissl, "Performance characteristics of UV-C AlGaN-based lasers grown on sapphire and bulk AlN substrates," *IEEE Photonics Technol. Lett.*, vol. 26, no. 4, pp. 342–345, 2014.

[37] D. C. Kim, S. B. Bae, S. B. Kim, Y. H. Ko, Y. A. Leem, and E. S. Nam, "Anti-crossing effect and optimization of waveguide structure in InGaN/GaN/AlGaN laser diode on sapphire substrate," *Curr. Appl. Phys.*, vol. 16, no. 3, pp. 371–377, 2016.

[38] Z.-W. Zheng, M.-H. Lai, L.-Y. Ying, and B.-P. Zhang, "High-efficiency vertical-type InGaN/GaN multiple quantum well solar cells using aluminum reflectors," *2016 IEEE 16th Int. Conf. Nanotechnol.*, pp. 91–93, 2016.

[39] M. Arif, W. Elhuni, J. Streque, S. Sundaram, S. Belahsene, Y. El Gmili, M. Jordan, X. Li, G. Patriarche, A. Slaoui, A. Migan, R. Abderrahim, Z. Djebbour, P. L. Voss, J. P. Salvestrini, and A. Ougazzaden, "Improving InGaN heterojunction solar cells efficiency using a semibulk absorber," *Sol. Energy Mater. Sol. Cells*, vol. 159, no. September 2016, pp. 405–411, 2017.

[40] J. Bai, M. Athanasiou, and T. Wang, "Solar Energy Materials & Solar Cells Influence of the ITO current spreading layer on ef fi ciencies of InGaN-based solar cells," *Sol. Energy Mater. Sol. Cells*, vol. 145, pp. 226–230, 2016.

[41] C. J. Neufeld, N. G. Toledo, S. C. Cruz, M. Iza, S. P. DenBaars, and U. K. Mishra, "High quantum efficiency InGaN/GaN solar cells with 2.95 eV band gap," *Appl. Phys. Lett.*, vol. 93, no. 14, pp. 14–17, 2008.

CHAPTER 2
DENSITY FUNCTIONAL THEORY

2.1 INTRODUCTION

There are many fields within the physical sciences and engineering where the key to scientific and technological progress is to understand and control the properties of matter at the level of individual atoms and molecules. Density functional theory is a phenomenally successful approach to finding solutions to the fundamental equation that describes the quantum behavior of atoms and molecules, the Schrödinger equation in settings of practical value [1].

Density Functional Theory (DFT) is a ground-state theory in which the emphasis is on the charge density as the relevant physical quantity. DFT has proved to be highly successful in describing structural and electronic properties in a vast class of materials, ranging from atoms and molecules to simple crystals to complex extended systems (including glasses and liquids).

Furthermore, DFT has become a common tool in first-principles calculations aimed at describing – or even predicting – properties of molecular and condensed matter systems, it is so profoundly useful due to the generality of its precepts. It is a true ab-initio method which requires no parameters other than the crystal lattice and basis for the solid under investigation [2-3].

In this chapter, we will discuss the theory, methods and approximations used in the calculations, we begin a review of some quantum mechanics in order to lay the foundations for the theoretical discussion on density functional theory (DFT) key ideas from that underlie DFT. Density functional theory (DFT) is one of the most widely used technique obtainable on computational condensed matter physics, which was originally invented and developed by Kohn, Hohenberg, and Sham (Hohenberg and Kohn, 1964 [4]; Kohn and Sham, 1965 [5]), provides a modern tool to study the ground state properties of atoms, molecules, and solids. Our goal here is not to present a complete derivation of the techniques used in DFT. Instead, our goal is to give a clear**,** brief, introductory presentation of the most basic equations important for DFT.

2.2 DEFINITION OF DFT

Density Functional Theory, or DFT as she is more commonly known, was born during 1927, in the immediate aftermath of the Second Quantum Revolution. By the time of her death, two-thirds of a century later, she had inspired a revolution of her own and had launched the careers and reputations of an entire generation of professors and conference organizers [6].

Density-functional-based methods have revolutionized the way in which we calculate electronic structure theory, it has become an important tool in the treatment of many-body

problems in atomic, molecular, solid state, and nuclear physics [7]. The density contains enough information about the wave function, so that it can be used as the main variable to formulate quantum mechanics, with the obvious advantage that it is easier to deal with a global physical observable that depends only on 3 spatial coordinates and spin [8].

Based on the famous Hohenberg and Kohn theorems [4], DFT provided a sound basis for the development of computational strategies for obtaining information about the energetic, structure, and properties of (atoms and) molecules at much lower costs than traditional ab initio wave function techniques [9], It is a true ab-initio method which requires no parameters other than the crystal lattice and basis for the solid under investigation [3].

The greatest challenge in density-functional theory has been to successfully reformulate quantum mechanics in terms of the density, the main complication being that a practical form of the exact energy as a functional of the density is unknown [8].

2.3 Equation of Schrödinger

The first density-functional method dates back to the discovery of the Schrödinger equation [10]. The ultimate goal of most quantum chemical approaches is the – approximate – solution of the time-independent, non-relativistic Schrödinger equation:

$$H\psi = E\psi \qquad (2.1),$$

$$\hat{H}\psi_i(\vec{x}_1, \vec{x}_2, \dots, \vec{x}_N, \vec{R}_1, \vec{R}_2, \dots, \vec{R}_M) = E_i\psi_i(\vec{x}_1, \vec{x}_2, \dots, \vec{x}_N, \vec{R}_1, \vec{R}_2, \dots, \vec{R}_M) \qquad (2.2),$$

where $\hat{H}$ is the Hamilton operator for a molecular system consisting of M nuclei and N electrons in the absence of magnetic or electric fields. $\hat{H}$ is a differential operator representing the total energy:

$$\hat{H} = -\frac{1}{2}\sum_{i=1}^{N}\nabla_i^2 - \frac{1}{2}\sum_{A=1}^{M}\frac{1}{M_A}\nabla_A^2 - \sum_{i=1}^{N}\sum_{A=1}^{M}\frac{Z_A}{r_{iA}} + \sum_{i=1}^{N}\sum_{j>1}^{M}\frac{1}{r_{ij}} + \sum_{A=1}^{N}\sum_{B>A}^{M}\frac{Z_A Z_B}{R_{AB}} \qquad (2.3),$$

here, A and B run over the M nuclei while i and j denote the N electrons in the system. The first two terms describe the kinetic energy of the electrons and nuclei respectively, where the Laplacian operator ∇_q^2 is defined as a sum of differential operators (in Cartesian coordinates)

$$\nabla_q^2 = \frac{\partial^2}{\partial x_q^2} + \frac{\partial^2}{\partial y_q^2} + \frac{\partial^2}{\partial z_q^2} \qquad (2.4),$$

and M_A is the mass of nucleus A in multiples of the mass of an electron (atomic units).

The remaining three terms define the potential part of the Hamiltonian and represent the attractive electrostatic interaction between the nuclei and the electrons and the repulsive potential due to the electron-electron and nucleus-nucleus interactions, respectively.

r_{pq} (and similarly, R_{pq}) is the distance between the particles p and q, i. e.,

$$r_{pq} = |r_p - r_q|. \quad (2.5),$$

$\psi_i(\vec{x}_1, \vec{x}_2, \ldots, \vec{x}_N, \vec{R}_1, \vec{R}_2, \ldots, \vec{R}_M)$ stands for the wave function of the i'th state of the system, which depends on the $3N$ spatial coordinates $\{\vec{r}_i\}$, and the N spin coordinates $\{s_i\}$ of the electrons, which are collectively termed $\{\vec{x}_i\}$ and the $3M$ spatial coordinates of the nuclei, $\{\vec{R}_I\}$.

The wave function Ψ_i contains all information that can possibly be known about the quantum system at hand. Finally, E_i is the numerical value of the energy of the state described by Ψ_i [1-11].

2.4 Essential Aspects of DFT

Under the Born-Oppenheimer approximation [12], we are permitted to treat separately the electron potential due to the nuclei and due to the electrons, themselves. Let the potential due to the nuclei be V_{ext}; all electron-electron interactions (classical Coulomb potential, exchange-correlation potential) we denote V. With these assumptions, the many-body Hamiltonian is:

$$H = T + V + V_{ext} \quad (2.6),$$

with T the electron kinetic energy operator. The core of density functional theory is owed to Hohenberg and Kohn [4-5], who showed that the external potential exhibits a one-to-one correspondence with the ground state electron density, ρ. It is intuitive to students of quantum mechanics that V_{ext} determines ρ; density functional theory exists because the converse is also true. The consequences of that statement are far reaching, because given the external potential V_{ext}, the Hamiltonian H itself is uniquely determined. That is, the Hamiltonian, and thus the ground state total energy, is a functional of the ground state electron density. The ground state energy of the system may then be expressed (with the notation $f[x]$ indicating that f is a functional of x:

$$E_{V_{ext}}[\rho] = \langle\psi|T + V|\psi\rangle + \langle\psi| V_{ext}|\psi\rangle \quad (2.7),$$

$$= F_{HK}[\rho] + \int \rho(\vec{r})\ V_{ext}(\vec{r}) d\,\vec{r} \quad (2.8),$$

where F_{HK} is the Hohenberg-Kohn functional. Of course, the form of F_{HK} is not known explicitly. DFT is made a practical tool by the Kohn-Sham (KS) equations [4-5]. By further decomposing the Hohenberg-Kohn functional, the KS equations allow the energy functional to be written:

$$E_{\,V_{ext}}[\rho] = T_0[\rho] + V_{ext}[\rho] + V_{coul}[\rho] + V_{xc}[\rho] \quad (2.9),$$

where T_0 is the kinetic energy functional for a non-interacting electron gas, V_{coul} is the classical Coulomb potential, and V_{xc} is the (unknown) exchange-correlation functional. Couched in this way, the ground state energy of the inhomogenous interacting electron gas can be obtained by solving the wave equation for a single-particle Hamiltonian. That is, there exists a set of single-particle wave functions such that

$$H_{KS}\phi_i = \epsilon_i\phi_i \quad (2.10),$$

where H_{KS} is the KS Hamiltonian, and the exact ground state electron density of the N -electron system is given by:

$$\rho(\vec{r}) = \sum_i^N \phi_i\,(\vec{r})^*\phi_i(\vec{r}) \quad (2.11),$$

the set of $\{\phi_i\}$ does not represent actual electron wavefunctions here, nor are the $\{\epsilon_i\}$ single-electron energies; rather they are the eigenfunctions and eigenvalues, respectively, of the Kohn-Sham Hamiltonian.

2.5 EXCHANGE-CORRELATION POTENTIALS

The Kohn-Sham equations [13] are not useful without explicit definition of an exchange correlation functional $V_{xc}[\rho]$. The accuracy and precision of DFT calculations are influenced greatly by the functional that is chosen. A brief introduction to the varieties of approximation follows.

2.5.1 THE LOCAL DENSITY APPROXIMATION (LDA)

The most fundamental and simplest approximation is the local-density approximation (LDA), in which the energy depends only on the density at the point where the functional is evaluated (Kohn and Sham1965) [5]. LDA, which in essence assumes that the density corresponds to that of a homogeneous electron gas, proved to be an improvement over HF.

While LDA remains a major workhorse in solid state physics, its success in chemistry is at best moderate due to its strong tendency for overbinding [14].

This functional operates under the assumption that the inhomogeneous electron gas can be divided into differential elements of constant density, and that these elements contribute to the exchange-correlation energy identically to a homogenous electron gas of that density. That is,

$$V_{xc}{}^{LDA}[\rho] = \int \rho(\vec{r})\epsilon_{xc}(\rho(\vec{r}))d\,\vec{r} \qquad (2.10),$$

where $\rho(\vec{r}\,)$ is a function which is known numerically for the homogeneous electron gas. It can be extended to spin-polarized systems by separately accounting for spin-up and spin-down densities, in which case it is referred to as the local spin density approximation (LSDA):

$$V_{xc}{}^{LDA}[\rho_\uparrow, \rho_\downarrow\,] = \int \rho(\vec{r})\epsilon_{xc}(\rho_\uparrow(\vec{r}), \rho_\downarrow(\vec{r}))d\,\vec{r} \qquad (2.11).$$

The LDA and LSDA functionals have been shown to be successful in systems with slowly varying density. However, a notable failure of the LSDA functionals was exposed by results which found the nonmagnetic and antiferromagnetic fcc phases of iron to be more stable than the ferromagnetic bcc phase [15]. This inadequacy, along with others, prompted the development of functionals which accounted for neighboring density elements, i.e., density gradients.

2.5.2 The Generalized Gradient Approximation (GGA)

The first real breakthrough came with the creation of functional belonging to the so-called generalized gradient approximation (GGA) that incorporates dependence not only on the electron density but also on its gradient, thus being able to better describe the inhomogeneous nature of molecular densities. GGA functional such as BP86 (Becke1988) or PBE (Perdew et al.1996) [16] can be implemented efficiently and yield good results, particularly for structural parameters, but are often less accurate for other properties [14].

Many forms of GGA functionals exist, since the incorporation of the density gradient term is not explicitly stipulated (as opposed to the LDA, where ϵ_{xc} is well-defined). The functional in the GGA scheme takes the form

$$V_{xc}{}^{GGA}[\rho_\uparrow, \rho_\downarrow\,] = \int f(\rho_\uparrow(\vec{r}), \rho_\downarrow(\vec{r}), \nabla\rho_\uparrow(\vec{r}), \nabla\rho_\downarrow(\vec{r}))d\,\vec{r} \qquad (2.12),$$

where f is not uniquely defined. In comparison with LSDA, GGA functionals more accurately determine total energies and structural energy differences, as well as softening and expanding

bonds [16]. Care must also be taken in applying GGA, because there are cases where the LDA solutions are overcorrected, leading to underbinding. Examples of this can be seen in noble gas dimers and N2 molecular crystals, for which GGA predicts no binding [17].

2.6 Solving the Kohn-Sham Equations

What has been ignored above is that the electron density is an unknown in addition to the eigenfunctions of the KS Hamiltonian. In fact, the density depends on the solutions ϕ_m according to equation (2.11). This is then a self-consistency problem, in which the solution determines the equation to be solved. An initial guess of the density is made, and the KS equations are solved, after which the density is recomputed with the $\{\phi_m\}$. This density is used to repeat the cycle until the density arrived at converges on the input density. The process of solving the self-consistent KS equations [5] is essentially reduced to finding the correct coefficients to express the single-particle wave-functions in terms of the chosen basis:

$$H_{KS}\phi_m(\vec{r}) = \epsilon_m\phi_m(\vec{r}) \qquad (2.13),$$

$$\phi_m = \sum_{p=1}^{P} c_p\, \phi_p^b \qquad (2.14),$$

where the basis functions $\{\phi_p^b\}$ may be any orthonormal set. Plane waves are employed in some capacity in most popular codes applied to condensed matter, due to obvious connections with Bloch's theorem. In the interstitial regions between nuclei, valence electrons tend to behave similarly to free electrons, making the plane wave basis an efficient choice. It is in the electronic core, where the wave function may be both steep and oscillatory, that the choice of basis varies most.

2.7 Basis Functions for DFT

Basis sets, similarly to exchange-correlation functional, are an area of current development in DFT. An exhaustive catalogue of basis sets, and the theory behind them is beyond the scope of this thesis. Instead, what follows is an outline of the fundamental principles which are shared among basis sets currently in use.

2.7.1 Pseudopotential Methods

For many applications of ab initio codes, core electron energies and excitations are unimportant. This is true for many systems, in which chemical bonding is of primary interest, or in simulations of lattice vibrations, to give two examples. The pseudopotential (PP) in

question is the combined interaction potential of the nuclear attraction mediated by the electronic screening of the core.

The key advantage of the PP method is the computing efficiency it offers. By truncating the plane wave basis at a k value insufficient to accurately describe the potential near the nucleus, few plane waves are needed. Its disadvantages, of course, are the lack of insight provided into the behavior of the core electrons. For the subject of this thesis, in which core spin polarization and high pressures (which may cause core relaxation) are vitally important, pseudo-potential codes do not suffice [3].

2.7.2 FULL-POTENTIAL PLANE WAVE METHODS

The steep potential near the nucleus is no small impediment to the use of a pure plane-wave basis in the absence of a psuedopotential. So-called full-potential methods cope with this through the adoption of a combined basis set predicated on the subdivision of the unit cell into multiple atomic spheres and an interstitial region.

Physical intuition suggests that even in solids, electrons close to the nucleus have wave-functions which are atomic in nature; similarly, electrons far from the nucleus move in a much weaker potential and are more or less free. This scheme is illustrated in Figure.2.1.

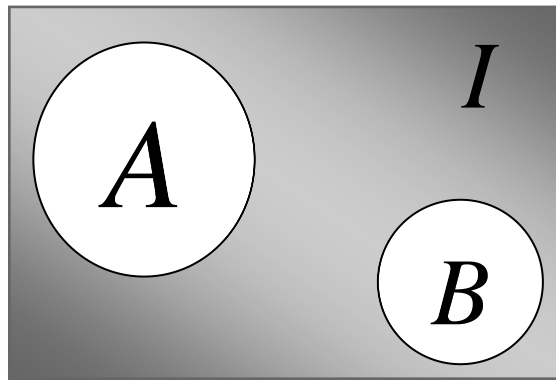

Figure.2.1 Schematic representation of the muffin-tin scheme for full-potential plane wave bases.

A and B represent atomic spheres for inequivalent atoms, and the shaded area I is the interstitial region.

In the region I in Figure.2.1, the plane waves take a familiar form:

$$\phi_{\vec{K}}^{\vec{k}}(\vec{r}) = \frac{1}{\sqrt{V}} e^{i(\vec{k}+\vec{K}).\vec{r}} \quad (2.15),$$

where $\vec{k}$ is a wave vector in the Brillouin zone, $\vec{K}$ is a reciprocal lattice vector, and V is the volume of the unit cell. Within the muffin-tin sphere, however, there are several choices that can be made. The Wien2k code [18], which was used for the work presented in this thesis, offers linearized augmented plane wave (LAPW).

As before, the LAPW has the form of equation (2.15) in the interstitial region. Within the muffin tin, the expansion of is done about

$$u_l^\alpha(r,E) = u_l^\alpha(r,E_0) + (E_0 - E)\dot{u}_l^\alpha(r,E_0) + \cdots \qquad (2.16),$$

again, the notation $\dot{u}$ indicates the first energy derivative. The muffin-tin form of the LAPW is then

$$\phi_{\vec{K}}^{\vec{k}}(\vec{r}) = \sum_{l,m}(A_{lm}^{\vec{k}+\vec{K}}\, u_l(r,E_0) + B_{lm}^{\vec{k}+\vec{K}}\dot{u}_l(r,E_0))Y_m^l(\hat{r}) \qquad (2.17),$$

and similarly, to the APW+LO method, $A_{lm}^{\vec{k}+\vec{K}}$ and $B_{lm}^{\vec{k}+\vec{K}}$ are found to enforce the necessary continuity conditions at the boundary of the atomic sphere.

2.8 Our use of DFT calculations in our own research

The application of density functional theory (DFT) calculations is rapidly becoming a “standard tool” for diverse materials modeling problems in physics, chemistry, materials science, and multiple branches of engineering. Although a number of highly detailed books and articles on the theoretical foundations of DFT are available, it remains difficult for a newcomer to these methods to rapidly learn the tools that allow him or her to actually perform calculations that are now routine in the fields listed above [1].

The Linearized Augmented Plane Wave (LAPW) method has proven to be one of the most accurate methods for the computation of the electronic structure of solids within density functional theory [19]. An important step toward the use of DFT in the study, Several codes were developed based on density functional theory (DFT) which became the most used, precise, and practical way to calculate the band structure of solids [9-20].

The overall implementation of the calculation of the band structure and optical properties of semiconductors with the WIEN2K code based on DFT which revolutionized the way in which we calculate electronic structure theory and gives better results and it’s theoretically well founded [8].

2.9 THE WIEN2K CODE APPROACH

A full-potential LAPW-code for crystalline solids has been developed over a period of more than twenty years. A first copyrighted version was called WIEN and it was published by P. Blaha, K. Schwarz, P. Sorantin, and S. B. Trickey, in Comput. Phys. Commun. 59, 399 (1990) [18-19].

WIEN consists of several independent programs described in more detail below. It is convenient, however, to have in mind a typical example of their use. Thus, LSTART is a modified (relativistic) atomic LSDA code used to generate starting potentials. There are two major parts in the program, the initialization and the self-consistent field (SCF) cycle the self-consistency cycle is pursued until certain convergence criteria are satisfied.

The calculations in this work are performed using the WIEN2k computer package (Blaha et al., 2014) [19]. This program contains several sub-programs, which are described briefly below. The flow chart of the code is given in Figure. 2.2.

• **Initialization** (Setting up the unit cell and generating the initial density): In this sub-program, atomic densities are generated and superimposed to obtain an initial crystal density for the SCF calculation. Additionally, the atomic potentials and, optionally, atomic valence densities are created. Information about l, m values of the lattice harmonics representation and number of Fourier coefficients of the interstitial charge density are inserted as input file in this part.

• **LAPW0** (Construction of the effective potential): — generates potential from density;

The Poisson equation is solved and the total potential is computed as the sum of the Coulomb and the exchange-correlation potential in the LAPW0 program. The electron (spin) density is used as input and the spherical (l = 0) and the non-spherical parts of the potential are generated. The exchange-correlation potential is computed numerically on a grid. Additionally, the Hellmann-Feynman force contribution to the force is also determined.

• **LAPW1** (Solving the Kohn-Sham equations of valence electrons): computes bands (eigenvalues and eigenvectors);

The Hamiltonian and the overlap matrix are set up in LAPW1. Their diagonalization provides the eigenvalues and eigenvectors. Both the LAPW and the APW+lo methods are supported. For maximum efficiency a mix of both is recommended, i.e. the APW+lo basis functions are

used for physically meaningful l values, while LAPW basis functions are employed to describe higher l-values functions.

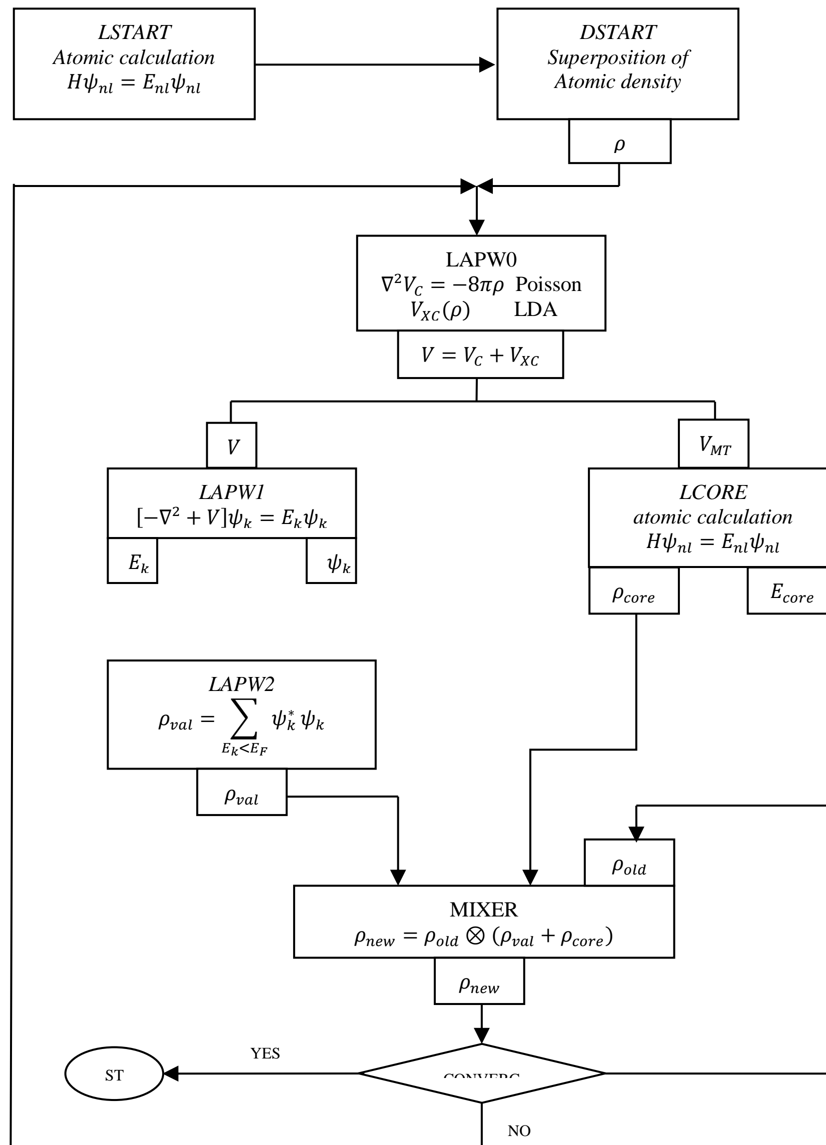

Figure.2.2 Flow chart of WIEN2k code.

• **LAPW2** (Construction of the new electron density) computes valence density from eigenvectors;

The Fermi-energy is computed. The electronic charge densities are expanded according to the representation of Eq.(III.17) for each occupied state and each k-vector. Afterwards the corresponding (partial) charges inside the atomic spheres are obtained by integration.

• **LCORE** (The treatment of the core electrons): compute core states and densities;

The potential and the charge density of the core electrons are computed.

• **LMIXER** (Generating the input density for the next iteration): mix input and output densities;

The electron densities of core, semi-core, and valence states are combined to yield the total new density. Taking only the new densities would, however, lead to instabilities in the iterative SCF process. To have a stable SCF cycle new and old densities need to be mixed, to obtain a new density.

2.10 CONCLUSIONS

In the present thesis many properties using WIEN2k have been investigated for a large variety of structures of the III-Nitrides binary, ternary and quaternary alloys, such as structural stability, density of states (DOS), partial density of states (PDOS) of constituent atoms, electronic band structure and optical properties.

LAPW calculations have helped to understand the structural, electronic and optical behavior of the solids. Super cells are also generated to enlarge the unit cells in all the three dimensions.

The results are reported in succeeding chapters.

REFERENCES

[1] D. S. Sholl and J. A. Steckel, *Density functional theory: A practical introduction*. John Wiley & Sons, Inc, 2009.

[2] D. M. Brink, "Density functional theory," *Nucl. Phys. News*, vol. 12, no. 4, pp. 27–32, 2002.

[3] A. B. Papandrew, *The Effects of High Pressure on the Vibrational and Magnetic Properties of Iron-Based Materials*. 2006.

[4] P. HOHENBERG and W. KOHN, "Inhomogeneous electron Gas," *Phys. Rev. B*, vol. 136, no. 3B, pp. 864–871, 1964.

[5] W. Kohn and L. J. Sham, "Self-consistent equations including exchange and correlation effects," *Phys. Rev.*, vol. 140, no. 4A, pp. A1131–A1138, 1965.

[6] P. M. W. Gill, "Obituary : Density Functional Theory (1927 – 1993)," *Aust. J. Chem.*, vol. 54, pp. 661–662, 2001.

[7] E. Runge and E. K. U. Gross, "Density-Functional Theory for Time-Dependent Systems," vol. 52, no. 12, pp. 997–1000, 1984.

[8] Miquel HUIX I ROTLANT, *Improved correlation kernels for linear-reponse time-dependent density-functinal theory*. 2011.

[9] P. Geerlings, F. De Proft, and W. Langenaeker, "Conceptual Density Functional Theory," *Chem. Rev.*, vol. 103, no. 5, pp. 1793–1873, 2003.

[10] E. Schrödinger, "An undulatory theory of the mechanics of atoms and molecules," *Phys. Rev.*, vol. 28, no. 6, pp. 1049–1070, 1926.

[11] W. Koch and M. C. Holthausen, *A Chemist 's Guide to Density Functional Theory*, 2nd editio., vol. 3. WILEY-VCH Verlag GmbH, 2001.

[12] M. Born and J R Oppenheimer, "On the Quantum Theory of Molecules," *Ann. Phys.*, vol. 84, no. 458, 1927.

[13] J. A. Pople, P. M. W. Gill, and B. G. Johnson, "Kohn—Sham density-functional theory within a finite basis set," *Chem. Phys. Lett.*, vol. 199, no. 6, pp. 557–560, 1992.

[14] M. Orio, D. A.Pantazis, and F. Neese, "Density functional theory," *Photosynth Res*, pp.

443–453, 2009.

[15] C. S. Wang, B. M. Klein, and H.Krakauer, "Theory of Magnetic and Structural Ordering in Iron," *Phys. Rev. Lett.*, vol. 54, no. 16, pp. 1852–1855, 1985.

[16] J. P. Perdew, K. Burke, and M. Ernzerhof, "Generalized Gradient Approximation Made Simple," *Phys. Rev. Lett.*, vol. 77, no. 18, pp. 3865–3868, 1996.

[17] J. Hafner, "ATOMIC-SCALE COMPUTATIONAL MATERIALS SCIENCE," *Acta Mater.*, vol. 48, pp. 71–92, 2000.

[18] P. Blaha, K. Schwarz, and P. Sorantin, "FULL-POTENTIAL, LINEARIZED AUGMENTED PLANE WAVE PROGRAMS FOR CRYSTALLINE SYSTEMS," *Comput. Phys. Commun.*, vol. 59, pp. 399–415, 1990.

[19] P. Blaha, K. Schwarz, G. Madsen, D. Kvasnicka, and J. Luitz, *WIEN2k*, WIEN2K_14., vol. 2. 2014.

[20] J.A.Camargo-Martinez and R. Baquero, "Performance of the modified Becke-Johnson potential for semiconductors," *Phys. Rev. B*, vol. 86, pp. 1–8, 2012.

CHAPTER 3
THE PROPERTIES OF THE ZINC-BLENDE ALGAINN ALLOYS

3.1 INTRODUCTION

The main objective of this chapter is to investigate the structural, electronic and optical properties of quaternary $Al_xGa_yIn_{1-x-y}N$ zinc-blende alloy using first-principles calculations. The plane-wave pseudopotential-based density functional theory (DFT) was implemented in the WIEN2K code employed throughout the work.

This chapter is arranged in three sections. The first part shows the computational method used in the work. The second section shows the results and discussions. Finally, the conclusion of this work is summarized in the final section.

3.2 COMPUTATIONAL DETAIL

Kohn, Hohenberg, and Sham's advanced density functional theory (DFT) provides a decent theoretical tool to probe the structural, electronic and optical properties of materials [1]. The present calculations are based on the density functional theory (DFT) which is implemented in WIEN2K code [2-3]. The generalized gradient approximation by Wu–Cohen GGA scheme [4-5] is used to treat electron exchange and correlation. The modified Becke-Johnson exchange potential [F. Tran and P. Blaha] (TB-mBJ) [6-7] is implemented to acquire a greater band gap value that is frequently underestimated by LDA and GGA [8], in which the states of $Al(3s^2 3p^1)$, $Ga(3d^{10} 4s^2 4p^1)$, $In(4d^{10} 5s^2 5p^1)$ and $N(2s^2 2p^3)$ are considered as valence electrons.

In this aim, we were using a supercell $(2 \times 2 \times 2)$ with 64 atoms. The model of crystal structures of $Al_{0.343}Ga_{0.625}In_{0.031}N$ quaternary alloys is shown in Figure.3.2. The GaN, AlN and InN compounds crystallize in both zinc blende (space group $F43m$) and wurtzite (space group $P63mc$) structure under ambient conditions. This study is using zinc-blende structure for all the concerned materials.

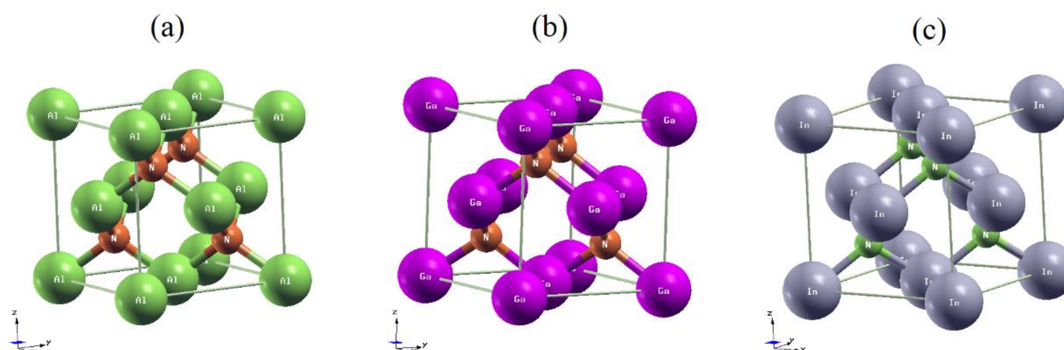

Figure.3.1 Illustration of a 1×1×1 conventional zinc-blende cell: (a) AlN, (b) GaN and (c) InN.

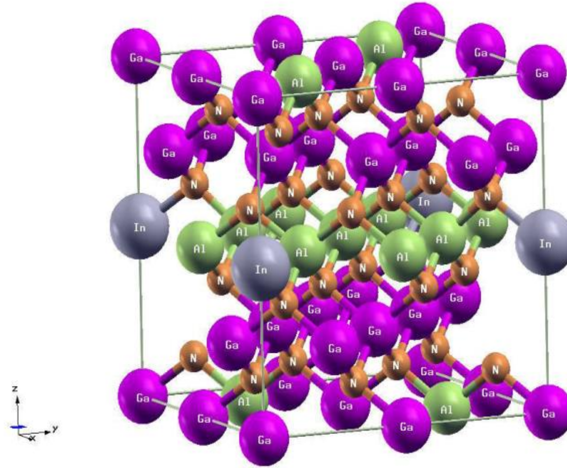

Figure.3.2 Illustration of a 2×2×2 zinc-blende $Al_{0.343}Ga_{0.625}In_{0.031}N$ supercell.

In FP-LAPW calculations, the unit cells are divided to nonoverlapping muffin-tin (MT) spheres [9]. To reach energy eigenvalues convergence, the wave function within the interstitial region was developed in terms of plane waves with a cut-off parameter of $RMT * Kmax = 7.0$ [3], where the RMT signifies the radius of muffin-tin (MT) sphere [10] equal to 1.79, 1.88, 1.98 and 1.58 (a.u) for Al, Ga, In and N, respectively, and $Kmax$ expresses largest K vector in the plane wave expansion [3]. The valence wave functions within the spheres are extended up to $lmax = 10$ [11], when the charge density was Fourier extended up to $Gmax = 12(a.u) - 1$ [12].

3.3 RESULTS AND DISCUSSION

3.3.1 STRUCTURAL PROPERTIES

The lattice matching condition for $Al_xGa_yIn_{1-x-y}N$ quaternary alloy matched to AlN is $y = 1,25(1-x)$. The Vegard's law [13] for the quaternary alloys allows us to write:

$$a_{Al_xGa_yIn_{1-x-y}N} = xa_{AlN} + ya_{GaN} + (1-x-y)a_{InN} \quad (3.1),$$

which the lattice constant of AlN, GaN and InN are denoted as a_{AlN}, a_{GaN} and a_{InN}, respectively.

J. Ohta et *al*. [15], reported that the growth of high-quality InN films is complicated, owing to diverse difficulties. The main issue resides in the low dissociation temperature of InN and the second is the affects of crystal growth of InN due to non-suitable substrates. The lattice

mismatch between InN and c-plane sapphire the common usually substrate, is about 29%. The lattice mismatch is given by,

$$(a_{Al_xGa_y\,In_{1-x-y}N} - a_{AlN})\times 100\%\,/a_{AlN} \quad (3.2),$$

implementing the equation (3.2) of our quaternary $Al_{0.343}Ga_{0.625}In_{0.031}N$, $Al_{0.468}Ga_{0.5}In_{0.031}N$ and $Al_{0.593}Ga_{0.25}In_{0.031}N$, the lattice mismatch is 2.05%, 1.82% and 1.36%, respectively for 3.12% of In amount, when incorporation is increased to 6.25%, the lattice mismatch will be 3.19%, 2.96% and 2.51%, respectively. Therefore, in this work we limit the indium incorporation to 3.12%.

The optimization procedure of the compounds binary (AlN, GaN, InN), ternary ($Al_{0.375}Ga_{0.625}N$, $Al_{0.5}Ga_{0.5}N$, $Al_{0.625}Ga_{0.375}N$) and quaternary ($Al_{0.343}Ga_{0.625}In_{0.031}N$, $Al_{0.468}Ga_{0.5}In_{0.031}N$ and $Al_{0.593}Ga_{0.25}In_{0.031}N$) alloys in this study utilizes the proposed energy function to obtain the structural parameters of the material [15]. In the volume optimization, we start the structure from an experimental data for the constituent pure binaries (AlN, GaN, InN).

Figure.3.2, shows the total energy versus volume curve for of the compounds binary (AlN, GaN, InN), Figure.3.3 the volume curves of the ternary ($Al_{0.375}Ga_{0.625}N$, $Al_{0.5}Ga_{0.5}N$, $Al_{0.625}Ga_{0.375}N$) and Figure.3.4 shows the quaternary volume curves ($Al_{0.343}Ga_{0.625}In_{0.031}N$, $Al_{0.468}Ga_{0.5}In_{0.031}N$ and $Al_{0.593}Ga_{0.25}In_{0.031}N$) alloys in cubic structure. The static equilibrium properties are obtained from these curves.

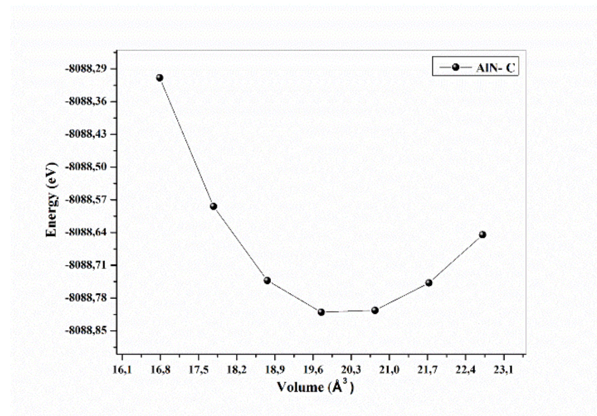

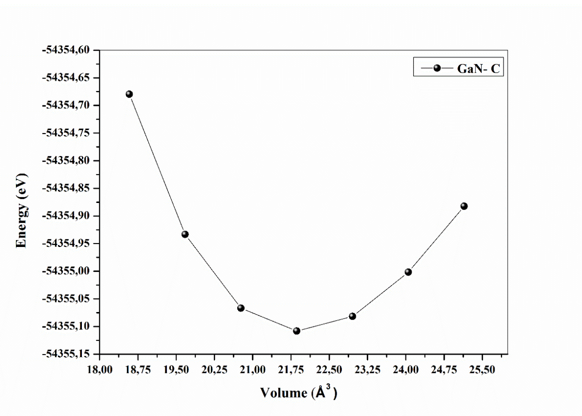

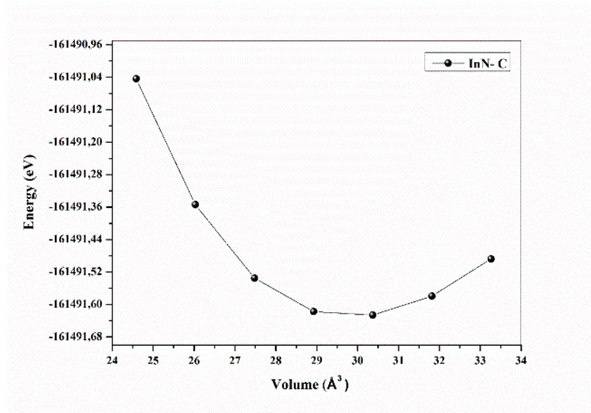

Figure.3.3 Total energy of AlN, GaN and InN as a function of volume.

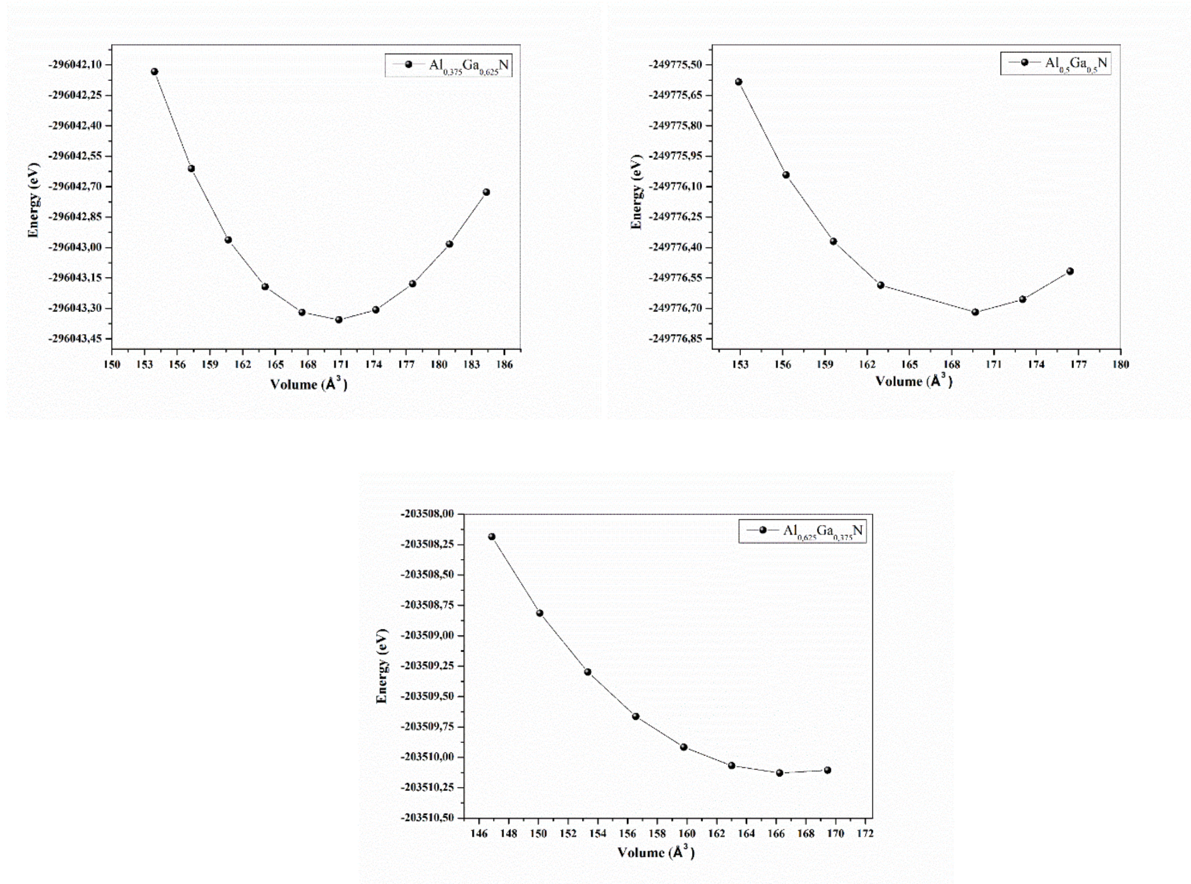

Figure.3.4 Total energy of $Al_{0.375}Ga_{0.625}N$, $Al_{0.5}Ga_{0.5}N$ and $Al_{0.625}Ga_{0.375}N$as a function of volume.

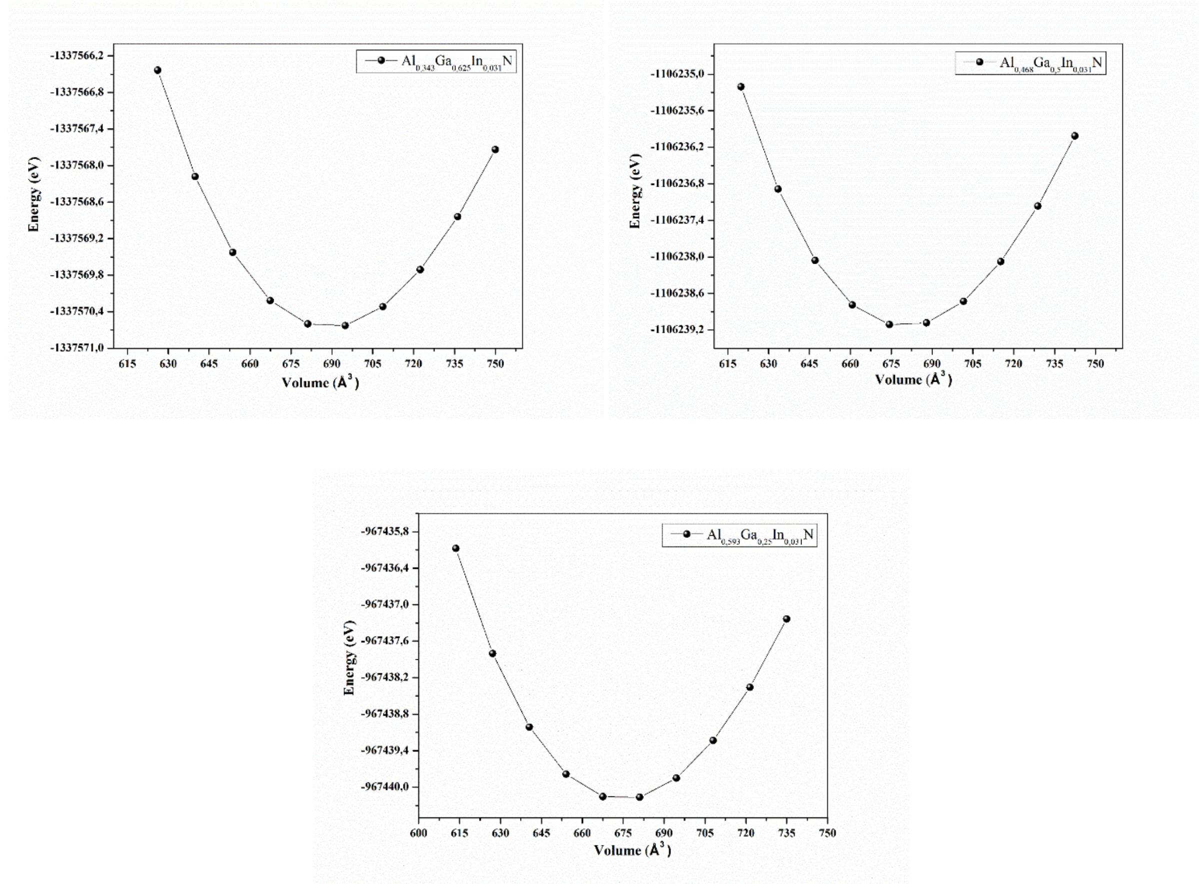

Figure.3.5 Total energy of $Al_{0.343}Ga_{0.625}In_{0.031}N$, $Al_{0.468}Ga_{0.5}In_{0.031}N$ and $Al_{0.593}Ga_{0.25}In_{0.031}N$ as a function of volume.

The WIEN2K code [16] permits the calculation of the equilibrium structural properties of the system, the equilibrium energy E_0, the Bulk modulus B_0, its first derivative B_0', and the balance volume at zero pressure V_0, by fitting using the EOS (equation of state) by Murnaghan [17],

$$E(V) = E_0 + \frac{B_0 V}{B'_0}\left[\frac{1}{B'_0 - 1}\left(\frac{V_0}{V}\right)^{B'_0} + 1\right] - \frac{B_0 V_0}{(B'_0 - 1)} \quad (3.3),$$

the calculated equilibrium lattice constant for the compounds are listed in Table 1 along with their respective bulk modulus, pressure derivatives in comparison with available earlier reports.

Table.3.1.

The lattice constant a, bulk modulus B and its first derivative B' of AlN, GaN, InN, $Al_{1-y}Ga_yN$ and $Al_xGa_yIn_{1-x-y}N$ compared to other experimental or theoretical data. VL indicated Vegard's law results in the table.

Material	a (Å)				B(GPA)		B'	
	Our	Other	VL	Exp	Our	Other	our	Other
AlN	4.38	4.34[a],4.37[c]	--	4.37[d],4.35[b]	202.19	201[c]	3.96	3.66[c]
GaN	4.50	4.46[a],4.49[c]	--	4.5[b], 4.50[d]	190.86	200[c]	4.53	4.75[c]
InN	4.98	4.95[a],4.99[f]	--	4.95[b],4.98[d]	136.49	136.60[f]	4.68	4.75[f]
$Al_{0.375}Ga_{0.625}N$	4.45	4.41[e]	4.45	--	196.06	--	4.30	--
$Al_{0.5}Ga_{0.5}N$	4.44	4.40[e]	4.44	--	196.80	--	4.26	--
$Al_{0.625}Ga_{0.375}N$	4.42	4.38[e]	4.42	--	198.35	--	4.23	--
$Al_{0.343}Ga_{0.625}In_{0.031}N$	4.47	--	4.47	--	192.47	--	4.32	--
$Al_{0.468}Ga_{0.5}In_{0.031}N$	4.46	--	4.46	--	194.74	--	4.26	--
$Al_{0.593}Ga_{0.25}In_{0.031}N$	4.44	--	4.44	--	195.81	--	4.18	--

[a] Ref.[18]. [b] Ref.[1]. [c] Ref.[9]. [d] Ref.[19]. [e] Ref.[20]. [f] Ref.[21].

Comparing our work with other reported data suggest a small difference due to different approximations. It is seen from the Table.3.1 that the calculated results of the lattice constants and bulk modulus for AlN, GaN and InN agrees well with the reported values in the literature.

The WC-GGA by Wu and Cohen is very suitable for the structural properties of solids [21], because of its closer experimental results especially with the binaries. In the $Al_xGa_yIn_{1-x-y}N$ and $Al_{1-y}Ga_yN$, we note that the diminution of the lattice constant is accompanied by an augmentation of the incorporation of the aluminum; therefore, the bulk modulus and its first pressure derivative increase linearly. We note that there are no available experimental data for the quaternary $Al_xGa_yIn_{1-x-y}N$

3.3.2 ELECTRONIC PROPERTIES

3.3.2.1 BAND STRUCTURE

At the equilibrium lattice, we calculated the electronic band structures for the zinc-blende binaries (AlN, GaN, InN), ternaries ($Al_{1-y}Ga_yN$) and quaternary ($Al_xGa_yIn_{1-x-y}N$); the WC-GGA and the mBJ-GGA approximations were implemented in the calculations of this properties. F.Tran et *al.* [7] shows that the modified Beck Johnson (TB-mBJ) estimates is very suitable for all types of solids and the agreement of results are accurate enough to help interpreting experimental data of the electronic band structures.

The energy band gap for the ternary and quaternary can be expressed as a function and obtained by the following equations:

i. For ternary: [22]

$$E_g(x) = (1-x)E_g(GaN) + xE_g(AlN) - bx(1-x) \tag{3.4}$$

where b is the bowing parameter, $E_g(GaN)$ the band gap of GaN and $E_g(AlN)$ the band gap of AlN. For the bowing b we use the value of reference [23], and for band gap, we use the experiment values $Eg(AlN) = 6.28$, $Eg(GaN) = 3.20$, $Eg(InN) = 0.70$ (eV) [7- 24]

ii. For the quaternary: [25]

$$E_g\left(Al_x\,Ga_{1-x-y}\,In_{\,y}N\right) = \frac{xyE_g^u(AlInN)+yzE_g^v(InGaN)+xzE_g^w(AlGaN)}{xy+yz+zx} \tag{3.5}$$

$$E_g^u(AlInN) = uE_g(InN) + (1-u)E_g(AlN) - u(1-u)B(AlInN) \tag{3.6}$$

$$E_g^v(InGaN) = vE_g(GaN) + (1-v)E_g(InN) - v(1-v)B(InGaN) \tag{3.7}$$

$$E_g^w(AlGaN) = wE_g(GaN) + (1-w)E_g(AlN) - w(1-w)B(AlGaN) \tag{3.8}$$

$$u = \frac{1-x+y}{2}\ ;\ v = \frac{1-y+z}{2}\ ;\ w = \frac{1-x+z}{2}\ ;\ z = 1-x-y \tag{3.9}$$

The band gap bowing parameters of $AlInN$, $InGaN$, and $AlGaN$ are $B(AlInN)$, $B(InGaN)$, and $B(AlGaN)$, their values are selected from reference [23].

Therefore, the calculated results obtained of energy at the point Γ of high-symmetry on the Brillouin zone for the binary, ternary and quaternary compounds using the WC-GGA, TB-mBJ and the two equations cited for ternary and quaternary using the bowing parameter are shown in Table.3.2, as well as the theoretical and experimental results issued by other researchers where appropriate.

Table.3.2.

The energy band gap E_g of AlN, GaN, InN, $Al_{1-y}Ga_yN$ and $Al_xGa_yIn_{1-x-y}N$ calculated with WC-GGA, TB-mBJ and Vegard's law compared to other experimental or theoretical data.

Material	Eg (eV)				
	WC-GGA	TB-mBJ	Calculations Eq. (3) and (4)	Exp	Others calculation
AlN	3.21	4.90	--	6.28[b], 5.94[a]	3.28[d], 5.09[d], 4.10[c], 3.31[g]
GaN	1.66	2.98	--	3.20[b], 3.30[a]	1.64[d], 2.88[d], 2.94[f],1.64[c], 1.74[g]
InN	0.00	0.66	--	0.70[g], 0.90[a]	0.00[d], 0.81[d], 0.66[f], 0.08[g]
$Al_{0.375}Ga_{0.625}N$	2.50	4.15	4.19	--	2.91[e]
$Al_{0.5}Ga_{0.5}N$	2.95	4.53	4.56	--	3.16[e]
$Al_{0.625}Ga_{0.375}N$	3.40	4.85	4.96	--	3.20[e]
$Al_{0.343}Ga_{0.625}In_{0.031}N$	2.68	3.70	3.89	--	--
$Al_{0.468}Ga_{0.5}In_{0.031}N$	2.96	4.00	4.06	--	--
$Al_{0.593}Ga_{0.25}In_{0.031}N$	3.17	4.19	4.24	--	--

[a] Ref.[18]. [b] Ref.[7]. [c] Ref.[9]. [d] Ref.[19]. [e] Ref.[20]. [f] Ref.[21]. [g] Ref.[24].

The calculation results of the approximations used in this framework analyzed starting with the binary compounds; a wide underestimation is obtained between the WC-GGA and experimental data of 48.75%, 48.09% and 100% for AlN, GaN, and InN, respectively. Using TB-mBJ approximations the divergence decreases to 21.84%, 6.87%, 4.71%, respectively, for the same binary.

For the ternary and quaternary, the respective WC-GGA underestimation is 41.25%, 34.87%, 29.97%, 27.56%, 26.11% and 24.43% for the $Al_{0.375}Ga_{0.625}N$, $Al_{0.5}Ga_{0.5}N$, $Al_{0.625}Ga_{0.375}N$, $Al_{0.343}Ga_{0.625}In_{0.031}N$, $Al_{0.468}Ga_{0.5}In_{0.031}N$ and $Al_{0.593}Ga_{0.25}In_{0.031}N$. Hence, the TB-mBJ occur an excellent accord to the results of the two equations. (3.4) and (3.5) data, with divergence of 1.65%, 0.76%, 2.05%, 4.88%, 1.33% and 1.06%, demonstrating the accurate results of TB-mBJ for semiconductor compounds.

While the calculated band gap for semiconductor using the LDA and GGA are undervalued, A.Shaukat et. *al* [26], reported that the self-interaction error and the lack of derivative discontinuity in the exchange-correlation potential produce an important underestimation (up to 50%) of the band gap.

It is obviously possible to see the nature of the band gap of the quaternary. It is interesting to note that we have a direct band gap [26], where the valence band peak and the lowest conduction band are in the same point of symmetry Γ as shown in Figure.3.6 and , with the band structures plotted for the ternary $Al_{0.375}Ga_{0.625}N$, $Al_{0.5}Ga_{0.5}N$ and $Al_{0.625}Ga_{0.375}N$ using TB-mBJ

and the plotted band structures for the quaternary $Al_{0.343}Ga_{0.625}In_{0.031}N$, $Al_{0.468}Ga_{0.5}In_{0.031}N$ and $Al_{0.593}Ga_{0.25}In_{0.031}N$ using TB-mBJ in Figure.3.7.

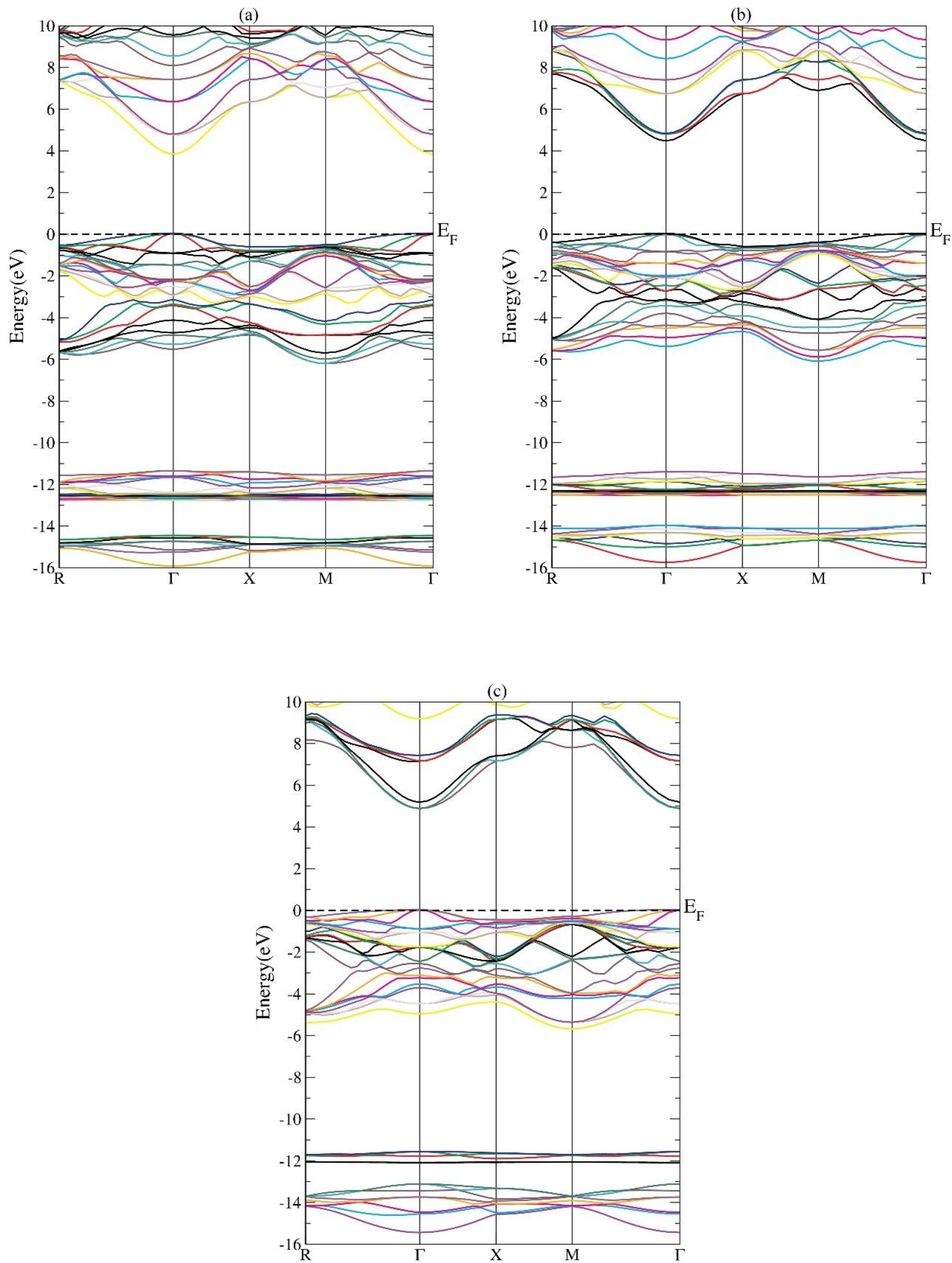

Figure.3.6 Band structures within TB-mBJ at the lattice constant for (a) $Al_{0.375}Ga_{0.625}N$, (b) $Al_{0.5}Ga_{0.5}N$ and (c) $Al_{0.625}Ga_{0.375}N$.

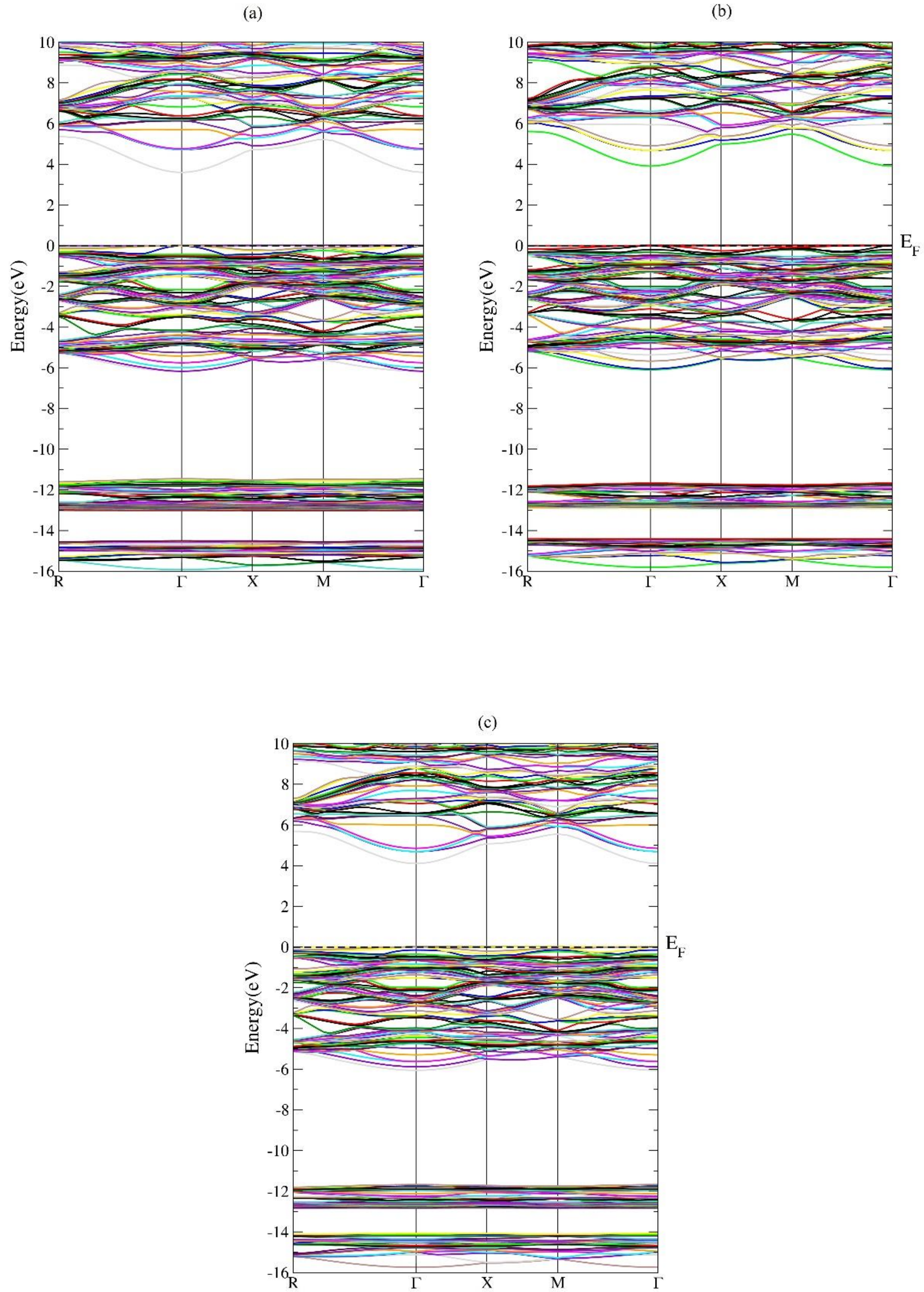

Figure.3.7 Band structures within TB-mBJ at the lattice constant for (a) $Al_{0.343}Ga_{0.625}In_{0.031}N$, (b) $Al_{0.468}Ga_{0.5}In_{0.031}N$ and (c) $Al_{0.593}Ga_{0.25}In_{0.031}N$.

The following equation could calculate the wavelength from E_g,

$$E_g(eV) = 1240/\lambda(nm) \tag{3.10}$$

The wavelengths calculated from Equation (3.10) are 298.79 nm, 273.73 nm and 255.67 nm for the respective ternary $Al_{0.375}Ga_{0.625}N$, $Al_{0.5}Ga_{0.5}N$ and $Al_{0.625}Ga_{0.375}N$, and 335.135 nm, 309.53 nm, and 295.58 nm for $Al_{0.343}Ga_{0.625}In_{0.031}N$, $Al_{0.468}Ga_{0.5}In_{0.031}N$ and $Al_{0.593}Ga_{0.25}In_{0.031}N$ quaternary, respectively. These wavelengths are in the UV spectrum range, which confirms that our compounds can be incredibly engaging to fabricate ultraviolet components such as emitters and detectors [22].

3.3.2 .2 DENSITIES OF STATES DOS

In order to obtain deeper knowledge of the electronic structure for our ternary and quaternary alloys, the electronic density of states (DOS) depicts the number of states through an interval of energy at every energy level which is possible to be occupied.

a. For the ternary

Calculated density of states (DOS) of $Al_{0.375}Ga_{0.625}N$, $Al_{0.5}Ga_{0.5}N$ and $Al_{0.625}Ga_{0.375}N$, using the TB-mBJ scheme are shown in Figure.3.8, with the plot of the total and the partial densities of states (TDOS and PDOS). The vertical red dashed line is the Fermi level which is set to be zero. In Figure.3.8, it is clear to observe in the valence band that the electronic density contains two essential sub-bands, the narrowband between -12 to -11.26 eV and the wideband between -6 eV to fermi level. The PDOS is split into: s, p, and d orbitals. We can analyze that the narrowband had a high peak due to the atomic s orbital of the N atoms with the addition of Ga-p and Al-p. The wideband contain two peaks, the first from -6 to -3.68 eV have a combination from several N-p, Ga-s, and Al-s/p, while the second peak between -3.68 to 0.00 eV comprises of the N-p, the Ga-p/d orbital of and Al-s/p orbital.

The confined part subsequent to the Fermi level and the conduction band indicates that of the bandgap energy of the ternary $Al_{0.375}Ga_{0.625}N$, $Al_{0.5}Ga_{0.5}N$ and $Al_{0.625}Ga_{0.375}N$ are 4.15, 4.53 and 4.85 eV. Those dominant states of the conduction band, $the\ orbital\ Al/Ga-s, and\ the\ states\ Al/Ga/N-p.$

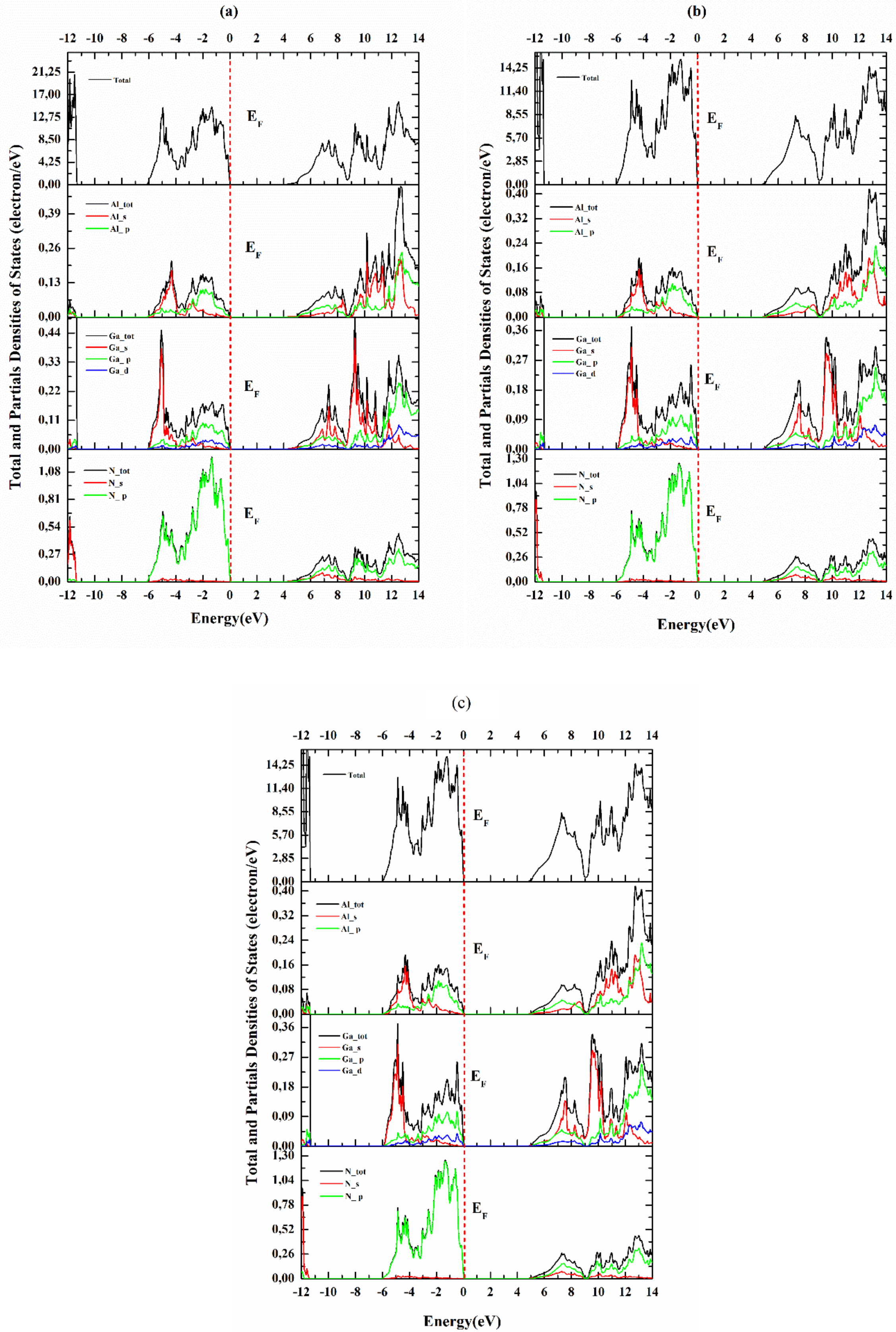

Figure.3.8 Total and partial densities of states for (a) $Al_{0.375}Ga_{0.625}N$, (b) $Al_{0.5}Ga_{0.5}N$ and (c) $Al_{0.625}Ga_{0.375}N$ compounds.

b. For the quaternary

Calculated density of states (DOS) of $Al_{0.343}Ga_{0.625}In_{0.031}N$, $Al_{0.468}Ga_{0.5}In_{0.031}N$ and $Al_{0.593}Ga_{0.25}In_{0.031}N$, using the TB-mBJ scheme are shown in Figure.3.9, with the plot of the total and the partial densities of states (TDOS and PDOS). The vertical red dashed line is the Fermi level which is set to be zero. In Figure.3.9, it is clear to observe in the valence band that the electronic density contains three essential sub-bands, the narrowband between -15.51 to -14.02 eV, the second between -13.23 to -11,11eV and the wideband between -6.92 eV to Fermi level. The PDOS is split into: s, p, and d orbitals. We can analyze that the narrowband had a high peak due to the atomic d orbital of the Ga and In atoms with the addition of N-s and Al-p. The middle band ward contributed by the d orbital of Ga and In (Ga/In-d) with a small mixture of N-s. The wideband contain two peaks, the first from -6.92 to -4.19 eV have a combination from several N-p, In-s, Ga-s, and Al-s, while the second peak between -4.19 to 0.00 eV comprises of the N-p, the In-p/d orbital of and Ga/Al-p orbital. The confined part subsequent to the Fermi level and the conduction band indicates that of the bandgap energy of the quaternary $Al_{0.343}Ga_{0.625}In_{0.031}N$, $Al_{0.468}Ga_{0.5}In_{0.031}N$ and $Al_{0.593}Ga_{0.25}In_{0.031}N$ are 3.70, 4.00, and 4.19 eV, respectively.

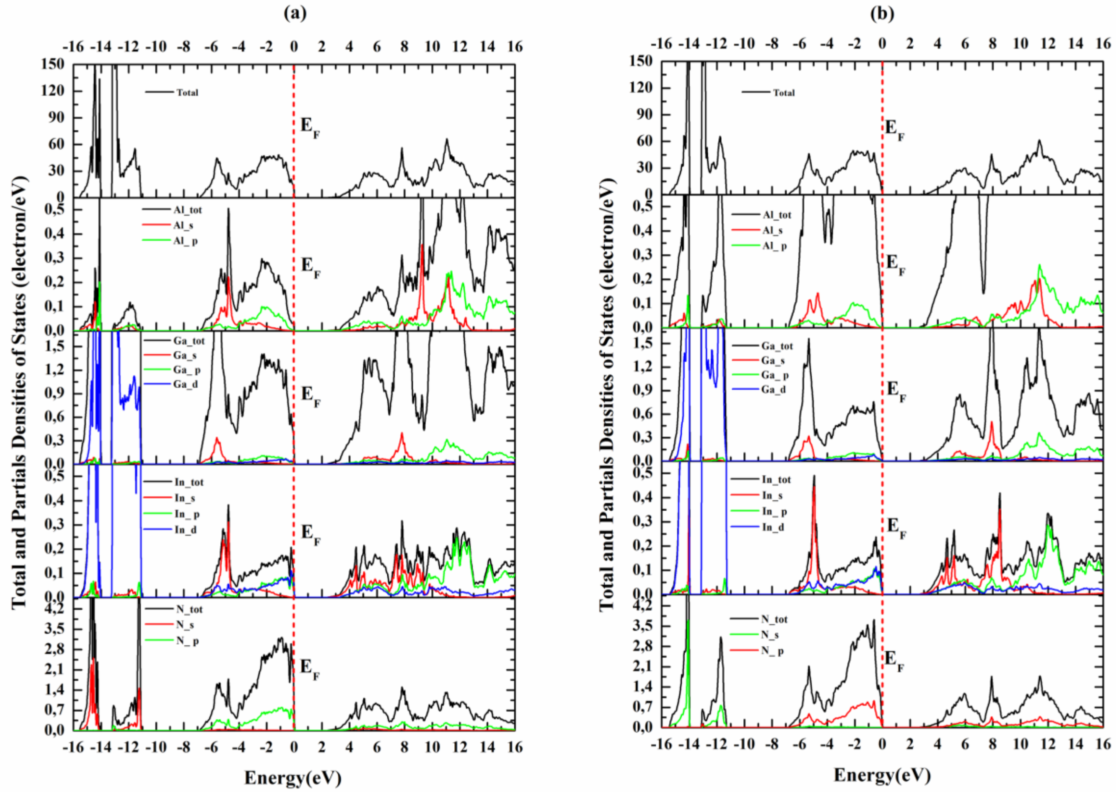

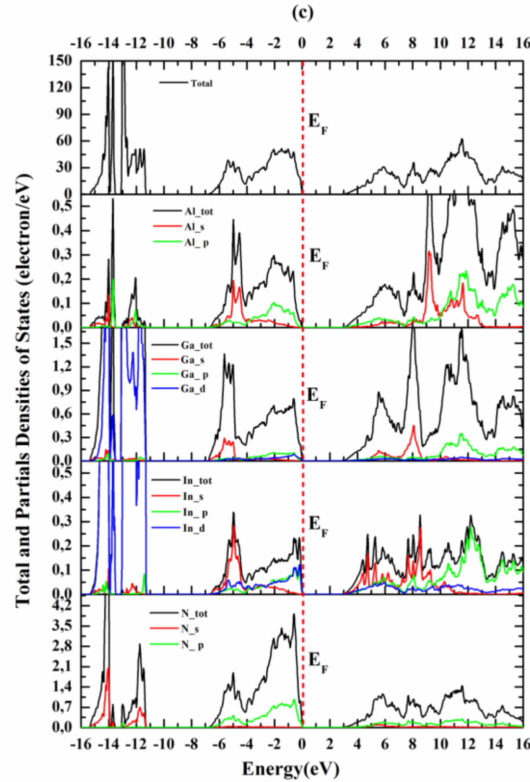

Figure.3.9 Total and partial densities of states for (a) $Al_{0.343}Ga_{0.625}In_{0.031}N$, (b) $Al_{0.468}Ga_{0.5}In_{0.031}N$ and (c) $Al_{0.593}Ga_{0.25}In_{0.031}N$ compounds.

Those dominant states of the conduction band, the orbital In/Al-s, and the states In/Al-p, reveals that the incorporation of indium (In) resulted to diminish the bandgap energy.

3.3.3 Optical properties

This section provides a number of optical properties of the ternary $Al_{0.375}Ga_{0.625}N$, $Al_{0.5}Ga_{0.5}N$ and $Al_{0.625}Ga_{0.375}N$ and the quaternary $Al_{0.343}Ga_{0.625}In_{0.031}N$, $Al_{0.468}Ga_{0.5}In_{0.031}N$ and $Al_{0.593}Ga_{0.25}In_{0.031}N$ using the TB-mBJ exchange potential to calculate the optical properties because of the improved bandgap energy, a dense mesh of uniformly distributed k-points must be used to obtain the excellent optical spectra of the dielectric function $\varepsilon(\omega)$. Therefore, the Brillouin zone *(BZ)* integration was achieved with 126 *k*-points into the irreducible part of the *(BZ).* The calculation results have been investigated in the energy range up to 34 eV. However, to the best of our knowledge, there are no experimental and theoretical study of optical properties of the quaternaries.

The optical functions are developed from the complex dielectric function $\varepsilon(\omega)$, which can depict the optical properties of the medium at all photon $E = \hbar\omega$,

$$\varepsilon(\omega) = \varepsilon_1(\omega) + i\varepsilon_2(\omega) \quad (3.11),$$

wherever $\varepsilon_1(\omega)$ and $\varepsilon_2(\omega)$ are the real (dispersive) and the imaginary (absorptive) parts of $\varepsilon(\omega)$ [27-28], respectively. The imaginary part of the dielectric function, $\varepsilon_2(\omega)$ is obtained from the momentum matrix elements [29], and the electronic structure calculation (densities of states). The real part $\varepsilon_1(\omega)$ can be derived from the $\varepsilon_2(\omega)$, using the Kramer-Kronig transformations [30]. From $\varepsilon_1(\omega)$ and $\varepsilon_2(\omega)$, we gather the other optical parameters such as the absorption coefficient $\alpha(\omega)$, reflectivity $R(\omega)$, refractive index $n(\omega)$ and the extinction coefficient $k(\omega)$: [27-31]

$$n(\omega) = \sqrt{\frac{(\varepsilon_1(\omega)^2+\varepsilon_2(\omega)^2)^{1/2}+\varepsilon_1(\omega)}{2}} \quad (3.12),$$

$$k(\omega) = \sqrt{\frac{(\varepsilon_1(\omega)^2+\varepsilon_2(\omega)^2)^{1/2}-\varepsilon_1(\omega)}{2}} \quad (3.13),$$

the complex refractive index $n^*(\omega)$, presented as the following equation:

$$n^*(\omega) = n(\omega) + ik(\omega) = \sqrt{\varepsilon(\omega)} = \sqrt{\varepsilon_1(\omega) + i\varepsilon_2\,(\omega)} \quad (3.14).$$

For the absorption coefficient *α(ω)* and normal-incidence reflectivity *R(ω)*,

$$\alpha(\omega) = \frac{4\pi}{\lambda} k(\omega) \quad (3.15),$$

$$R(\omega) = \frac{(n(\omega)-1)^2+k(\omega)^2}{(n(\omega)+1)^2+k(\omega)^2} \quad (3.16),$$

where λ is the wavelength of light in the vacuum.

The real and imaginary part of the dielectric function for the ternary $Al_{0.375}Ga_{0.625}N$, $Al_{0.5}Ga_{0.5}N$ and $Al_{0.625}Ga_{0.375}N$ are displayed in Figure.3.10 while Figure.3.11 for the quaternary $Al_{0.343}Ga_{0.625}In_{0.031}N$, $Al_{0.468}Ga_{0.5}In_{0.031}N$ and $Al_{0.593}Ga_{0.25}In_{0.031}N$. The imaginary part of the dielectric function indicates that the threshold energy (the first critical point *A*) appear at 4.15, 4.53, 4.85, 3.70, 4.00 and 4.19 eV for the respective $Al_{0.375}Ga_{0.625}N$, $Al_{0.5}Ga_{0.5}N$, $Al_{0.625}Ga_{0.375}N$ $Al_{0.343}Ga_{0.625}In_{0.031}N$, $Al_{0.468}Ga_{0.5}In_{0.031}N$ and $Al_{0.593}Ga_{0.25}In_{0.031}N$. As shown in band structure (Figure.3.6 and Figure.3.7) the point *A* represents the direct optical transitions between the top of the valence band and the bottom of the conduction band at $\Gamma_{15v} - \Gamma_{1c}$ symmetry point, which is identified as the fundamental absorption edge. Beyond these points, the curves increase rapidly with different main peaks (*B*, *C*, and *D*), appearing the

resonance behavior. This resonance behavior for the ternary compounds is related to the shift from occupied N-p, the Ga-p/d orbital of and Al-s/p orbital localized in highest valence band to unoccupied orbital Al/Ga-s and the states $Al/Ga/N$-p localized in lowest conduction band. For the quaternary the resonance behavior related to the shift from occupied Al-p, Ga-p/d, In-p/d, and N-p states localized in highest valence band to unoccupied Al-p, Ga-s, In-s, and N-s/p states localized in lowest conduction band along R, Γ and X symmetry direction in the Brillouin zone.

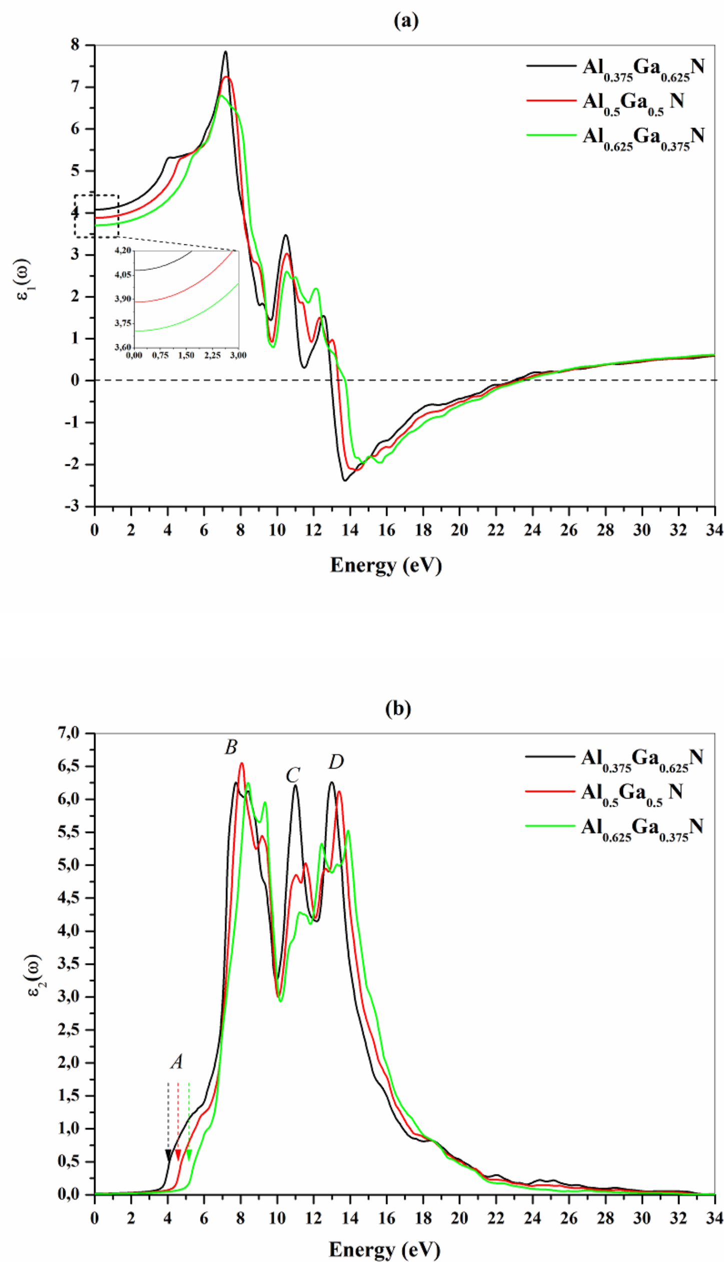

Figure.3.10 Real part $\varepsilon_1(\omega)$ (a) and imaginary part $\varepsilon_2(\omega)$ (b) for $Al_{0.375}Ga_{0.625}N$, $Al_{0.5}Ga_{0.5}N$ and $Al_{0.625}Ga_{0.375}N$ compounds.

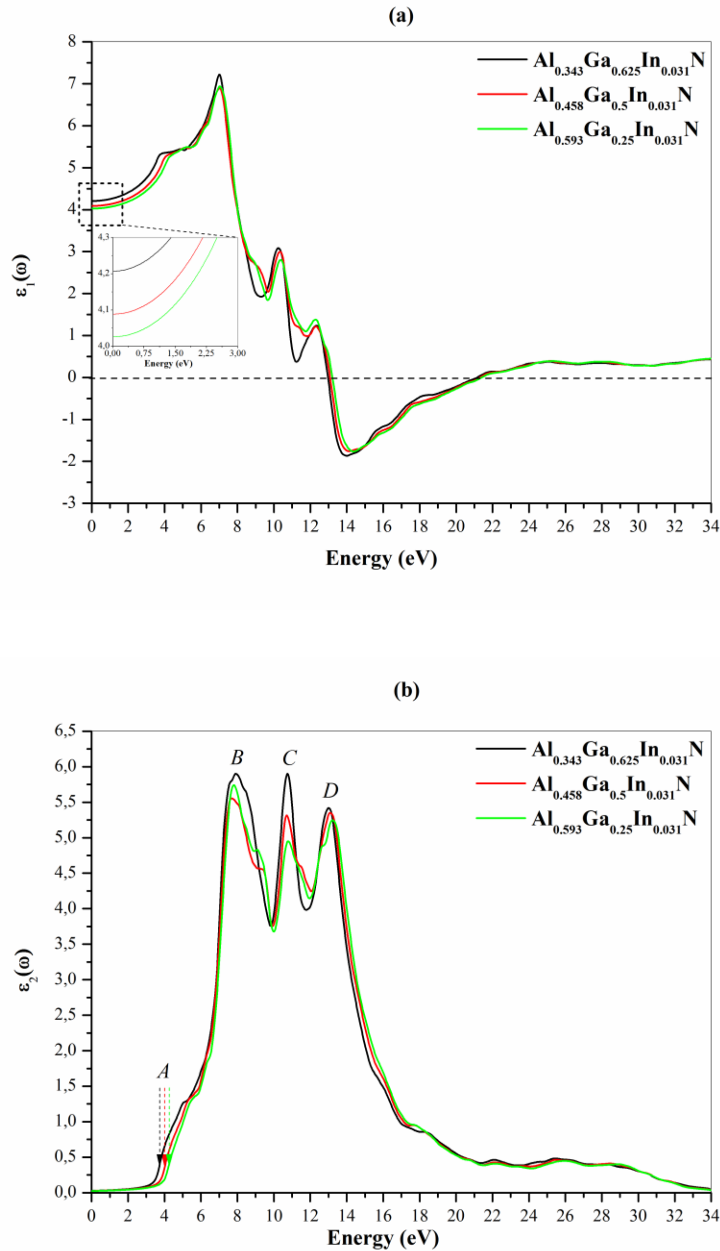

Figure.3.11 Real part $\varepsilon_1(\omega)$ (a) and imaginary part $\varepsilon_2(\omega)$ (b) for $Al_{0.343}Ga_{0.625}In_{0.031}N$, $Al_{0.468}Ga_{0.5}In_{0.031}N$ and $Al_{0.593}Ga_{0.25}In_{0.031}N$ compounds.

Table.3.3

Collected the peak positions of $\varepsilon_2(\omega)$, static dielectric constant $\varepsilon_1(0)$, refractive index $n(0)$ and Static reflectivity $R(0)$ for $Al_{0.375}Ga_{0.625}N$, $Al_{0.5}Ga_{0.5}N$, $Al_{0.625}Ga_{0.375}N$, $Al_{0.343}Ga_{0.625}In_{0.031}N$, $Al_{0.468}Ga_{0.5}In_{0.031}N$ and $Al_{0.593}Ga_{0.25}In_{0.031}N$ compounds.

Materials	Critical points				Static dielectric constant	Static refractive index	Static reflectivity
	A	B	C	D	$\varepsilon_1(0)$	$n(0)$	$R(0)$
$Al_{0.375}Ga_{0.625}N$	4.15	7.71	10.97	12.97	4.45	2.020	0.1139
$Al_{0.5}Ga_{0.5}N$	4.53	8.06	11.53	13.38	3.86	1.975	0.1071
$Al_{0.625}Ga_{0.375}N$	4.85	8.39	12.40	13.85	3.72	1.917	0.1006
$Al_{0.343}Ga_{0.625}In_{0.031}N$	3.70	7.93	10.75	13.00	4.21	2.052	0.1187
$Al_{0.468}Ga_{0.5}In_{0.031}N$	4.00	7.66	10.71	13.10	4.08	2.021	0.1143
$Al_{0.593}Ga_{0.25}In_{0.031}N$	4.19	7.82	1.78	13.22	4.02	2.006	0.1120

The static dielectric function $\varepsilon_1(0)$ is an important parameter from which we can calculate band gap value from the relation:

$$\varepsilon \approx 1 + (\hbar\omega_p/E_g)^2 \quad (3.18),$$

we note that a smaller energy gap yields a larger $\varepsilon_1(0)$ value. This could be clarified on the basis of the Penn model [28-32-33]. It can be seen that our results collected in Table.3.3 are in good agreement with the relation (3.18).

The refractive index $n(\omega)$ and reflectivity $R(\omega)$ are shown in Figure.3.12 for the ternary $Al_{0.375}Ga_{0.625}N$, $Al_{0.5}Ga_{0.5}N$ and $Al_{0.625}Ga_{0.375}N$ and for the quaternary $Al_{0.343}Ga_{0.625}In_{0.031}N$, $Al_{0.468}Ga_{0.5}In_{0.031}N$ and $Al_{0.593}Ga_{0.25}In_{0.031}N$ in Figure.3.13. The interaction of light with electrons of the constituent atoms, define the refractive index $n(\omega)$ [34]. The first deep insight to the refractive index spectrum of Figure.3.12 and Figure.3.13, the $n(\omega)$ increase with the increase of photon energy at inferior energies. Therefore, three main peaks in the curves correspond to inter-band transitions, the highest peak occurs at 2.89, 2.79 and 2.65 $a.u$ for the ternary. Increasing the Al amount, the first peaks move to 2.16, 2.02 and 1.89 $a.u$ and the lowest peaks were found at 1.89, 1.79 and 1.93 $a.u$ for all the three-considered ternary in Figure.3.12.

The highest peak occurs at 2.77 $a.u$ for $Al_{0.343}Ga_{0.625}In_{0.031}N$. Increasing the Al amount, the first peaks move to 2.72 and 2.71 $a.u$, for $Al_{0.468}Ga_{0.5}In_{0.031}N$ and $Al_{0.593}Ga_{0.25}In_{0.031}N$, respectively. The second peaks occur at 2.11, 2.06 and 2.00 $a.u$, and the lowest peaks were found at 1.74, 1.72 and 1.75 $a.u$, for all the three-considered quaternary in Figure.3.13. The highest refractive index is reached for photon energy around 7.16 and 7.09 eV for the respective

$Al_{0.375}Ga_{0.625}N$ and $Al_{0.343}Ga_{0.625}In_{0.031}N$ are related mainly to A transition of 4.15 and 3.70 eV.

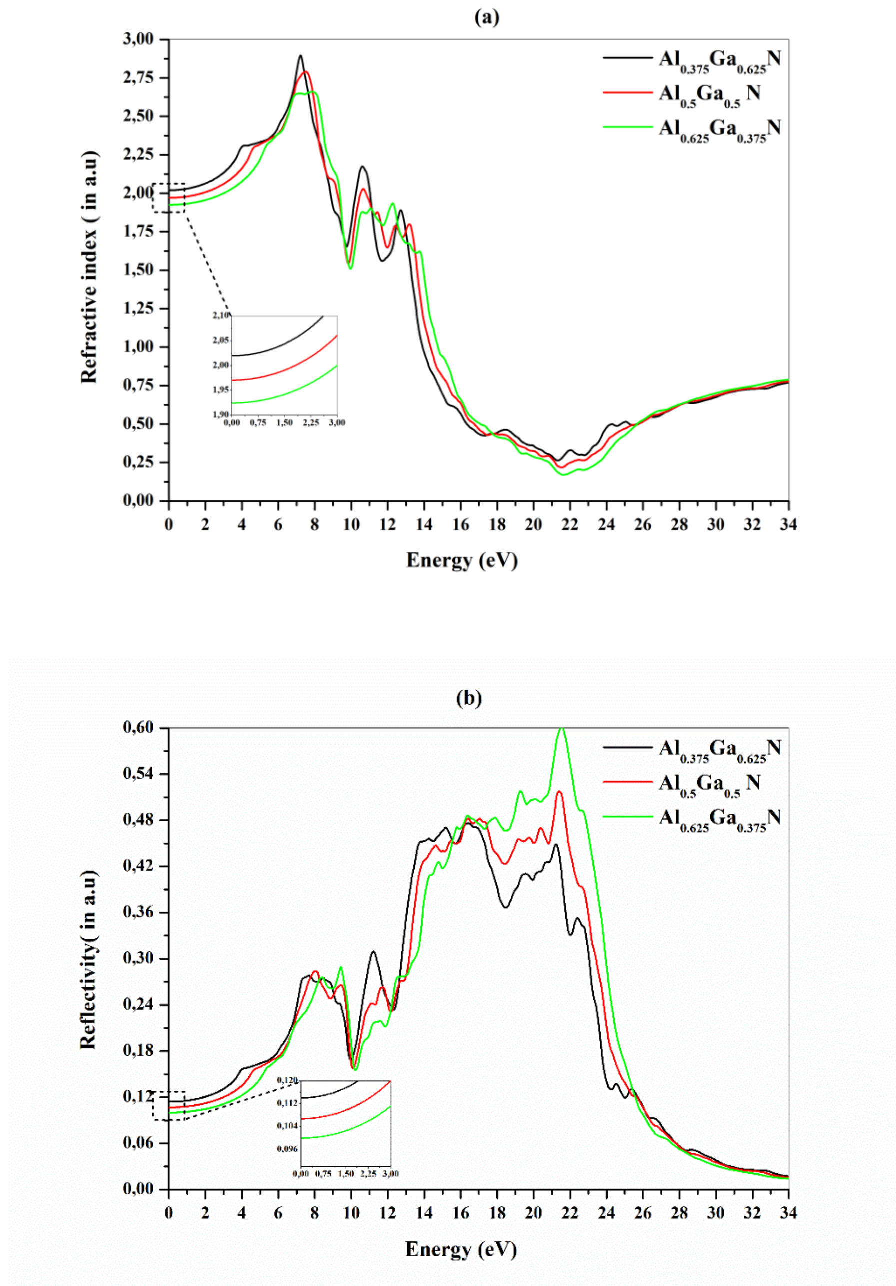

Figure.3.12 refractive index $n(\omega)$ (a) and reflectivity $R(\omega)$ (b) for $Al_{0.375}Ga_{0.625}N$, $Al_{0.5}Ga_{0.5}N$ and $Al_{0.625}Ga_{0.375}N$ compounds.

Furthernmore, as shown in Figure.3.12 and Figure.3.13, the first peak of reflectivity is at 4.19, 4.68, 5.20, 3.83, 4.20, and 4.44 eV (near A transition) and the maximum reflectivity explained by the resonance plasmon arising in the ultraviolet range, occurs in the energy regions of (7.16, 21.64) eV, (7.36, 21.91) eV, (7.51, 22.30) eV, (7.09, 19.74) eV, (7.26, 20.17)

eV and, (7.34, 20.39) eV for $Al_{0.375}Ga_{0.625}N$, $Al_{0.5}Ga_{0.5}N$, $Al_{0.625}Ga_{0.375}N$, $Al_{0.343}Ga_{0.625}In_{0.031}N$, $Al_{0.468}Ga_{0.5}In_{0.031}N$ and $Al_{0.593}Ga_{0.25}In_{0.031}N$ compounds, respectively.

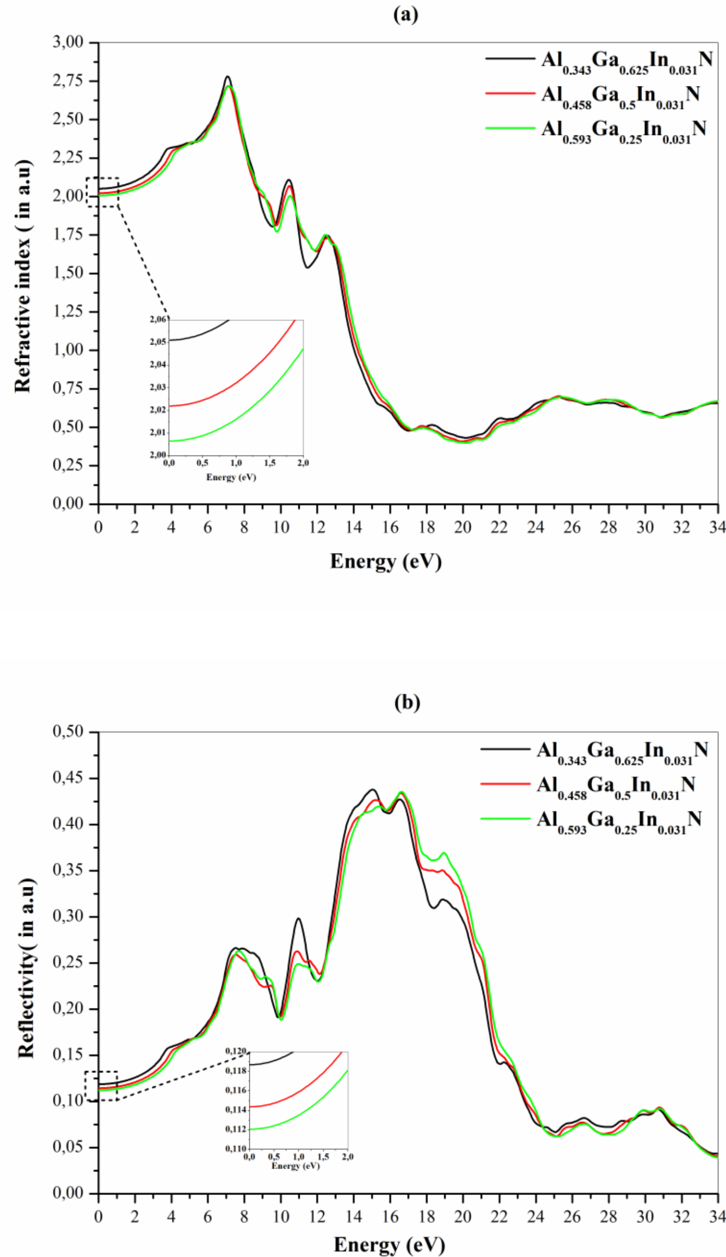

Figure.3.13 refractive index $n(\omega)$ (a) and reflectivity $R(\omega)$ (b) for $Al_{0.343}Ga_{0.625}In_{0.031}N$, $Al_{0.468}Ga_{0.5}In_{0.031}N$ and $Al_{0.593}Ga_{0.25}In_{0.031}N$ compounds.

Figure.3.14 displays the results of absorption coefficient $\alpha(\omega)$ for $Al_{0.375}Ga_{0.625}N$, $Al_{0.5}Ga_{0.5}N$ and $Al_{0.625}Ga_{0.375}N$, while Figure.3.15 show the $\alpha(\omega)$ for $Al_{0.343}Ga_{0.625}In_{0.031}N$, $Al_{0.468}Ga_{0.5}In_{0.031}N$ and $Al_{0.593}Ga_{0.25}In_{0.031}N$ compounds. We

observe from the curves of Figure.3.14 and Figure.3.15 that the absorption edge begins from the energy values of4.15, 4.53, 4.85, 3.70, 4.00 and 4.19 eV, corresponding to the energy gaps of $\Gamma v - \Gamma c$, those materials with direct band gap upper to 3.1 eV used for UV application purposes.

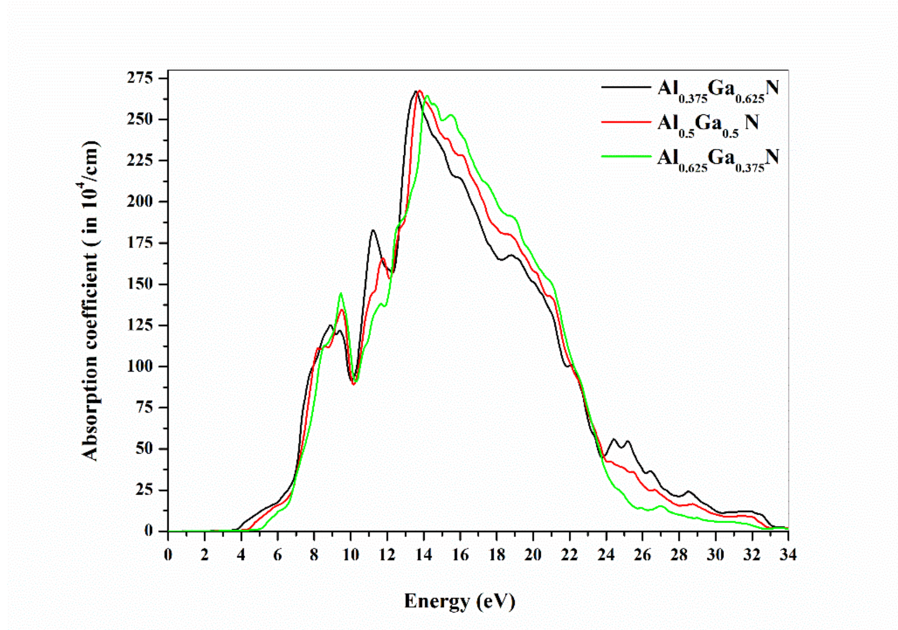

Figure.3.14 Absorption coefficient *α(ω)* for $Al_{0.375}Ga_{0.625}N$, $Al_{0.5}Ga_{0.5}N$ and $Al_{0.625}Ga_{0.375}N$ compounds.

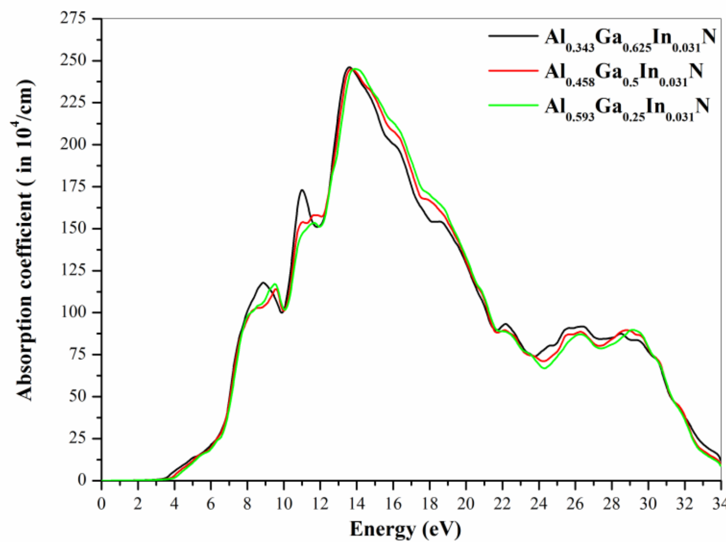

Figure.3.15 Absorption coefficient *α(ω)* for $Al_{0.343}Ga_{0.625}In_{0.031}N$, $Al_{0.468}Ga_{0.5}In_{0.031}N$ and $Al_{0.593}Ga_{0.25}In_{0.031}N$ compounds.

3.4 CONCLUSION

Theoretical study of structural, electronic and optical properties of III-Nitrides alloys based on ‘‘FP-LAPW’’ calculation method, implementing, GGA and mBJ approximations. These compounds, binary (AlN, GaN, InN), ternary ($Al_{0.375}Ga_{0.625}N$, $Al_{0.5}Ga_{0.5}N$, $Al_{0.625}Ga_{0.375}N$) and quaternary ($Al_{0.343}Ga_{0.625}In_{0.031}N$, $Al_{0.468}Ga_{0.5}In_{0.031}N$, $Al_{0.593}Ga_{0.25}In_{0.031}N$) alloys have zinc-blende structure.

The bandgaps nature of these materials is direct $\Gamma v - \Gamma c$, except the AlN have indirect gap. It is inferred that mBJ is an adequate theoretical method for the computation of the band structures of III/V materials. The findings require that mBJ will be a favorable potential for the bandgaps engineering of III/V compounds. In those alloys, the critical points in the optical spectra reveal the passage of electrons from valance band to the unoccupied states in the conduction band.

The zero-frequency edge of $\varepsilon_1(o)$ and $n(o)$ show a reversed link with the bandgaps. From the interpretation of optical graphs, it is provided that those materials are suitable for the fabrications of the ultraviolet optoelectronic devices.

REFERENCES

[1] B. Amin, S. Arif, I. Ahmad, M. Maqbool, R. Ahmad, S. Goumri-Said, and K. Prisbrey, “Cr-doped III-V nitrides: Potential candidates for spintronics,” *J. Electron. Mater.*, vol. 40, no. 6, pp. 1428–1436, 2011.

[2] K. Schwarz and P. Blaha, “Solid state calculations using WIEN2k,” *Comput. Mater. Sci.*, vol. 28, no. 2, pp. 259–273, 2003.

[3] S. Valedbagi, A. Fathalian, and S. Mohammad Elahi, “Electronic and optical properties of AlN nanosheet: An ab initio study,” *Opt. Commun.*, vol. 309, pp. 153–157, 2013.

[4] B. T. Liou and C. W. Liu, “Electronic and structural properties of zincblende $Al_xIn_{1-x}N$,” *Opt. Commun.*, vol. 274, no. 2, pp. 361–365, 2007.

[5] B. Amin, I. Ahmad, M. Maqbool, S. Goumri-Said, and R. Ahmad, “Ab initio study of the bandgap engineering of $Al_{1-x}Ga_xN$ for optoelectronic applications,” *J. Appl. Phys.*, vol. 109, no. 2, p. 023109, 2011.

[6] D. Koller, F. Tran, and P. Blaha, “Merits and limits of the modified Becke-Johnson exchange potential,” *Phys. Rev. B*, vol. 83, no. 19, pp. 195134 – 1 – 10, 2011.

[7] F. Tran and P. Blaha, “Accurate band gaps of semiconductors and insulators with a semilocal exchange-correlation potential,” *Phys. Rev. Lett.*, vol. 102, no. 22, pp. 5–8, 2009.

[8] A. H. Reshak, O. V Parasyuk, A. O. Fedorchuk, H. Kamarudin, S. Auluck, and J. Chysky, “ Optical Spectra and Band Structure of $Ag_xGa_xGe_{1-x}Se2$ (x = 0.333, 0.250, 0.200, 0.167) Single Crystals : Experiment and Theory,” vol. 2, 2013.

[9] L. DJOUDI, A. LACHEBI, B. MERABET, and H. ABID, “first-principle calculation of structural and electronic properties of zinc-blende B_y Al_x Ga_{1-x-y} N matched to AlN substrate,” *Mod. Phys. Lett. B*, vol. 26, no. 24, p. 1250159, 2012.

[10] M. Yousaf, M. a. Saeed, R. Ahmed, M. M. Alsardia, A. R. M. Isa, and a. Shaari, “An Improved Study of Electronic Band Structure and Optical Parameters of X-Phosphides (X=B, Al, Ga, In) by Modified Becke—Johnson Potential,” *Commun. Theor. Phys.*, vol. 58, no. 5, pp. 777–784, 2012.

[11] O. Arbouche, B. Belgoumene, B. Soudini, Y. Azzaz, H. Bendaoud, and K. Amara, "First-principles study on structural properties and phase stability of III-phosphide (BP, GaP, AlP and InP)," *Comput. Mater. Sci.*, vol. 47, no. 3, pp. 685–692, 2010.

[12] T. Seddik, R. Khenata, A. Bouhemadou, A. H. Reshak, F. Semari, and B. Amrani, "Prediction study of the structural, elastic and high pressure properties of Yttrium chalcogenide," *Comput. Mater. Sci.*, vol. 49, no. 2, pp. 372–377, 2010.

[13] L. Vegard, "Die Konstitution der Mischkristalle und die Raumfullung der Atome," *Zeitschrift fur Phys.*, vol. 5, no. 1, pp. 17–26, 1921.

[14] J. Ohta, K. Mitamura, A. Kobayashi, T. Honke, H. Fujioka, and M. Oshima, "Epitaxial growth of InN on nearly lattice-matched (Mn,Zn)Fe 2O4," *Solid State Commun.*, vol. 137, no. 4, pp. 208–211, 2006.

[15] J. A. Camargo-Martinez and R. Baquero, "The modified Becke-Johnson potential analyzed," *Superf. y Vacio*, vol. 26, no. 2, pp. 54–57, 2013.

[16] P. Blaha and G. Madsen, *WIEN2k*, vol. 1. 2012.

[17] F. D. Murnaghan, "Finite Deformations of an Elastic Solid," *American Journal of Mathematics*, vol. 59, no. 2, pp. 235–260, 1937.

[18] M. Marques, L. K. Teles, L. M. R. Scolfaro, J. R. Leite, J. Furthmüller, and F. Bechstedt, "Lattice parameter and energy band gap of cubic AlxGayIn1-x-yN quaternary alloys," *Appl. Phys. Lett.*, vol. 83, no. 5, pp. 890–892, 2003.

[19] P. Rinke, M. Winkelnkemper, A. Qteish, D. Bimberg, J. Neugebauer, and M. Scheffler, "Consistent set of band parameters for the group-III nitrides AlN, GaN, and InN," *Phys. Rev. B - Condens. Matter Mater. Phys.*, vol. 77, no. 7, pp. 1–15, 2008.

[20] Z. Dridi, B. Bouhafs, and P. Ruterana, "First-principles study of cubic AlxGa1-xN alloys," *Comput. Mater. Sci.*, vol. 33, no. 1–3, pp. 136–140, 2005.

[21] M. I. Ziane, Z. Bensaad, T. Ouahrani, and H. Bennacer, "First principles study of structural, electronic and optical properties of indium gallium nitride arsenide lattice matched to gallium arsenide," *Mater. Sci. Semicond. Process.*, vol. 30, pp. 181–196,

[22] N. Nepal, J. Li, M. L. Nakarmi, J. Y. Lin, and H. X. Jiang, "Temperature and

compositional dependence of the energy band gap of AlGaN alloys," *Appl. Phys. Lett.*, vol. 87, no. 24, pp. 1–3, 2005.

[23] I. Vurgaftman and J. R. Meyer, "Band parameters for nitrogen-containing semiconductors," *J. Appl. Phys.*, vol. 94, no. 6, pp. 3675–3696, 2003.

[24] Y. K. Kuo, M. C. Tsai, and S. H. Yen, "Numerical simulation of blue InGaN light-emitting diodes with polarization-matched AlGaInN electron-blocking layer and barrier layer," *Opt. Commun.*, vol. 282, no. 21, pp. 4252–4255, 2009.

[25] R. Ahmed and H. Akbarzadeh, "A first principle study of band structure of III-nitride compounds," vol. 370, pp. 52–60, 2005.

[26] A. Shaukat, Y. Saeed, S. Nazir, N. Ikram, and M. Tanveer, "Ab initio study of structural, electronic and optical properties of Ca1-xSrxS compounds," *Phys. B Condens. Matter*, vol. 404, no. 21, pp. 3964–3972, 2009.

[27] S. Adachi, *Properties of Semiconductor Alloys : Group-IV , III – V and II – VI Semiconductors*.

[28] Z. Jiao, S. Ma, and Y. Guo, "Simulation of optical function for phosphide crystals following the DFT band structure calculations," vol. 970, pp. 79–84, 2011.

[29] A. Assali, M. Bouslama, H. Abid, S. Zerroug, M. Ghaffour, and F. Saidi, "Materials Science in Semiconductor Processing Optoelectronic properties of cubic $B_xIn_yGa_{1-x-y}N$ alloys matched to GaN for designing quantum well Lasers : First- principles study within mBJ exchange potential," *Mater. Sci. Semicond. Process.*, vol. 36, pp. 192–203, 2015.

[30] M. O. Donnell, E. T. Jaynes, and J. G. Miller, " Kramers-Kronig relationship between ultrasonic attenuation and phase velocity" no. May, pp. 696–701, 2014.

[31] B. Merabet, H. Abid, and N. Sekkal, "First principles investigation of optical properties of zinc-blende $Al_xGa_{1-x}As_{1-y}N_y$ materials," vol. 406, pp. 930–935, 2011.

[32] M. Yousaf, F. Inam, R. Khenata, G. Murtaza, A. R. M. Isa, and M. A. Saeed, "Prediction study of structural , electronic and optical properties of XIn 2 S 4 (X = Hg , Zn) thiospinels under pressure effect," *J. Alloys Compd.*, vol. 589, pp. 353–363, 2014.

[33] N. N. Anua, R. Ahmed, A. Shaari, B. U. Haq, F. Science, and U. T. M. Skudai, "DFT

Investigations of the Optical Properties of Gallium Arsenide and Mazmira binti Mohamad," vol. 895, pp. 429–438, 2014.

[34] Z. Feng, H. Hu, Z. Lv, and S. Cui, "First-principles study of electronic and optical properties of BaS , BaSe and BaTe," vol. 8, no. 5, 2010.

CHAPTER 4
THE PROPERTIES OF THE WURTZITE INGAN ALLOYS

4.1 INTRODUCTION

Toward deeper knowledge, slightly extensive experimental and first-principles calculations studies for the ternary alloys $In_xGa_{1-x}N$ with x varying $0 \leq x \leq 1$ have accomplished in the research to perform a significant matching, Luiz Claudio de Carvalho *et* al [1], Seyyed Ali Hashemizadeh *et* al [2], Bo-Ting Liou *et* al [3] and Wen-Wei Lin *et* al [4]. Therefore, our study could provide as a source of perspective for future searches.

The most prominent interest of DFT lies in its ability to execute computations without empirical parameters as inputs, whose relieves up application exceedingly from constraints set by experiments [5], the first-principles calculations based on DFT was performed in the WIEN2K code [6].

This chapter has been arranged in three sections. In Section 2, we concisely illustrate the computational method applied in this study. The important results accomplished for the structural, electronic and optical properties of $In_xGa_{1-x}N$ ternary alloys are exhibited and discussed in Section 3. Subsequently, the conclusions in Section 4.

4.2 COMPUTATIONAL DETAIL

The precise and important theoretical solution of the structural, electronic, optical, and magnetic properties of metals and semiconductors is the Kohn-Sham formation [7-8-9].

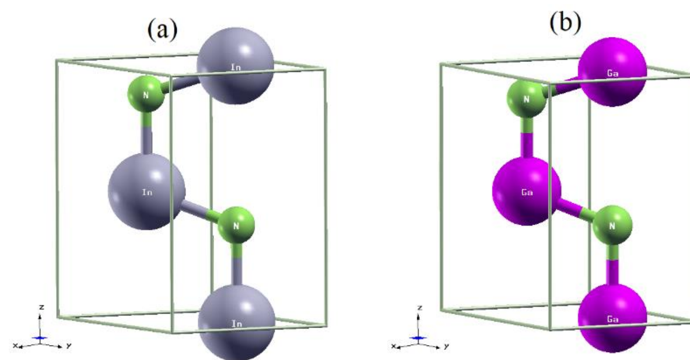

Figure.4.1 Illustration of a 1×1×1 conventional hexagonal cell- wurtzite: (a) InN and (b) GaN.

The nitrides compounds crystalize in zinc-blende (space group $F43m$) and wurtzite structure (space group $P63mc$). The current calculations in this study of the physical properties of the wurtzite ternary alloy $A_xB_{1-x}N$ ($In_xGa_{1-x}N$), so that x signifies In composition, were performed by the FP-LAPW method based on the DFT executed in the WIEN2k package [10]. To model $A_xB_{1-x}N$ wurtzite alloy, we used a 16-atom $A_nB_{8-n}N_8$ supercell, (2 × 2 × 2) that is

twice the size of a primitive wurtzite unit cell in base plane direction [3]. The model of crystal structures of ternary $In_xGa_{1-x}N$ alloys is shown in Figure.4. 2.

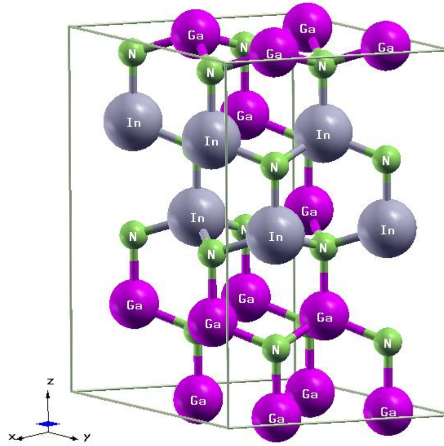

Figure.4.2 Illustration of a 2×2×2 wurtzite $In_{0,375}Ga_{0,625}N$ supercell.

The exchange and correlation effects were handled applying three different approximations: the Wu and Cohen generalized gradient approximation (GGA-WC) functional [11-12], the standard local density approach (LDA), and the modified Becke-Johnson exchange potential [F. Tran and P. Blaha] (TB-mBJ) [11-13-14] is performed to procure a larger band gap value that is generally underestimated by LDA and GGA [11]. For the total and partial densities of states (DOS) we considered the orbitals of In ($4d^{10}5s^25p^1$), Ga ($3d^{10}4s^24p^1$) and N ($2s^22p^3$) as valence electrons.

An entirely relativistic calculation moreover scalar relativistic approximation for core and valence state, respectively, without spin-orbit interaction, were employed. In the interstitial region, the plane wave cut-off value of $RMT * Kmax = 7$ was used [15], where RMT is the minimum radius of the muffin-tin spheres are set to 2.04, 1.84, 1.70 atomic units (a.u) for In, Ga and N respectively, and $Kmax$ provides the magnitude of the largest K vector in the plane wave basis [16]. The maximum l quantum number of the wave function expansion inside the atomic sphere was defined to $lmax = 10$ [10], for the Fourier expansion the charge density was extended to $Gmax = 12(a.u)^{-1}$. The Brillion Zone (BZ) integration has been formed applying Monkhorst-Pack Special K-points approach [17].

4.3 Results and discussion

4.3.1 Structural properties

First, we performed the structural properties of the binary compounds InN and GaN in the both structures wurtzite (wz) and zinc-blende (zb). The InN and GaN are reported by (1×1×1) conventional hexagonal cell (wurtzite) and face centred cubic (zinc-blende).

The computed total energies within GGA as a function of the volume were employed for the perception of theoretical lattice constant and bulk modulus. The equilibrium energy E_0, the Bulk modulus B_0, its first derivative B_0', and the balance volume at zero pressure V_0, by fitting the calculated total energy to the Murnaghan's equation of state (EOS) [18], which is allowed with WIEN2k package.

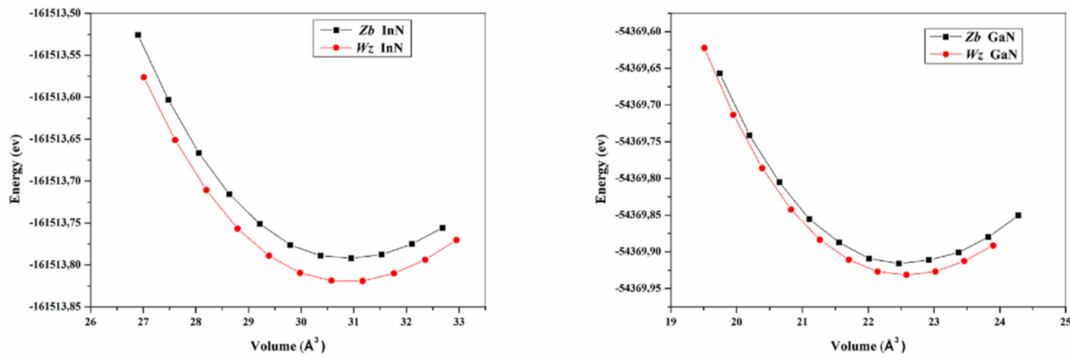

Figure.4.3 Total energies as a function of volume for the InN and GaN for zb and wz phases.

From Figure.4.3 we noticed that the wz phase was found to be more stable than the zinc-blende phase for the InN and GaN compounds. The calculated lattice constants and bulk modulus are arranged in Table.4.1.

Table.4.1

The lattice constant a and c, bulk modulus B and its first derivative B' of InN and GaN, compared to other experimental or theoretical data, the lattice mismatch $\Delta(a_o)$ and $\Delta(c_o)$ are indicated in the table.

Material	a(Å)			c(Å)			$\Delta(a_o)$	$\Delta(c_o)$	B(GPA)		B'	
	our	Other	exp	our	other	exp			Our	Other	our	Other
InN	3.57	3.59[a]	3.53[a]	5.80	5.78[a]	5.69[a]	0.04	0.11	123.41	--	4.18	--
		3.54[d]	3.51[c]		5.70[d]	5.66[c]	0.06	0.14				
		3.54[f]	3.55[e]		5.71[f]	5.74[e]	0.02	0.06				
GaN	3.21	3.23[a]	3.19[a]	5.24	5.26[a]	5.18[a]	0.02	0.06	176.80	--	4.20	--
		3.18[b]	3.15[c]		5.18[b]	5.14[c]	0.06	0.10				
		3.19[d]	3.18[e]		5.18[d]	5.18[e]	0.03	0.06				
		3.18[f]			5.18[f]							

[a]Ref[19], [b]Ref[20], [c]Ref[21], [d]Ref[22], [e]Ref[23], [f]Ref[24]

The obtained lattice constant parameters a and c for the wurtzite InN and GaN were somewhat bigger than the experimental lattice constant parameters, the shift in lattice parameter set as $\Delta(a_o)$ and $\Delta(c_o)$. For further details, no experimental data were possible for the Bulk modulus B_0 and its first derivative B_0'.

The element configuration of ternary alloy $In_xGa_{1-x}N$ acts a notable part in both physical properties and the epitaxial growth process. To study the fundamental structural properties of the ternary alloys $In_xGa_{1-x}N$ matched on GaN substrate for composition of $0 \leq x \leq 1$, we have considered all studied of the ternary alloys in wz phase which is the stable compared with zinc-blende whereas the ternary alloys $In_xGa_{1-x}N$ with 16 atoms with 25% intervals of x.

Reviewing the Vegard's law validity for the wurtzite ternary alloy $In_xGa_{1-x}N$, the lattice constant is commonly denoted as a linear function depend on x concentration of the compounds. The Vegard's law [25] is applicable for the both a and c lattice parameters as below:

$$a_{In_xGa_{1-x}N} = xa_{InN} + (1-x)a_{GaN} \quad (4.1),$$

$$c_{In_xGa_{1-x}N} = xc_{InN} + (1-x)c_{GaN} \quad (4.2).$$

The obtained lattice constants of $In_xGa_{1-x}N$ are summarized in Table.4.2.

Table.4.2

The lattice constant a and c calculated by The Vegard's law of $In_xGa_{1-x}N$, compared to other experimental work results.

material	a(Å)		c(Å)	
	our	exp	our	exp
$In_{0,125}Ga_{0,875}N$	3.24	3.20a	5.31	5.21[a]
$In_{0,375}Ga_{0,625}N$	3.33	3.30a	5.45	5.35[a]
$In_{0,625}Ga_{0,375}N$	3.43	3.38a	5.59	5.49[a]
$In_{0,875}Ga_{0,125}N$	3.52	3.47a	5.73	5.64[a]

[a]Ref [3]

From the Table.4.2, its clearly observed that the lattice constant a and c are in inversely proportional relation with the Indium incorporation.

4.3.2 ELECTRONIC PROPERTIES

The energy band gap of a semiconductor is an essential key which is extremely useful for their efficient employment in optoelectronic and different photonic devices. Its small variation can completely modify the utilization in the optoelectronic devices. Therefore, the knowledge of the character of the band gaps of the current materials and their precise values whether by experiments or calculations are not only significant for their technological applications as well as their band gap tailoring [26].

It is entirely comprehended that the most accurate GGA and LDA undervalue the band gap of semiconductors, the reason is the regardless of the quasiparticle excitations in DFT. To defeat this obstacle, the mBJ approach was employed to produce a band gap approaching the experiment value.

The bandgap energy formula of the $In_xGa_{1-x}N$ is depicted as below:

$$E_g(x) = x \cdot E_g(InN) + (1-x) \cdot E_g(GaN) - b \cdot x \cdot (1-x) \quad (4.3),$$

where $E_g(x)$, $E_g(InN)$, $E_g(GaN)$ are the bandgap energy for the respective $In_xGa_{1-x}N$, InN and GaN, and b is the bandgap bowing parameter [27], the Vegard's law is convenient for the lattice constants of relaxed $InGaN$. Recent studies propose that the bowing parameter values depend to the indium incorporation, so that for $0 \leq x \leq 0.5$ the bowing is 1.4 eV, and for $0 \leq x \leq 1$ the bowing be 1.15eV or 2.5eV [3].

Accordingly, the calculated results completed of energy at the point Γ of high-symmetry on the Brillouin zone for the studied binary and ternary compounds using the WC-GGA, LDA, TB-mBJ are summarized in Table.4.3, together with previous experimental results.

Table.4.3

The energy band gap Eg of GaN, InN and $In_xGa_{1-x}N$ calculated with WC-GGA, LDA, TB-mBJ and Vegard's law compared to other experimental or theoretical data.

Material	Eg (eV)					
	WC-GGA	LDA	TB-mBJ	Vegard's law Calculations bowing 1.11	bowing 2.5	Exp
InN	0.00	0.00	0.77	--	--	0.70[a] – 0.77[b]
$In_{0,125}Ga_{0,875}N$	1.24	1.31	2.58	2.61	2.46	2.88 [b] - 3.10 [c]
$In_{0,375}Ga_{0,625}N$	0.49	0.55	1.68	1.91	1.58	1.95 [b]- 2.62 [c]
$In_{0,625}Ga_{0,375}N$	0.03	0.08	1.17	1.35	1.02	1.38 [b]

$In_{0,875}Ga_{0,125}N$	0.00	0.00	0.82	0.93	0.77	0.85 [b]
GaN	1.67	1.75	3.01	--	--	3.50[a] -3.42[b]-3.42[c]

[a] Ref [1]. [b] Ref [3]. [c] Ref [4].

It is obviously noticed that the calculated band gap values (Table.4.3) with TB-mBJ display a clear improvement over the previously calculated values using Vegard's law.

Figure.4.4 present the band structure of the considered ternary alloy $In_xGa_{1-x}N$, the high-symmetry lines through the first irreducible Brillouin zone estimated within mBJ approach.

The valance band maximum (VBM) and the conduction band minimum (CBM) appear at the Γ point showing that the studying materials have a direct band gap. Those results correspond properly through the precedent experimental and theoretical searches.

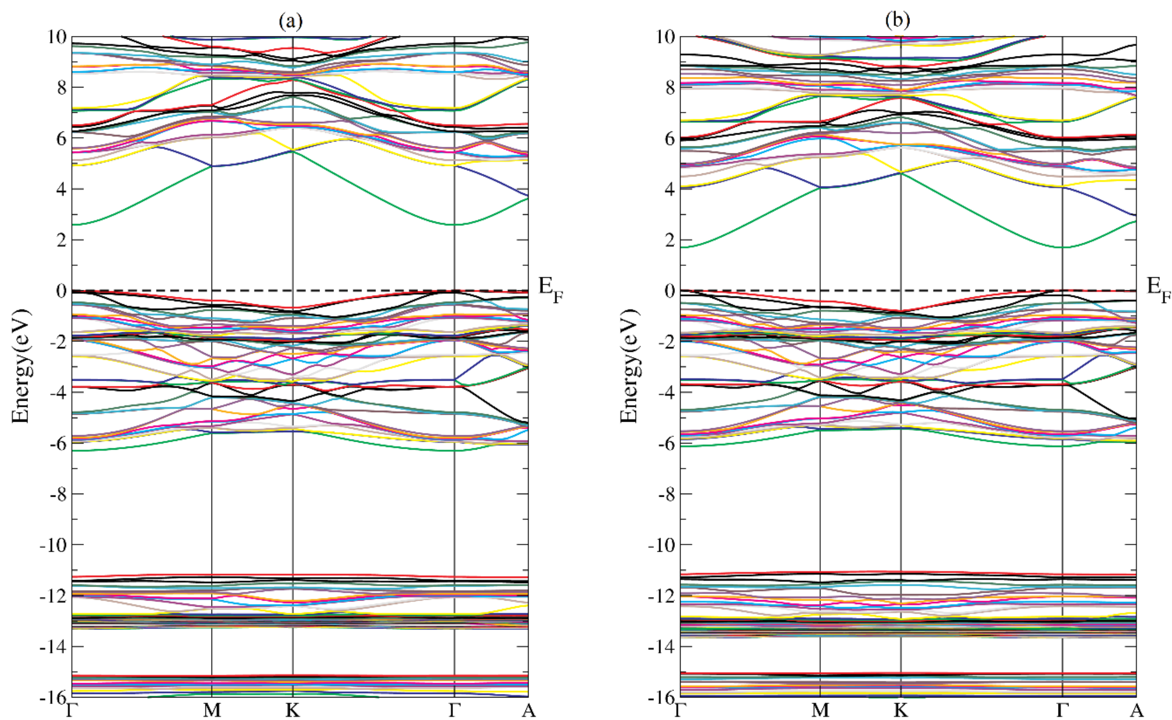

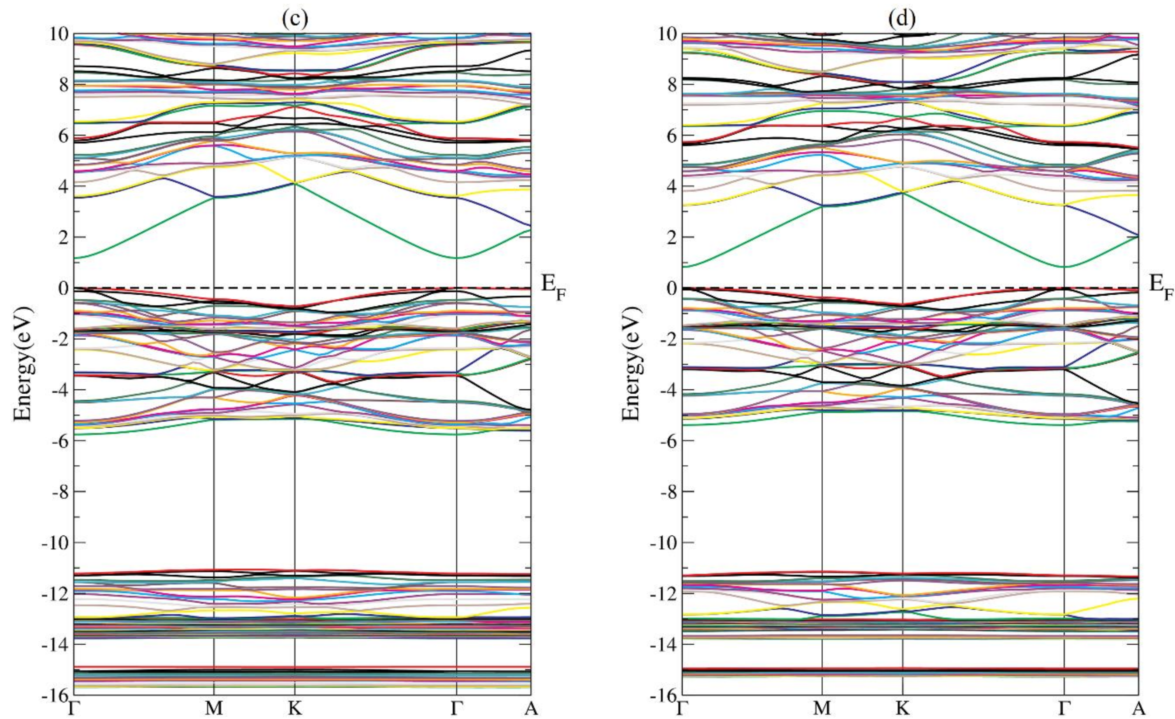

Figure.4.4 Band structures within TB-mBJ for (a)$In_{0,125}Ga_{0,875}\,N$, (b) $In_{0,375}Ga_{0,625}\,N$,(c) $In_{0,625}Ga_{0,375}\,N$ and (d) $In_{0,875}Ga_{0,125}\,N$.

The data of energy band gap using the WC-GGA, LDA and TB-mBJ approximations depicted in Table.4.3 are plotted in Figure.4.5.

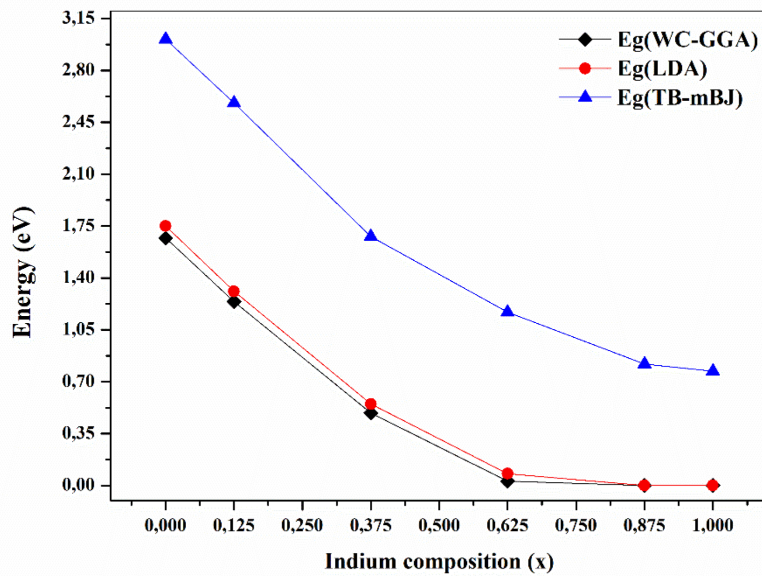

Figure.4.5 Band gap energy as a function of Indium concentration.

Figure.4.5 displays that at small Indium composition, a notable bowing can be achieved however at huge indium composition, the bowing could be negligible. Therefore, the Band gap energy can be characterized as a function of the Indium composition, the Eg is fitted and expressed by the following equations:

$$Eg^{WC-GGA}(x) = 1.68 - 4.13x + 2.46x^2 \quad (4.4),$$

$$Eg^{LDA}(x) = 1.76 - 4.15x + 2.39x^2 \quad (4.5),$$

$$Eg^{TB-mBJ}(x) = 3.03 - 4.25x + 1.98x^2 \quad (4.6),$$

these equations are related to the formula (4.3), where the bowing b = 2.46, 2.39 and 1.98 corresponding the respective approximations WC-GGA, LDA and Tb-mBJ.

The information of the electron density of states (DOS) is wanted to comprehend and simplify, the calculated band structure to know the contributing atomic states, the total and the partial DOS of the studied ternary $In_{0,125}Ga_{0,875}N$, $In_{0,375}Ga_{0,625}N$, $In_{0,625}Ga_{0,375}N$ and $In_{0,875}Ga_{0,125}N$ respectively are plotted in Figure.4.6, which are estimated using the TB-mBJ scheme. We have considered the inner-shell electrons in the valence electrons of In ($4d^{10}5s^25p^1$), Ga ($3d^{10}4s^24p^1$), and N ($2s^22p^3$) shells [28].

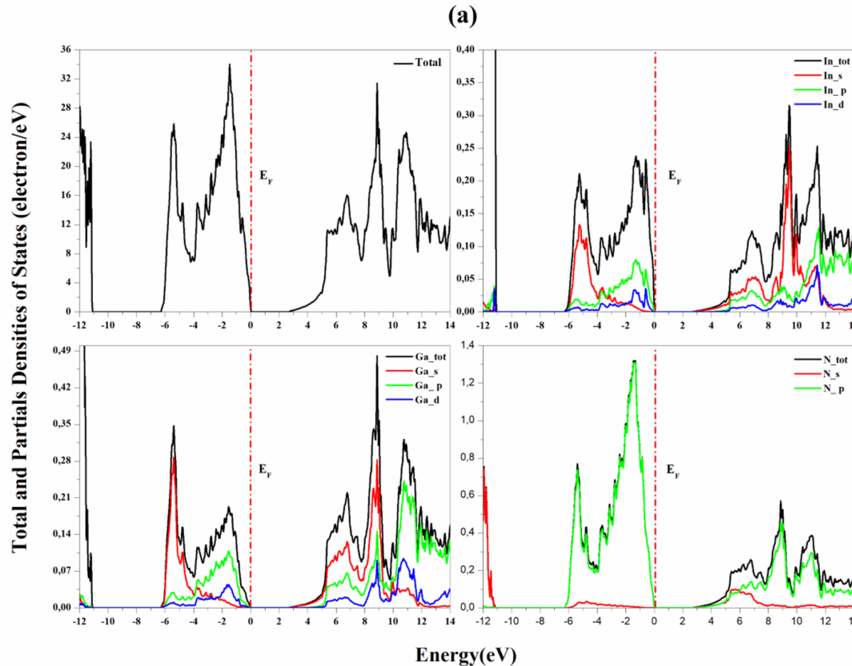

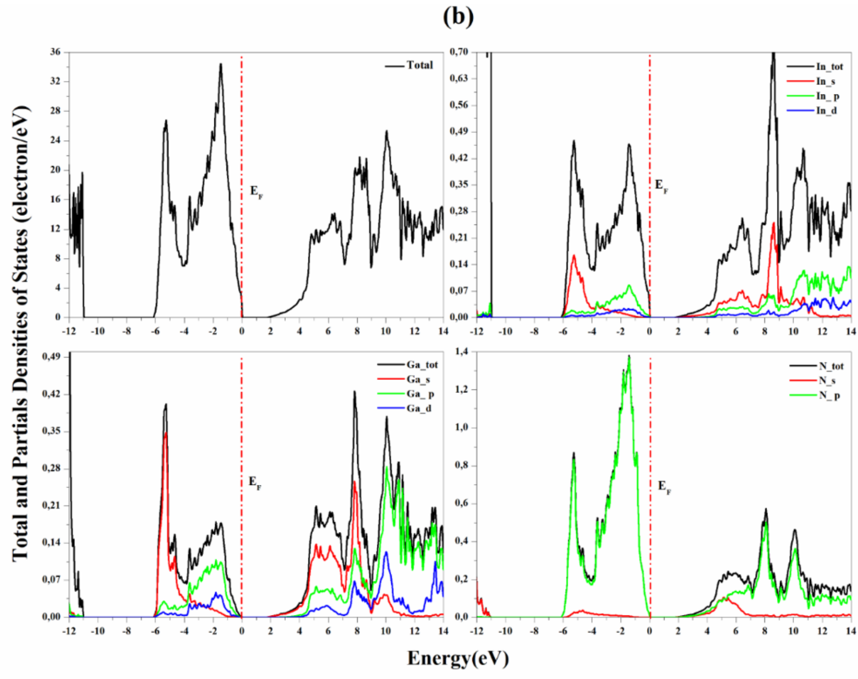
(b)
Total
In_tot
In_s
In_p
In_d
Ga_tot
Ga_s
Ga_p
Ga_d
N_tot
N_s
N_p
E_F
Total and Partials Densities of States (electron/eV)
Energy(eV)

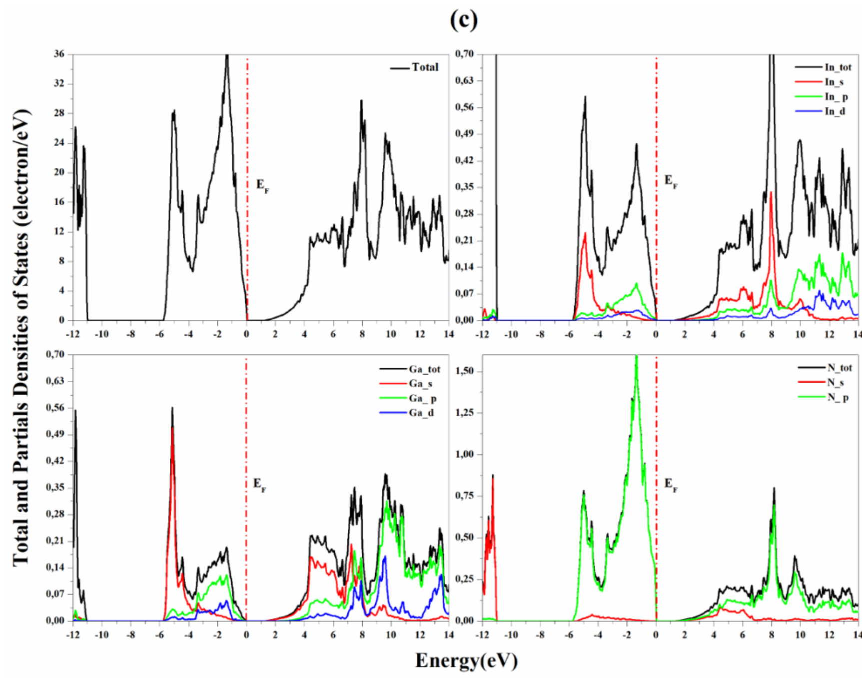
(c)
Total
In_tot
In_s
In_p
In_d
Ga_tot
Ga_s
Ga_p
Ga_d
N_tot
N_s
N_p
E_F
Total and Partials Densities of States (electron/eV)
Energy(eV)

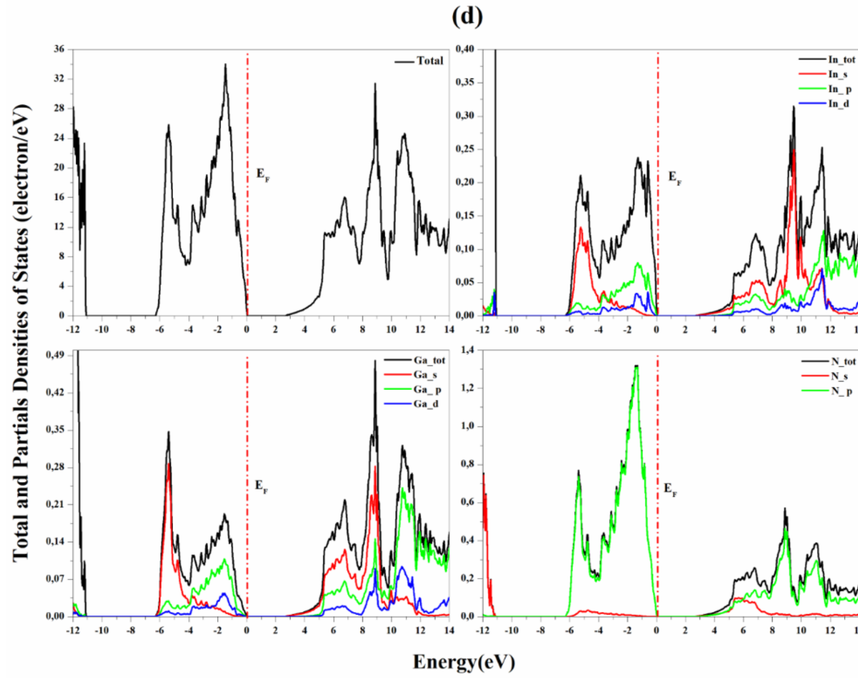

Figure.4.6 Total and partial densities of states for (a) $In_{0,125}Ga_{0,875}\,N$, (b) $In_{0,375}Ga_{0,625}\,N$, (c) $In_{0,625}Ga_{0,375}\,N$ and (d) $In_{0,875}Ga_{0,125}\,N$ compounds.

It is obviously shown from Figure.4.6, the state's lesser E_F the valence band be divided by two region the narrow range between (-13.08 -11.06) eV, mainly originates from the hybridization of In s/p, Ga s/p and N/s states. The wider region from -6.08 eV to fermi level contain two peaks, the first between (-6.08, -4.10) eV is mainly occupied by N/p, G/s and In/s states while the second from -4.10 eV approaching to fermi level is densely dominated by N/p, Ga P/d, In p/d states.

The studied ternary compounds note a definite energy gap among the valance and the conduction energy bands of 2.58, 1.68, 1.17 and 0.82 eV for the $In_{0,125}Ga_{0,875}\,N$, $In_{0,375}Ga_{0,625}\,N$, $In_{0,625}Ga_{0,375}\,N$ and $In_{0,875}Ga_{0,125}\,N$ respectively, the alloys system preserving its semiconductor character. Hence, the dominant conduction electron states possess a composition from several N/p, Ga s/p/d and In s/p.

4.3.3 Optical properties

The optical properties are straightly correlated to the electronic band gap of a semiconductor, characterizing the interaction of electromagnetic radiations with a material. The dielectric function $\varepsilon(\omega)$ acts an essential part in exploring the optical properties of a compound.

To provide an excellent optical properties of the wz semiconductors, a 480 k points was achieved into the irreducible part of Brillouin zone *(BZ)* integration using the TB-mBJ exchange potential for the $In_{0,125}Ga_{0,875}N$, $In_{0,375}Ga_{0,625}N$, $In_{0,625}Ga_{0,375}N$ and $In_{0,875}Ga_{0,125}N$.

Table.4.4

Collected the peak positions of $\varepsilon_2(\omega)$, static dielectric constant $\varepsilon_1(0)$, refractive index $n(0)$ and Static reflectivity $R(0)$ $In_{0,125}Ga_{0,875}N$, $In_{0,375}Ga_{0,625}N$, $In_{0,625}Ga_{0,375}N$ and $In_{0,875}Ga_{0,125}N$.

Materials	Critical points					Static dielectric constant	Static refractive index	Static reflectivity
	A	B	C	D	E	$\varepsilon_1(0)$	$n(0)$	$R(0)$
$In_{0,125}Ga_{0,875}N$	2.58	7.55	8.93	10.22	12.05	4.49	2.11	0.128
$In_{0,375}Ga_{0,625}N$	1.68	7.07	8.64	9.60	11.65	4.93	2.22	0.144
$In_{0,625}Ga_{0,375}N$	1.17	6.06	8.24	9.19	11.11	5.33	2.30	0.156
$In_{0,875}Ga_{0,125}N$	0.82	5.56	7.89	8.71	10.75	5.88	2.42	0.172

The dielectric function can be written as $\varepsilon(\omega) = \varepsilon_1(\omega) + i\varepsilon_2(\omega)$, illustrates the material response to the photon spectrum, where the imaginary part of the dielectric function $\varepsilon_2(\omega)$ signifies the optical absorption in the crystal, those able to acquire from the momentum matrix elements through the occupied and unoccupied eigenstates. It signifies the diversity of inter-band transitions in a semiconductor and the real part $\varepsilon_1(\omega)$ of the dielectric function is related to the imaginary part $\varepsilon_2(\omega)$ by employing the Kramers Kronig (KK) relations [29]:

$$\varepsilon_1(\omega) = 1 + \frac{2}{\pi} P \int_0^\infty \frac{\acute{\omega}\varepsilon_2(\acute{\omega})}{\acute{\omega}^2 - \omega^2} d\acute{\omega} \quad (4.7).$$

Different optical properties can be determined from the dielectric function, selected the refractive index $n(\omega)$, the extinction coefficient $k(\omega)$, the reflectivity $R(\omega)$, and the absorption coefficient $\alpha(\omega)$, within the following relations: [30]

$$n(\omega) = \sqrt{\frac{|\varepsilon(\omega)| + \varepsilon_1(\omega)}{2}} \quad (4.8),$$

$$K(\omega) = \sqrt{\frac{|\varepsilon(\omega)| - \varepsilon_1(\omega)}{2}} \quad (4.9),$$

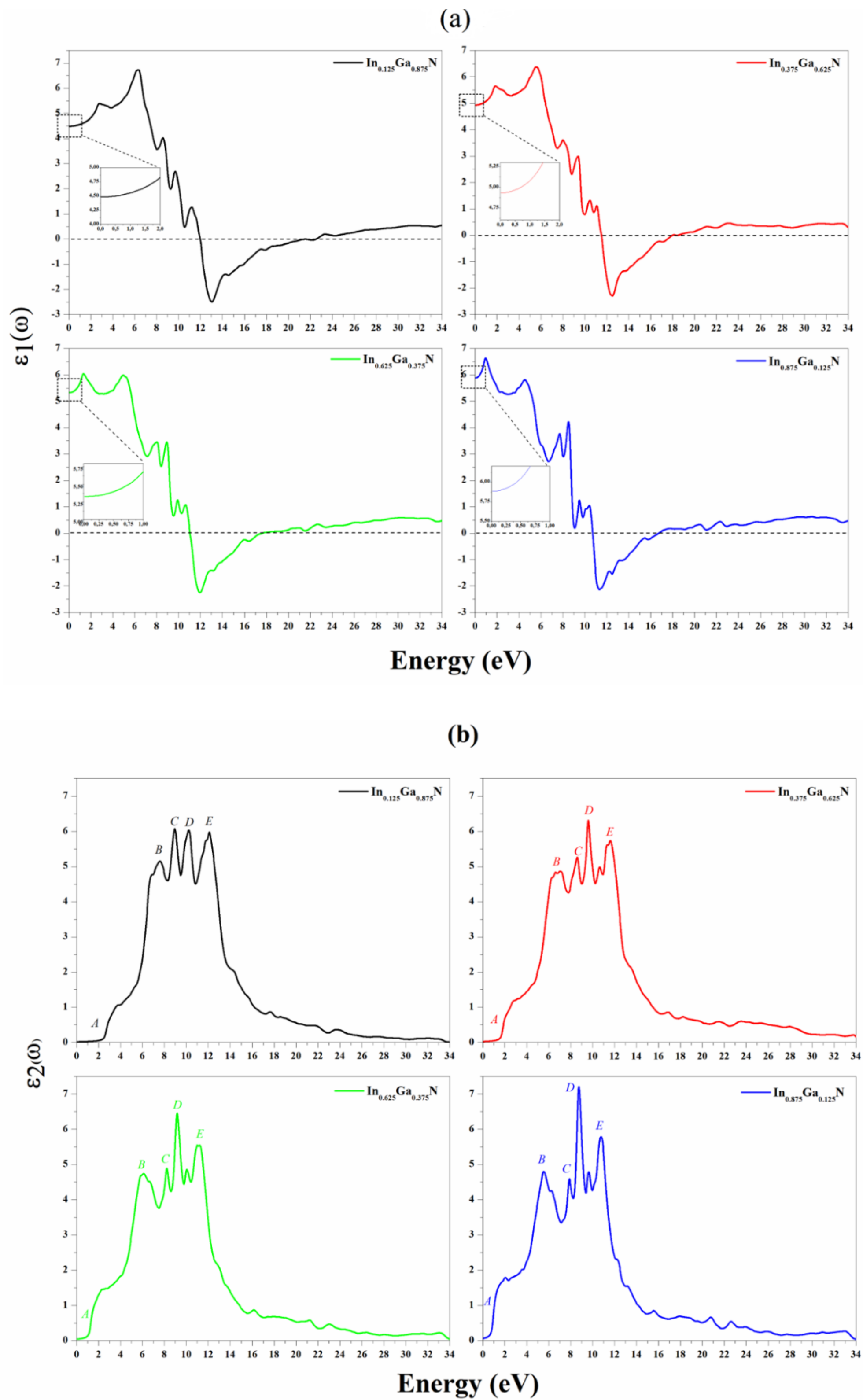

Figure.4.7 Real part $\varepsilon_1(\omega)$ (a) and imaginary part $\varepsilon_2(\omega)$ (b) for $In_{0,125}Ga_{0,875}N$, $In_{0,375}Ga_{0,625}N$, $In_{0,625}Ga_{0,375}N$ and $In_{0,875}Ga_{0,125}N$.

$$R(\omega) = \frac{(n(\omega)-1)^2+k(\omega)^2}{(n(\omega)+1)^2+k(\omega)^2} \quad (4.10),$$

$$\alpha(\omega) = \frac{4\pi}{\lambda} k(\omega) \quad (4.11),$$

where, λ is the wavelength of light in the vacuum.

From Figure.4.7 (b), the calculated $\varepsilon_2(\omega)$ spectra reveal that the first crucial point A, further set as optical's absorption edge occurs at 2.58, 1.68, 1.17 and 0.82 (eV) which represent the direct optical transitions for the respective compounds $In_{0,125}Ga_{0,875}N$, $In_{0,375}Ga_{0,625}N$, $In_{0,625}Ga_{0,375}N$ and $In_{0,875}Ga_{0,125}N$. The electronic optical transitions (represented by peaks B, C, D and E given in Table.4.4 among the valence band and conduction band at $\Gamma_{15v} - \Gamma_{1c}$ symmetry point, originate the absorption region.

Figure.4.7 (a) show the real part of dielectric function $\varepsilon_1(\omega)$, afford the static dielectric constant $\varepsilon_1(0)$ presented in Table.4.3. The inversely proportional relation between the $\varepsilon_1(0)$ and E_g can be defined by the Penn model [31],

$$\varepsilon \approx 1 + (\hbar\omega_p/E_g)^2 \quad (4.12),$$

$\varepsilon_1(\omega)$ rises within a small energy margin, then decreases for values less than one, the lower values of $\varepsilon_1(\omega)$ occurs at 13.02, 12.53, 11.93 and 11.36 eV for the $In_{0,125}Ga_{0,875}N$, $In_{0,375}Ga_{0,625}N$, $In_{0,625}Ga_{0,375}N$ and $In_{0,875}Ga_{0,125}N$, respectively. These values correspond to the higher values of the reflectivity shown in Figure.4.7 (a). Furthermore, when $\varepsilon_1(\omega)$ attains a stability when getting energy more than (>22, 18, 17and 16) eV for the respective ternary $In_{0,125}Ga_{0,875}N$, $In_{0,375}Ga_{0,625}N$, $In_{0,625}Ga_{0,375}N$ and $In_{0,875}Ga_{0,125}N$, designating that the incident photons cross the material without any notable interaction.

As provides in Figure.4.8(a), the reflectivity reached the maximum in the photon energy range (12.53, 16.55), (11.84, 15.40), (11.51, 15.06) and (10.88, 14.56) eV for the compounds $In_{0,125}Ga_{0,875}N$, $In_{0,375}Ga_{0,625}N$, $In_{0,625}Ga_{0,375}N$ and $In_{0,875}Ga_{0,125}N$,respectively. These Prominent reflectance is explained to the resonance plasmon rising in the Ultraviolet range. Furthermore, the In integration decrease proportionally the maximum value of the reflectivity as below 0.48, 0.46, 0.45 and 0.44 (a.u) for the respective In concentration (x = 0.125, 0.375, 0.625 and 0.875).

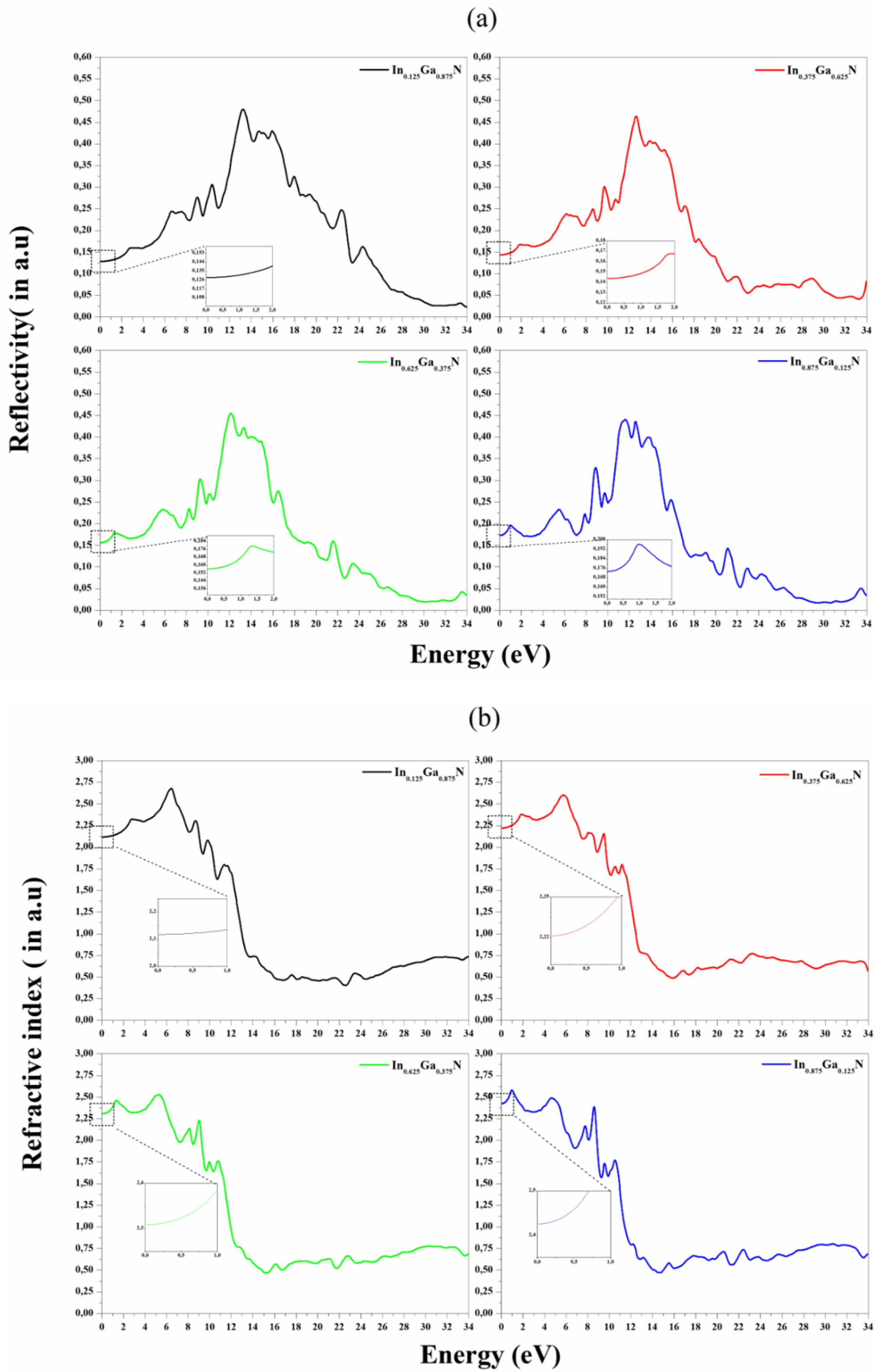

Figure.4.8 reflectivity $R(\omega)$ (a) and (b) refractive index $n(\omega)$ for $In_{0,125}Ga_{0,875}\,N$, $In_{0,375}Ga_{0,625}\,N$, $In_{0,625}Ga_{0,375}\,N$ and $In_{0,875}Ga_{0,125}\,N$.

The refractive index follows the pattern of $\varepsilon_1(\omega)$, It is seen from the Figure.4.8(b) that $n(\omega)$ spectra increase and reach a peak value of (2.67 at 6.48 eV , 2.60 at 5.72 eV, 2.52 at 5.23 eV and 2.57at 0.93 eV for the respective $In_{0,125}Ga_{0,875}N$, $In_{0,375}Ga_{0,625}N$, $In_{0,625}Ga_{0,375}N$ and $In_{0,875}Ga_{0,125}N$ compounds. Beyond the maximum, the spectra decrease inferior to 1. As the bandgap is decreased when we increase the In amount, while $n(0)$ alter vice versa with the band gap of the compounds as mentioned in the Table.4.3. The Refractive index inferior than unity ($vg = c/n$) exhibits that the group velocity of the incident radiation is bigger than the lightspeed c [32-33]. It signifies that the group velocity shift to negative domain and the material turn into superluminal for high energy photons.

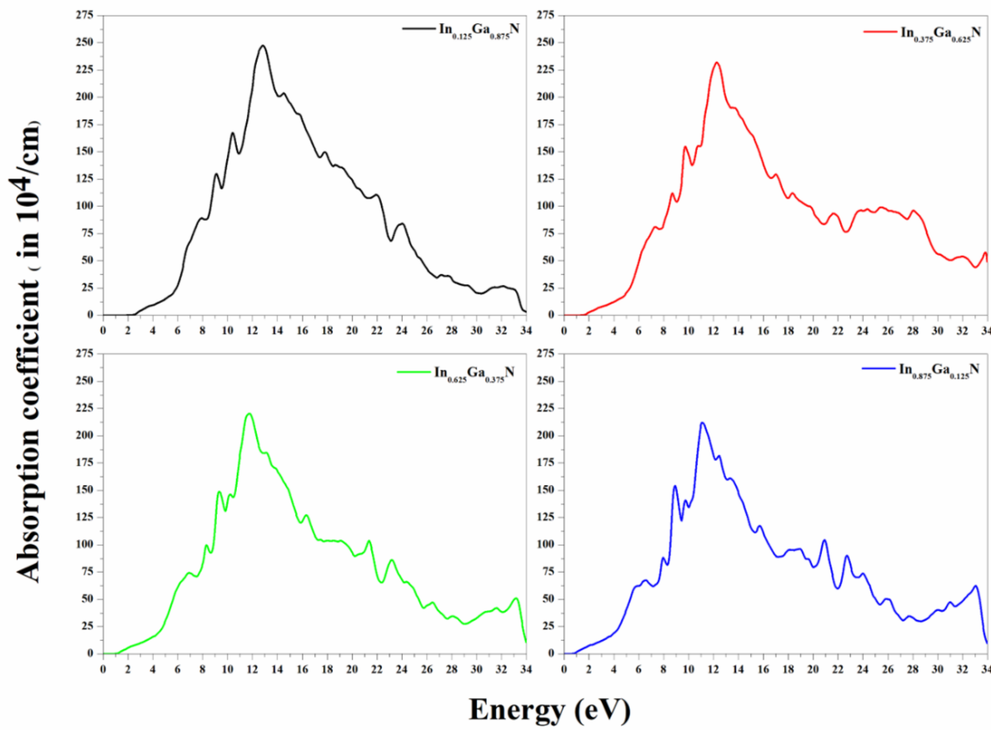

Figure.4.9 Absorption coefficient *α(ω)*for $In_{0,125}Ga_{0,875}N$, $In_{0,375}Ga_{0,625}N$, $In_{0,625}Ga_{0,375}N$ and $In_{0,875}Ga_{0,125}N$.

It is clearly from the absorption $\alpha(\omega)$ spectra plotted in Figure.4.9, that the absorption edge occurs at the energy values 2.58, 1.68, 1.17 and 0.82 eV for the compounds $In_{0,125}Ga_{0,875}N$, $In_{0,375}Ga_{0,625}N$, $In_{0,625}Ga_{0,375}N$ and $In_{0,875}Ga_{0,125}N$, respectively. These previous values are identical to the energy gaps of $\Gamma v - \Gamma c$. The absorption coefficient is the most important characterizing the solar cells, the maximum $\alpha(\omega)$ is 248.41, 231.96, 219.30 and 211.55 for In concentration of ($x =$0.125, 0.375, 0.625 and 0.875), therefore confirm Laref et *al.* [34]

study that for In poor region (x less or equal 25%) the $In_xGa_{1-x}N$ may allow the possibility of appropriate bandgap engineering for solar cell utilization.

4.4 CONCLUSION

Theoretical study of structural, electronic and optical properties of III-Nitrides alloys based on ''FP-LAPW'' calculation method, implementing LDA, GGA and mBJ approximations. These ternary compounds $In_{0,125}Ga_{0,875}N$, $In_{0,375}Ga_{0,625}N$, $In_{0,625}Ga_{0,375}N$ and $In_{0,875}Ga_{0,125}N$ have wurtzite structure.

The bandgaps nature of these materials is direct $\Gamma v - \Gamma c$. It is inferred that mBJ is an adequate theoretical method for the computation of the band structures of III/V materials. The findings require that mBJ will be a favorable potential for the bandgaps engineering of III/V compounds. In those alloys, the critical points in the optical spectra reveal the passage of electrons from valance band to the unoccupied states in the conduction band.

The zero-frequency edge of $\varepsilon_1(o)$ and $n(o)$ show a reversed link with the bandgaps. From the interpretation of optical graphs, it is provided that those materials are implemented for optoelectronics components in ultraviolet energy ranges and for solar cells application.

REFERENCES

[1] L. C. de Carvalho, A. Schleife, J. Furthmüller, and F. Bechstedt, "Ab initio calculation of optical properties with excitonic effects in wurtzite $In_xGa_{1-x}N$ and $In_xAl_{1-x}N$ alloys," *Phys. Rev. B*, vol. 87, no. 19, pp. 195211-1–12, 2013.

[2] S. Ali Hashemizadeh and V. Mohammadi Siavashi, "First-Principles Investigation of Density of States and Electron Density in Wurtzite $In_{0.5}Ga_{0.5}N$ Alloys with GGA-PBEsol Method," *J Nanostruct*, vol. 6, no. 4, pp. 273–277, 2016.

[3] B.-T. Liou, S.-H. Yen, and Y.-K. Kuo, "Vegard's law deviation in band gaps and bowing parameters of the wurtzite III-nitride ternary alloys," *Semicond. Lasers Appl. II*, vol. 5628, pp. 296–305, 2005.

[4] W.-W. Lin and Y.-K. Kuo, "Band structures and bandgap bowing parameters of wurtzite and zincblende III-nitrides," *Semicond. Lasers Appl.*, vol. 4913, p. 236, 2002.

[5] N. N. Anua, R. Ahmed, A. Shaari, B. U. Haq, F. Science, and U. T. M. Skudai, "DFT Investigations of the Optical Properties of Gallium Arsenide," vol. 895, pp. 429–438, 2014.

[6] K. Schwarz and P. Blaha, "Solid state calculations using WIEN2k," *Comput. Mater. Sci.*, vol. 28, no. 2, pp. 259–273, 2003.

[7] B. Amin and I. Ahmad, "Theoretical investigation of half metallicity in Fe/Co/Ni doped ZnSe material systems," *J. Appl. Phys.*, vol. 106, no. 9, pp. 93710-1–8, 2009.

[8] P. HOHENBERG and W. KOHN, "Inhomogeneous electron Gas," *Phys. Rev. B*, vol. 136, no. 3B, pp. 864–871, 1964.

[9] W. Kohn and L. J. Sham, "Self-consistent equations including exchange and correlation effects," *Phys. Rev.*, vol. 140, no. 4A, pp. A1131–A1138, 1965.

[10] M. Dadsetani, B. Kianisadr, and H. Nejatipour, "First Principles Investigation of the Optical Properties of BN_xP_{1-x} $(0 \leq x \leq 1)$ Boron Ternary Alloys," *J. Electron. Mater.*, vol. 44, no. 8, pp. 2699–2711, 2015.

[11] B. T. Liou and C. W. Liu, "Electronic and structural properties of zincblende $Al_xIn_{1-x}N$," *Opt. Commun.*, vol. 274, no. 2, pp. 361–365, 2007.

[12] B. Amin, I. Ahmad, M. Maqbool, S. Goumri-Said, and R. Ahmad, "Ab initio study of

the bandgap engineering of $Al_{1-x}Ga_xN$ for optoelectronic applications," *J. Appl. Phys.*, vol. 109, no. 2, p. 23109, 2011.

[13] B. Amina, A. Lachebi, A. Shuhaimi, S. A. Rahman, and H. Abid, "First-principles calculation of structural, optoelectronic properties of the cubic $Al_xGa_yIn_{1-x-y}$ N quaternary alloys matching on AlN substrate, within modified Becke-Johnson (mBJ) exchange potential," *Optik (Stuttg).*, vol. 127, no. 23, pp. 11577–11587, 2016.

[14] D. Koller, F. Tran, and P. Blaha, "Merits and limits of the modified Becke-Johnson exchange potential," *Phys. Rev. B*, vol. 83, no. 19, pp. 195134-1–10, 2011.

[15] M. Aslan, A. H. Reshak, B. G. Yalcin, S. Bagci, and M. Ustundag, "Structural and electronic properties of InN_xP_{1-x} alloy in full range ($0 \leq x \leq 1$)," *Philos. Mag.*, vol. 6435, no. March, pp. 1–15, 2016.

[16] T. Ouahrani, A. H. Reshak, R. Khenata, B. Amrani, M. Mebrouki, A. Otero-de-la-Roza, and V. Luana, "Ab-initio study of the structural, linear and nonlinear optical properties of CdAl2Se4 defect-chalcopyrite," *J. Solid State Chem.*, vol. 183, no. 1, pp. 46–51, 2010.

[17] B. U. Haq, R. Ahmed, M. Mohamad, A. Shaari, J. Y. Rhee, S. AlFaify, M. B. Kanoun, and S. Goumri-Said, "Engineering of highly mismatched alloy with semiconductor and semi-metallic substituent's for photovoltaic applications," *Curr. Appl. Phys.*, vol. 17, no. 2, pp. 162–168, 2017.

[18] P. Blaha and K. Schwarz, *WIEN2k*, vol. 1. Wien/Austria, 2012.

[19] Roberto.N-G, A. Reyes-Serrato, Alvaro Posada-Amarillas, and D. H. G, "First-principles calculation of the band gap of $Al_xGa_{1-x}N$ and $In_xGa_{1-x}N$," *Rev. Mex. F´ ISICA*, vol. 54, pp. 111–118, 2008.

[20] S. Stepanov, W. N. Wang, B. S. Yavich, V. Bougrov, Y. T. Rebane, and Y. G. Shreter, "Influence of Poisson's ratio uncertainty on calculations of the bowing parameter for strained InGaN layers," *MRS Internet J. Nitride Semicond. Res.*, vol. 6, no. 6, pp. 1–6, 2001.

[21] A. I. Duff, L. Lymperakis, and J. Neugebauer, "Understanding and controlling indium incorporation and surface segregation on $In_xGa_{1-x}N$ surfaces: An ab initio approach," *Phys. Rev. B - Condens. Matter Mater. Phys.*, vol. 89, no. 8, pp. 85307-1–12, 2014.

[22] P. Rinke, M. Winkelnkemper, A. Qteish, D. Bimberg, J. Neugebauer, and M. Scheffler, "Consistent set of band parameters for the group-III nitrides AlN, GaN, and InN," *Phys. Rev. B - Condens. Matter Mater. Phys.*, vol. 77, no. 7, pp. 75202-1–15, 2008.

[23] A. Belabbes, L. C. De Carvalho, A. Schleife, and F. Bechstedt, "Cubic inclusions in hexagonal AlN, GaN, and InN: Electronic states," *Phys. Rev. B - Condens. Matter Mater. Phys.*, vol. 84, no. 12, pp. 125108-1–9, 2011.

[24] S.-H. Wei, X. Nie, I. G. Batyrev, and S. B. Zhang, "Breakdown of the band-gap-common-cation rule: The origin of the small band gap of InN," *Phys. Rev. B*, vol. 67, no. 16, pp. 165209-1–4, 2003.

[25] T. Seddik, R. Khenata, A. Bouhemadou, A. H. Reshak, F. Semari, and B. Amrani, "Prediction study of the structural, elastic and high pressure properties of Yttrium chalcogenide," *Comput. Mater. Sci.*, vol. 49, no. 2, pp. 372–377, 2010.

[26] G. Rehman, M. Shafiq, Saifullah, R. Ahmad, S. Jalali-Asadabadi, M. Maqbool, I. Khan, H. Rahnamaye-Aliabad, and I. Ahmad, "Electronic Band Structures of the Highly Desirable III–V Semiconductors: TB-mBJ DFT Studies," *J. Electron. Mater.*, vol. 45, no. 7, pp. 3314–3323, 2016.

[27] E. Sakalauskas, Ö. Tuna, A. Kraus, H. Bremers, U. Rossow, C. Giesen, M. Heuken, A. Hangleiter, G. Gobsch, and R. Goldhahn, "Dielectric function and bowing parameters of InGaN alloys," *Phys. Status Solidi Basic Res.*, vol. 249, no. 3, pp. 485–488, 2012.

[28] M. Larbi, R. Riane, S. F. Matar, A. Abdiche, M. Djermouni, M. Ameri, N. Merabet, and A. Oualdine, "Ab initio studies of the structural, electronic, and optical properties of quaternary $B_xAl_yGa_{1-x-y}N$ compounds," *Zeitschrift fur Naturforsch. - Sect. B J. Chem. Sci.*, vol. 71, no. 2, pp. 125–134, 2016

[30] M. O. Donnell, E. T. Jaynes, and J. G. Miller, "kramers-Kronig relationship between ultrasonic attenuation and phase velocity," *Acoust. Soc. Am.*, vol. 69, no. May, pp. 696–701, 1981.

[31] Z. Jiao, S. Ma, and Y. Guo, "Simulation of optical function for phosphide crystals following the DFT band structure calculations," *Comput. Theor. Chem.*, vol. 970, pp. 79–84, 2011.

[32] M. Yousaf, F. Inam, R. Khenata, G. Murtaza, A. R. M. Isa, and M. A. Saeed,

"Prediction study of structural , electronic and optical properties of XIn 2 S 4 (X = Hg , Zn) thiospinels under pressure effect," *J. Alloys Compd.*, vol. 589, pp. 353–363, 2014.

[33] R. Ali, S. Mohammad, H. Ullah, S. A. Khan, H. Uddin, M. Khan, and N. U. Khan, "The structural, electronic and optical response of IIA-VIA compounds through the modified Becke-Johnson potential," *Phys. B Condens. Matter*, vol. 410, no. 1, pp. 93–98, 2013.

[34] G. Murtaza, G. Sadique, H. A. Rahnamaye Aliabad, M. N. Khalid, S. Naeem, A. Afaq, B. Amin, and I. Ahmad, "First principle study of cubic perovskites: $AgTF_3$ (T=Mg, Zn)," *Phys. B Condens. Matter*, vol. 406, no. 24, pp. 4584–4589, 2011.

[35] A. Laref, A. Altujar, and S. J. Luo, "The electronic and optical properties of InGaN-based solar cells alloys: First-principles investigations via mBJLDA approach," *Eur. Phys. J. B*, vol. 86, no. 11, pp. 1–11, 2013.

CHAPTER 5
EXPERIMENTAL TECHNIQUES AND DEVICE FABRICATION PROCESS

5.1 INTRODUCTION

Many different techniques are employed to grow III-nitride based heterostructures, the more developed being molecular beam epitaxy (MBE) and metal-organic vapor phase epitaxy (MOVPE).

This chapter describes the overview of the process for the nitridation surface treatment (NST) process, deposition of aluminium nitride (AlN) nucleation layer and AlN/GaN multilayer (ML), and multi quantum well (MQW) using the reactor described in this section. The detailed steps and the flow of the experiment is described concisely.

5.1 METAL ORGANIC CHEMICAL VAPOUR DEPOSITION (MOCVD)

The first MOCVD growth in the world was done back by H.M. Manasevit [1], a chemist working at Rockwell corporation who coined the term “metal-organic” (MO) emphasizing the metal component and further published literatures describing the MOCVD of III-V semiconductors including GaN and AlN, demonstrating the flexibility of this process

Since then, MOCVD have been one of the dominant industrial processes for the fabrication of semiconductor and optoelectronic devices as it offers the advantage of conformal step coverage and deposition over a large scale [2]. The basic working mechanism of MOCVD is to carry precursor materials into a reaction chamber where they are uniformly distributed over the surface of the substrate and decompose via pyrolysis to produce a uniform epitaxial layer of material. The most commonly used source of nitrogen for the III-nitrides is anhydrous ammonia NH_3 , a liquid which has a sufficiently high equilibrium vapour pressure at room temperature which then been delivered directly to the reaction chamber as a gas [3].

The most commonly used MO sources are trimethylaluminium (TMA), trimethylgallium (TMG) and trimetyhilindium (TMI). At room temperature, TMA and TMG are liquids while TMI is solid, in order to preventing them from being delivered directly into the chamber.

The three MO come in sealed metal containers, known as bubblers, because of their pyrophoric nature. In order to transport the MO materials to the reactor, a carrier gas is flowed into the bubblers where it enters through a dip tube submerged in the MO. After “bubbling” through the liquid MO, the carrier gas becomes saturated with the vapour phase MO that is present above the liquid level and carries it into the reactor. The important factor that should be taken into account is the amount of MO that is being delivered into the reactor. The amount of MO delivered into the reactor depends on the equilibrium vapour pressure and typically

calculated in micromoles. The flow rate of MO material in moles/minute out of the bubbler can be calculated as:

$$M_{OM}(mol/min) = \frac{F_c(sccm)}{22{,}400(\ cm^3/mol)} \times \frac{P_V}{P_T - P_V} \quad (5.1),$$

where F_C is the flow rate of the carrier gas, P_T is the total pressure above the MO, and P_V is the vapour pressure of the MO. The vapour pressure of the MO can be modelled for a particular material at absolute temperature T using the parameters a and b by the equation

$$log(P_V) = a - b/T \quad (5.2).$$

Referring to the above equation, the exponential temperature dependence of P_V requires the bubblers to be kept in chilled water baths to avoid fluctuation in temperature which can disturb the constant uniform delivery of MO. The ammonia can be treated as an ideal gas with the molar flow rate calculated using the equation:

$$M_{NH_3}(mol/min) = \frac{F_{NH_3}(sccm)}{22{,}400(\ cm^3/mol)} \quad (5.3).$$

The ratio M_{NH_3}/F_{NH_3} calculated from equations 5.3 and 5.1 is referred as the V/III ratio [4] and is a very useful parameter to describe the growth processes to determine the properties of the deposited material. Hydrogen and nitrogen is the carrier gas that were used in SR-2000 system [5]. It is noted that hydrogen gas is more suitable for thicker layer of deposition while nitrogen is efficiently useful for growing thin layer of material. Nitrogen is also preferred to be used for processes involving indium since hydrogen has a highly negative impact on indium corporation.

5.3 MOCVD Systems for Production

Metal organic chemical vapour deposition (MOCVD) that were used throughout this experiment was from Taiyo Nippon Sanso Corporation (TNSC) SR-2000 model which have the capability of growing up to 4-inch wafer inside the reactor [5]. For the purpose of preliminary serial of experiment and the suitability of budget, the 2-inch silicon (111) wafer were chosen as the substrate throughout this research.

There are basically two common types of MOCVD that depends on the way the gas will flows into the MOCVD chamber, the vertical and horizontal MOCVD. In the vertical

configuration, the gases are introduced from the top inlet, and flow downward perpendicularly onto the substrate placed on the susceptor. While in the horizontal reactor, the gases are flowed horizontally from the three-layered gas injection nozzle inlet and stream tangentially to the growth site [6]. The top nozzle carries hydrogen and nitrogen gas known as gas carry to counter balance the pressure from the other two lower inlets. The middle inlet transports the MO sources to the growth sides by means of carrier gases such as hydrogen and nitrogen gas. Whereas, the bottom inlet carries ammonia to be used as nitride element during the deposition. Figure.5.1 illustrates the incoming gas process entering the horizontal flow reactor through the three-layered gas injection nozzle inlet. The main advantage of using horizontal MOCVD as compared to vertical MOCVD is due to the capability of producing a very uniform and homogenous growth layer on the substrate and thus increasing the yield of deposition per unit area per wafer. These features are extremely important for device property especially in industrial level, where quality and the output were the main key importance indicator (KPI) for the respective company.

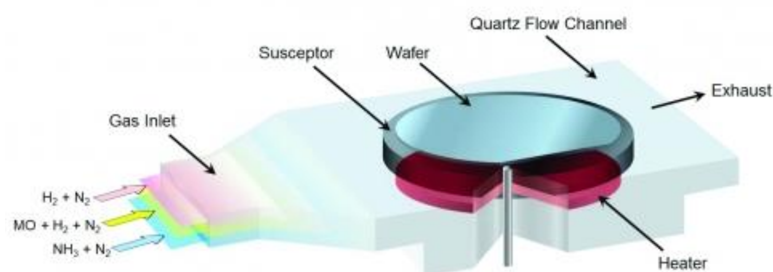

Figure.5.1 Process gases enter the horizontal flow reactor through the three-layered gas injection nozzle inlet [5]

The fundamental necessity for the effective control of MOCVD deposition process lies in the ability of the MOCVD to retain the laminar flow during growth. It is a well-known that, the turbulence gas effect that usually occurred inside the chamber can be avoided under laminar flow condition. This property leads towards a uniform layer of thin film to be deposited. The other factor that contributes to the uniformity of the grown thin film layer is the rotating disk that is connected to the stage inside the reactor where the susceptor is placed upon. It consists of a disk as the susceptor which holds the wafer and rotate at a desirable speed (normally set to 10 rpm) against a steady stream of gases flowing toward it at a normal angle. All the way during growth process, the disk will rotate at a fixed rotation which providing a stable, homogenous and uniform layer of thin film throughout the entire substrate surface. Figure.5.2 shows the schematic illustration of MOCVD process that ensues on the substrate during growth.

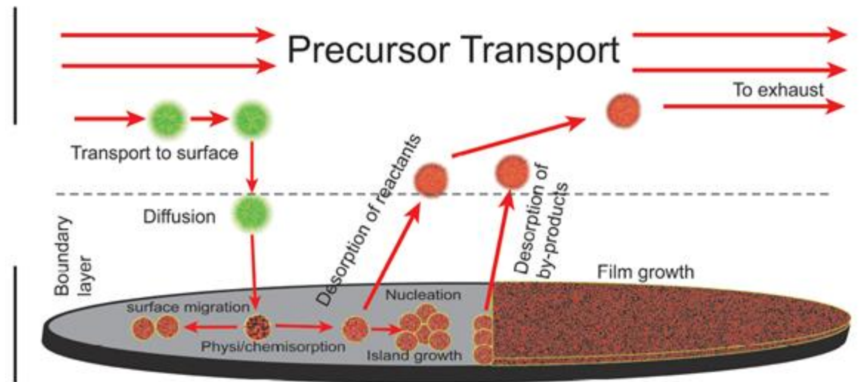

Figure.5.2 schematic illustration of MOCVD process.

5.4 Thin films deposition

5.4.1 Substrate Cleaning

The silicon (111) wafer undergoes the substrate cleaning process before being deposited in metal organic chemical vapour deposition (MOCVD) reactor. There are mainly three subsequent steps in the cleaning process for silicon (111) wafer that is the organic cleaning, the Radio Corporation of America standard cleaning (RCASC) method and lastly the hydrofluoric acid (HF) dip cleaning [7].

5.4.1.1 Organic cleaning method

The silicon (111) wafer were immersed in a contained beaker filled with acetone inside the water bath at temperature of °C for 10 minutes. Consequently, the substrates were rinsed in deionized (DI) water for 5 times. The acetone dip steps were repeated thoroughly for one more time. After the second acetone dip was carried out, the silicon wafer was submerged in propanol to remove the acetone residue on the surface of the substrates. The contained beaker of propanol with the wafer were put in the water bath for 10 minutes before being rinsed with DI water for another 5 times. After that, the wafer was dried using nitrogen blowing on the surface of the silicon wafer.

5.4.1.2 Radio Corporation of America standard cleaning (RCASC) method

This cleaning method was developed by Werner Kern [8] and functioned to remove organic residues and particles on the surface of the silicon wafer. The treatment introduced a thin layer of silicon dioxide (SiO_2) layer on the surface of the silicon with a certain degree of metallic

contamination that shall be removed in the subsequent cleaning steps. The RCASC involved the heating of 65 ml of ammonia solution (NH_4OH) to 70 +/- 5 °C using hot plate. The next step involved the mixing of 65 ml of hydrogen peroxide (H_2O_2) into the solution. The magnetic stirrer was used to stir the solution well.

The indicator for a good mixture of RCASC is the vigorously bubbling effect that can be observed one minute after the stirring process takes place. The silicon (111) wafer were then immersed in the RCASC solution for 10 minutes before being rinsed with distilled water for 5 times. The silicon wafer was then dried using nitrogen blowing. The RCASC solution can be reused within 24 hours at room temperature and 30 minutes at 70 °C.

Step 1 : Organic Cleaning

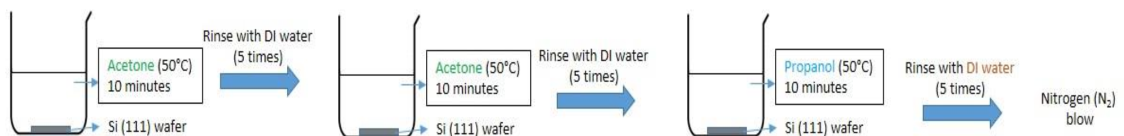

Step 2 : RCASC Cleaning

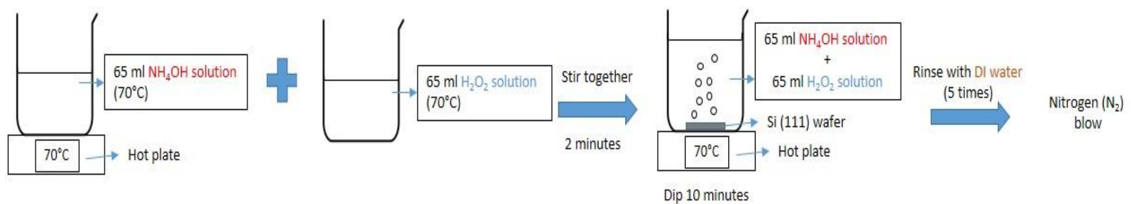

Step 3 : HF Cleaning

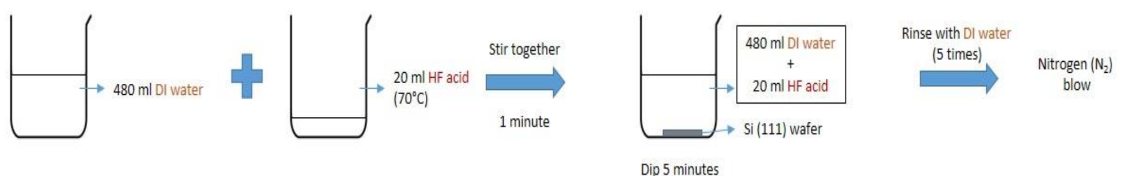

Figure.5.3 Schematic flow of silicon (111) cleaning process.

5.4.1.3 HYDROFLUORIC ACID (HF) DIPPING METHOD

Hydrofluoric acid (HF) is mainly used to remove the native silicon dioxide layer which is formerly produced during the RCASC cleaning method. Due to the reactive nature of HF which easily corrodes glass container, only polypropylene container and syringe were used during the overall process. 480 ml of DI water and 20 ml of HF were stirred slowly for 1 minute to produce

the solution of HF before the silicon (111) wafer were dipped for 5 minutes. The silicon (111) wafer will then undergoes simple wetting test as an indicator for checking the effectiveness of HF dip process. Little deionized (DI) water were poured on the surface of the wafer to check the hydrophobicity of silicon wafer. If the water beads up and rolls off, the surface is hydrophobic and water will not wet it. Since oxide is hydrophilic in nature and pure silicon is hydrophobic, a non-wetting surface suggests an oxide-clean surface. The silicon wafer was then dried with nitrogen blowing before being put into the metal organic chemical vapour deposition (MOCVD) reactor for deposition process. The HF solution may be saved for repeated cleaning process since it does not lose its effectiveness with time. The overall cleaning process takes around 1 hour and 30 minutes and Figure.5.3 shows the schematic flow of silicon (111) cleaning process.

5.4.2 Hydrogen Cleaning (baking)

The process was initiated immediately after the cleaning process by treating the silicon surface using in-situ hydrogen cleaning method inside the MOCVD reactor. The transferring process from the nitrogen blowing site to the metal organic chemical vapour deposition (MOCVD) reactor usually produce a thin layer of native oxide layer due to the high reactivity of oxygen with silicon surface. Thus, to remove the native oxide layer on the surface, hydrogen cleaning was carried out on the surface of the wafer by heating the substrate to a deposition temperature of 1125 °C while flowing hydrogen into the chamber for 10 minutes.

5.4.3 Controlled Preliminary Growth of GaN on Si (111) Substrates

The first preliminary growth parameter of GaN on Si (111) substrates was determined based on several initial commissioning recipes during the installation period of metal organic chemical vapour deposition (MOCVD) equipment at University of Malaya back on February 2014. The growth parameter of each layer is summarized in Table.5.1.

Table.5.1

Growth parameter of each layer of the samples.

Epitaxial Layers	Growth pressure (kPa)	Growth temperature (°C)	V/III ratio	Growth Time (s)
GaN (topmost layer)	13.3	1125	4800	670
AlN/GaN SLS (20 pairs)	13.3	1125	2800	43 (per pair)
AlN nucleation layer (NL) (bottom)	13.3	1000	2800	69

From the above growth parameter, the nitridation and the aluminium nitride (AlN) nucleation layer (NL) were grown at a homogeneous condition of 13.3 kPa and 1000 °C growth temperature. These two layers were considered the first buffer and plays a vital role in producing a good quality of GaN layer. The surrounding pressure was remaining the same throughout the whole growth to inhibit turbulence effect which will deteriorates the uniformity of epitaxial layer during nucleation and growth process. The V/III ratio of each layer is calculated using the equation:

$$M_{NH_3}/F_{NH_3} = V/III\ ratio = \frac{F_{NH_3}(\mu mol/min)}{(FTMA+FTMG+FTMI+FSIH4)(\mu mol/min)} \times \frac{1}{22.4\times10^6} \quad (5.4)$$

Since nitridation surface treatment only involve the flow of ammonia (NH_3) without any flow of group III precursor, the V/III ratio is not considered for that layer. The V/III ratio is one of the main parameter which determines the growth direction and preferred surface orientation of each layer. Furthermore, the crystal quality is closely related with the change in V/III ratio of each layer E. C. Piquette et.al [4] highlighted the influence of V/III ratio in the low temperature aluminium nitride (LT-AlN) interlayer towards the crystal quality of the topmost GaN layer. The author concluded that V/III ratios of the LT-AlN interlayer could strongly affect the crystal quality of GaN, instead of the strain status. Such dependence could be explained in terms of the different LT-AlN surface morphologies originating from the difference of the V/III ratios and the consequential different GaN growth rates in vertical and lateral direction. The LT-AlN grown with optimizing V/III ratio can efficiently prevent the propagation of the thread dislocations in the structure of GaN epitaxial.

A. Dadgar [9] found that both the growth temperature and the thickness of LT-AlN layer could strongly influence the strain relief status and the quality of the GaN layer grown on LT-AlN interlayer respectively.

5.5 The bulk $InGaN$ solar cell

5.5.1 Growth condition

2-inch Si substrate with (111)-crystal orientation has been employed. The substrate was first degreased using the conventional Si substrate cleaning method. The cleaning process was sequentially comprised of an organic cleaning using acetone and propanol before undergone the RCA-1 cleaning and ended up with the hydrofluoric dip for 30 min. The substrate was then

rinsed in the de-ionized water and purged with a nitrogen gun. At the early stage of each growth, the substrate was baked inside the reactor under H2 ambiance at 1125 ◦C for 10 min to remove the native oxide on the substrate surface

In order to prepare the Si substrate for the growth process, the nitridation surface treatment (NST) was accomplished by supplying an ammonia (NH_3) flow of 5 slm at 1000 °C for 400 seconds. After the NST process, a 20-nm aluminium nitride (AlN) nucleation layer was grown at the same temperature followed by growing a 60 pairs of aluminium nitride/gallium nitride (AlN/GaN) multi-layer at 1125 °C for more than 2 hours with thickness of 5nm and 20 nm, respectively, a 500-nm thick of gallium nitride (GaN) epilayer doping N was grown at 1125°C. The bulk layer $InGaN$ was grown at 721°C for supposed thickness 800-nm, with indium incorporation 8%. Finally, a 300-nm thick of P-GaN epilayer was grown atop.

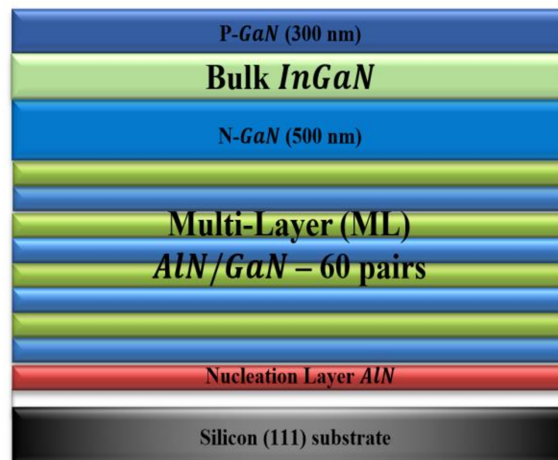

Figure.5.4 shows the growth structure of the bulk $InGaN$ solar cell sample.

5.5.2 Sample Characterization

Cross-section scanning using field effect scanning electron microscopy (FESEM) technique was conducted to further confirm the homogeneity of grown (AlN/GaN) multilayer and the bulk $InGaN$ on Si (111) substrate.

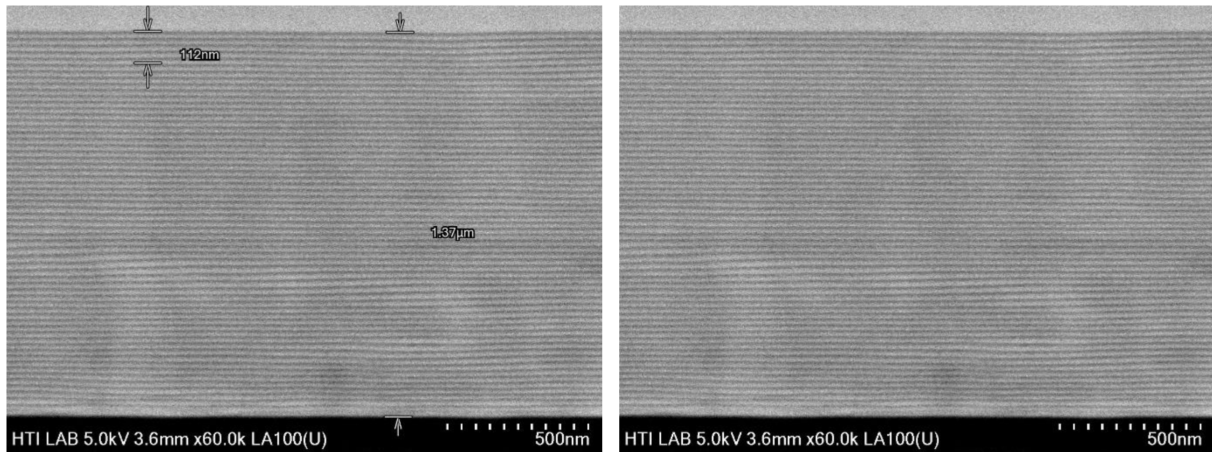

Figure.5.5 shows the cross-section images of the sample for the ML (AlN/GaN).

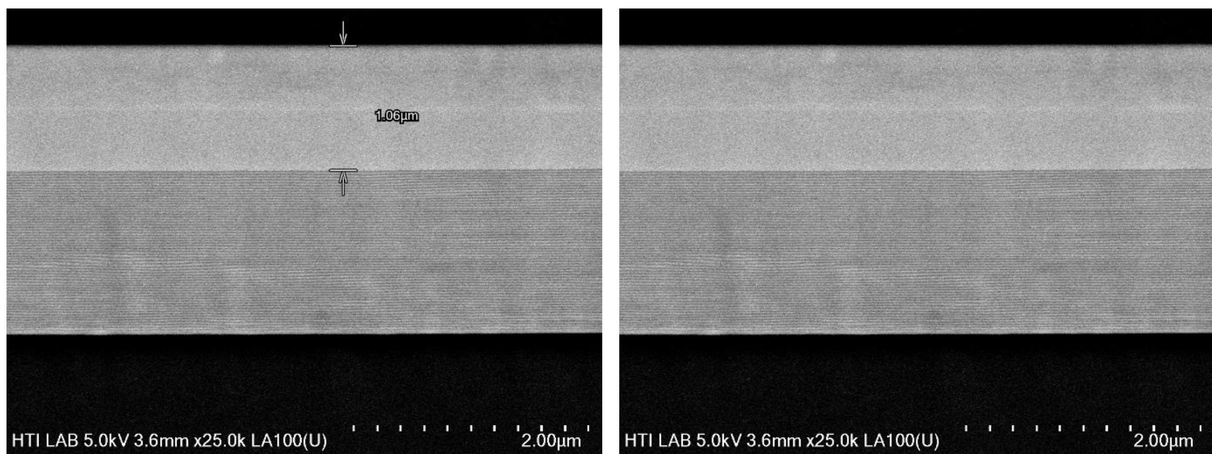

Figure.5.6 shows the cross-section images of the sample for the ML (AlN/GaN) and the bulk $InGaN$

We describe the thickness of each layer from the FESEM images as below:

$5pairs = 112nm \Rightarrow 1\, pair = 22.4\, nm$.

$60pairs = 1370nm \Rightarrow 1pair = 22.8\, nm$.

The P- $GaN + InGaN = 1006\, nm \Rightarrow bulk\ InGaN = 800nm$

The N-$GaN = 500nm$ and the P- $GaN = 200nm$

The $InGaN$ critical layer thickness (CLT) is estimated to be 15 nm for a high quality fully strained epitaxial layer with 10% of In concentration. Above this thickness the crystalline quality and optical performance are degraded. The literature data reports that for $InGaN$ layer thickness exceeding 100 nm with an In concentration above 10%, distinct sublayers of $InGaN$ are observed with distinct In compositions and strain states [10-11].

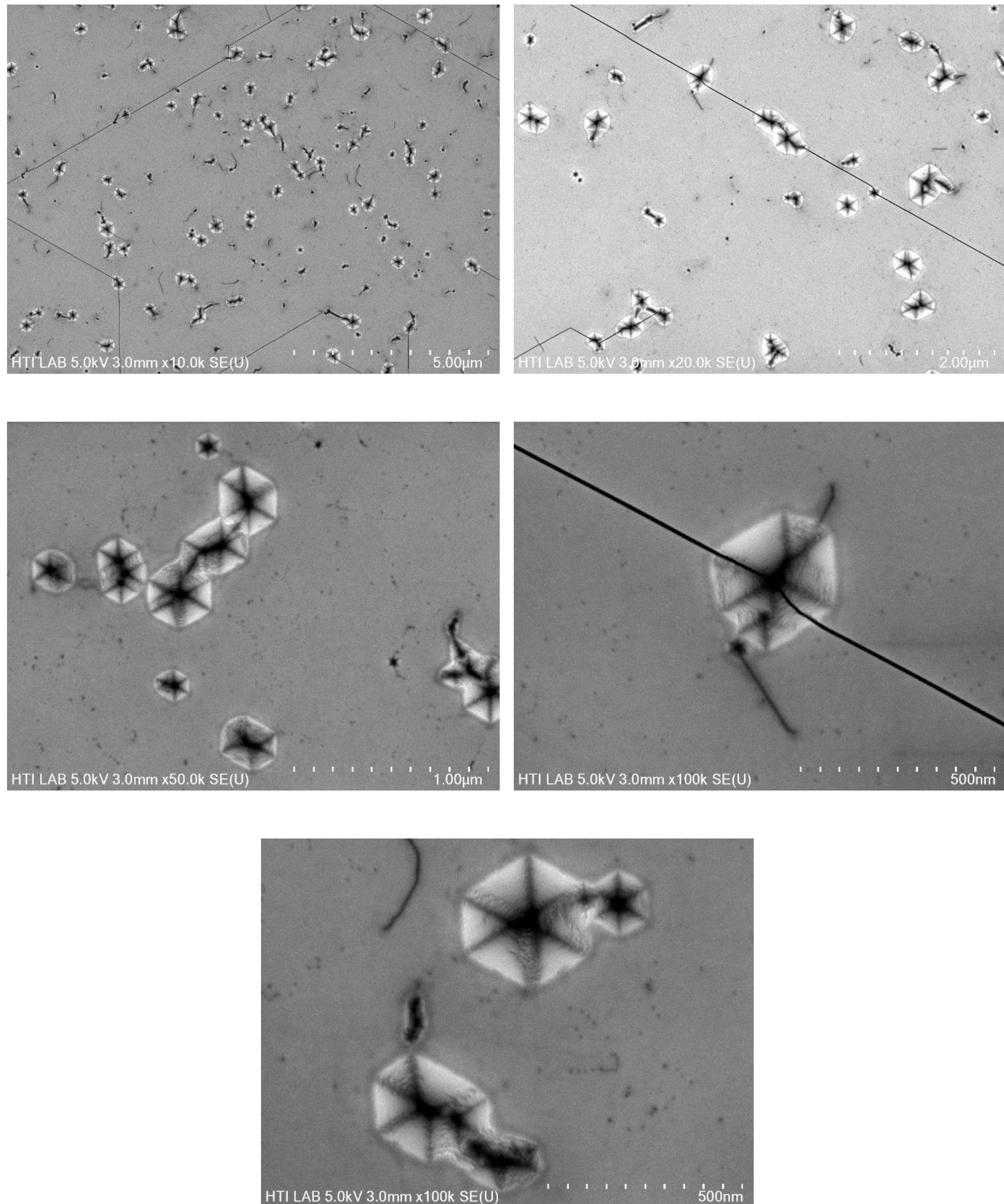

Figure.5.7 shows the FESEM images of the cracks generated on the topmost GaN layer.

The morphological structure of the preliminary sample was not determined by simple observation using naked eyes. The sample appears smooth without crack propagating throughout the sample

The sample was further analysed by surface scanning using field effect scanning electron microscopy (FESEM). Figure.5.7 shows the FESEM image of the cracks generated on the topmost GaN layer for the sample.

According to the cross-sectional images Figure.5.7, the micro-cracks were generated across the sample with most of them propagating near/from the white spot region as can be seen in the images. The white spot is concentrated mainly at the edge of the wafer and contributes toward the generation of cracks. Such condition has often been observed in many publications referring to the phenomenon known as the melt-back etching of silicon. M.Khoury et.al observed the same phenomenon at a higher degree of melt-back etching. According to their experimental results, once the melt-back etching happens, the surface morphology of GaN films will be degraded with the growth going on. Fortunately, insertion of a semi-bulk buffer layer as can eliminate the melt-back etching of GaN/Si [12].

5.6 The semibulk $InGaN$ solar cell

5.6.1 Growth condition

The same growth condition as the previous sample the bulk solar cells. The difference between the two-studied structure is the absorber layer, we change the bulk with the semi-bulk

The semi-bulk absorber layer: 50 periods of $In_{0.8}Ga_{0.92}N/GaN$, both grown at 800 °C,

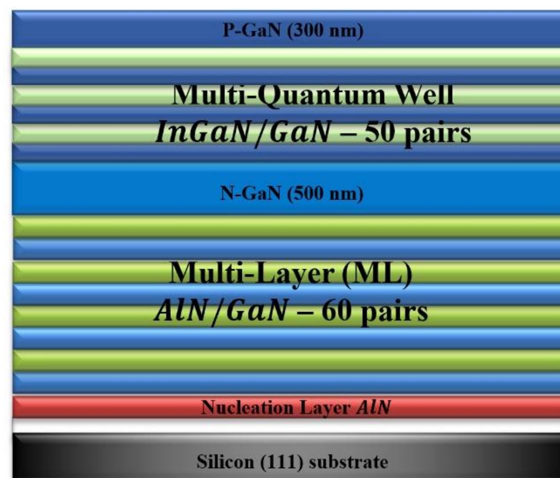

Figure.5.8 shows the schematic growth structure of the semi-bulk $InGaN/GaN$ solar cell sample.

5.6.2 Sample Characterization

The thick $InGaN$ absorber layer with a semi-bulk absorber may overcome the challenge of growing high crystalline quality, single phase absorber layers.

The properties of the deposited sample were examined using the characterization method the field effect scanning electron microscopy (FESEM) of grown the AlN nucleation layer, multi-layer (ML) and multi quantum well (MQW) on Si (111) substrate.

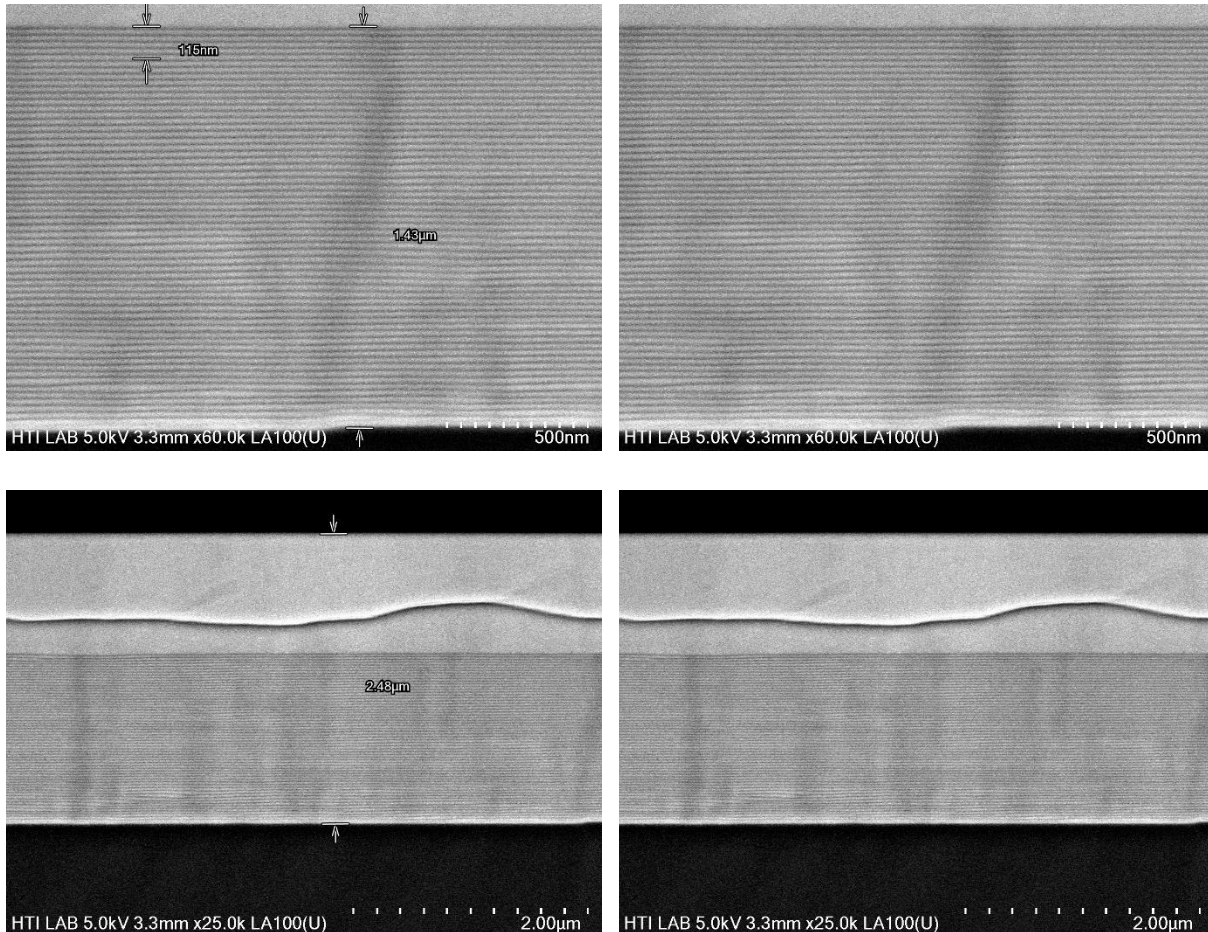

Figure.5.9 shows the cross-section images of the sample for the ML (AlN/GaN) and the semi-bulk $InGaN$ (MQW) with P-GaN growth.

We describe the thickness of each layer from the FESEM images as below:

$5pairs = 115nm \Rightarrow 1\ pair = 23\ nm$.

$60pairs = 1430nm \Rightarrow 1pair = 23.8\ nm$.

The N-$GaN = 500nm$ and the P- $GaN = 200nm$

The semi-bulk $InGaN$ MQW: $50\ pairs = 350nm \Rightarrow 1pair = 7nm.$

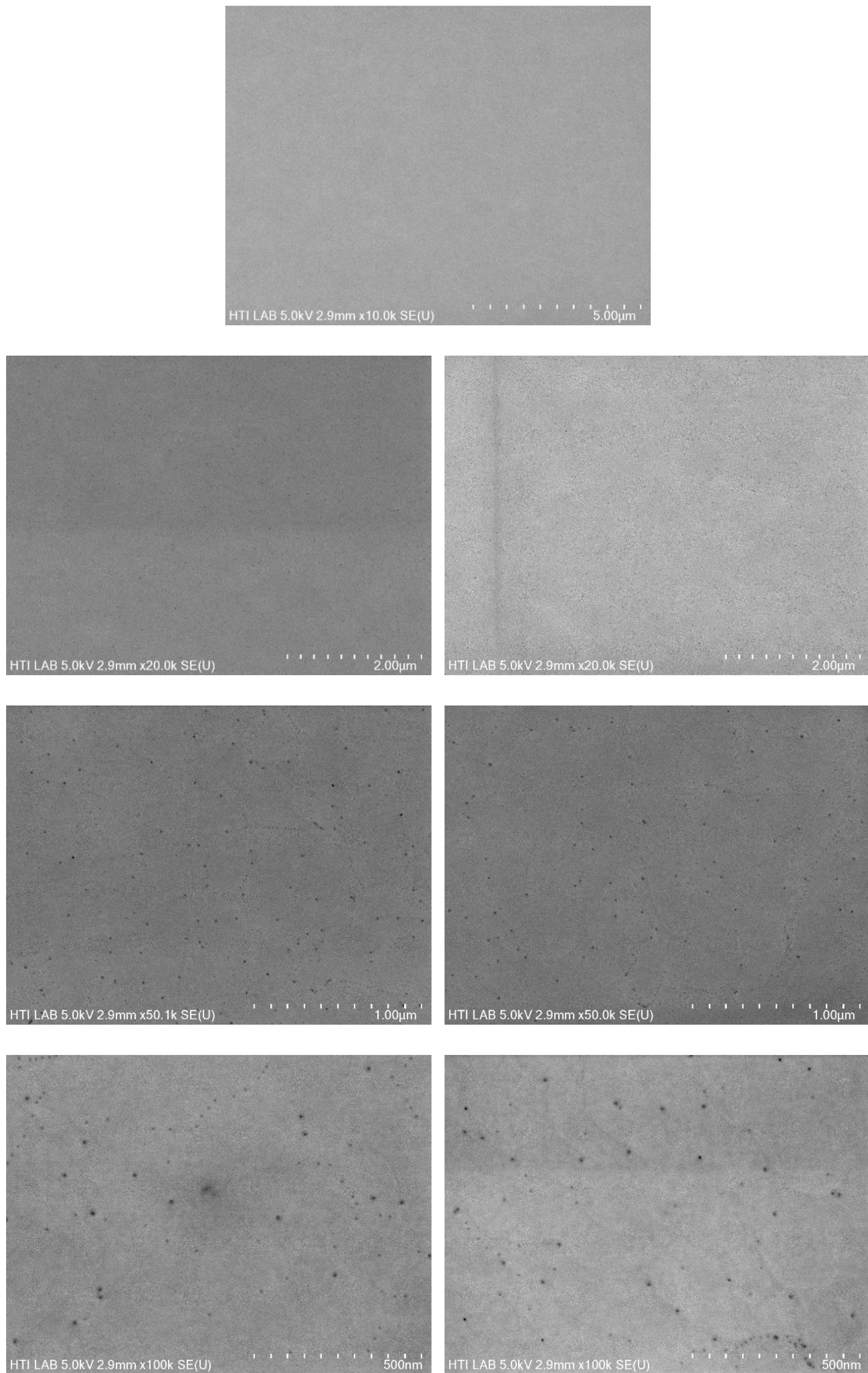

Figure.5.10 shows the FESEM images which shows crack free.

These results have concluded that a high quality of GaN epilayer and MQW absorber layer ($InGaN/GaN$) with a smooth and fine surface grown on Si (111) substrate is successfully achieved, no cracks and pits have been observed shows an abrupt with a smooth layer structure.

5.7 CONCLUSION

The power conversion efficiency (PCE) of $InGaN$ PIN heterojunction solar cells is strongly dependent on the crystalline quality of the $InGaN$ absorber layer, which must be larger than100 nm thick in order to absorb 90% of incident above-bandgap light, we noticed that replacing the thick $InGaN$ absorber layer with a semi-bulk absorber may overcome the challenge of growing high crystalline quality, single phase absorber layers

REFERENCES

[1] H. M. Manasevit, "Single-crystal gallium arsenide on insulating substrates," *Appl. Phys. Lett.*, vol. 12, no. 4, pp. 156–159, 1968.

[2] G. B. Stringfellow, *MOVPE*. Academic Press, 1999.

[3] B. Gil, *Physics of Wurtzite Nitrides and Oxides*. Springer series in Materials Science, 2014.

[4] E. C. Piquette, P. M. Bridger, R. a. Beach, and T. C. McGill, "Effect of Buffer Layer and III/V Ratio on the Surface Morphology of Gan Grown by MBE," *MRS Internet J. Nitride Semicond. Res.*, vol. G3.77, no. 4S1, 1999.

[5] "Metal Organic Chemical Vapor Deposition," TAIYO NIPPON SANSO CORPORATION, 2013.

[6] S. NAKAMURA and S. F. CHICHIBU, *Introduction to Nitride Semiconductor, Blue lasers and Light Emitting diodes*. CRC Press, 2000.

[7] W. Kern and J. E. Soc, "The Evolution of Silicon Wafer Cleaning Technology," *J. Electrochem. Soc.*, vol. 137, no. 6, pp. 1887–1892, 1990.

[8] M. Itano, F. W. Kern, M. Miyashita, and T. Ohmi, "Particle Removal from Silicon Wafer Surface in Wet Cleaning Process," *IEEE Trans. Semicond. Manuf.*, vol. 6, no. 3, pp. 258–267, 1993.

[9] A. Dadgar, "Sixteen years GaN on Si," *Phys. Status Solidi Basic Res.*, vol. 252, no. 5, pp. 1063–1068, 2015.

[10] J. Kim, D. Min, J. Jang, K. Lee, S. Chae, and O. Nam, "Strain relaxation of thick (11-22) semipolar InGaN layer for long wavelength nitride-based device," *J. Appl. Phys.*, vol. 116, no. 16, pp. 163109-1–5, 2014.

[11] M. J. Davies, P. Dawson, F. C. P. Massabuau, R. A. Oliver, M. J. Kappers, and C. J. Humphreys, "The effects of Si-doped prelayers on the optical properties of InGaN/GaN single quantum well structures," *Appl. Phys. Lett.*, vol. 105, no. 9, pp. 92106-1–4, 2014.

[12] M. Khoury, O. Tottereau, G. Feuillet, P. Vennéguès, and J. Zúñiga-Pérez, "Evolution and prevention of meltback etching: Case study of semipolar GaN growth on patterned silicon substrates," *J. Appl. Phys.*, vol. 122, no. 10, pp. 105108-1–7, 2017.

GENERAL CONCLUSION

GENERAL CONCLUSION

At present, III-V compound semiconductors provide the materials basis for a number of well-established commercial technologies, as well as new cutting-edge classes of electronic and optoelectronic devices.

The calculations of structural properties, the electronic (band structure and densities of states DOS), and optical functions for the zinc-blende $Al_xGa_yIn_{1-x-y}N$ compounds ($x = 0.343, 0.468, 0.593$ and $y = 0.375, 0.5, 0.625$) grown on AlN substrate with mismatch less than 2.05%, and the ternary wurtzite alloys $In_xGa_{1-x}N$ with ($x = 0.125, 0.375, 0.625$ and 0.875) grown on GaN substrate are implemented based on the DFT with WC-GGA, LDA and TB-mBJ approximations. The proper structural results, the electronic structures and optical functions of these III-nitrides compounds are performed. The essential results are summarized as follows:

i. The parameters of structural properties of the binary (AlN, GaN, and InN) using WC-GGA in the both structure (zinc-blende and the wurtzite), are in good agreement with the experimental, and the theoretical work values.

ii. The lattice matching condition expression for the $Al_xGa_yIn_{1-x-y}N$ on an AlN substrate was verified, for 3.12% of indium amount. The equilibrium structural properties for the ternaries $In_xGa_{1-x}N$, $Al_{1-y}Ga_yN$ and quaternary $Al_xGa_yIn_{1-x-y}N$ are reasonable comparing with Vegard's law values.

iii. The calculation affords a good explanation of the band structures of the III-nitrides semiconductor alloys ($Al_{1-y}Ga_yN$, $Al_xGa_yIn_{1-x-y}N$ and $In_xGa_{1-x}N$), with good improvement of TB-mBJ results comparing with the Vegard's law calculation. The E_g is in the range of 0.82 to 4.85 eV, identical to the wavelength range 1512.19–255.67 nm. Therefore, the $Al_{1-y}Ga_yN$ and $Al_xGa_yIn_{1-x-y}N$ system is an assuring material for the manufacturing of ultraviolet components (emitters and detectors), while the $In_xGa_{1-x}N$ alloys are implemented in ultraviolet optoelectronics devices and for solar cells application. The densities of states (DOS) of $Al_{1-y}Ga_yN$, $Al_xGa_yIn_{1-x-y}N$ and $In_xGa_{1-x}N$ alloy is explained and the variances between these compounds have been observed.

iv. The dielectric function $\varepsilon(\omega)$, absorption coefficient $\alpha(x)$, reflectivity spectrum $R(\omega)$, and refractive index $n(\omega)$, are calculated for radiation up to 34 eV. We find that the

variations of $\varepsilon_1(0)$ is related to the energy gap, increases when E_g decrease which proved the Penn model.

v. The present optical functions assure that the III-nitrides quaternary zinc-blende alloys ($Al_{0.343}Ga_{0.625}In_{0.031}N$, $Al_{0.468}Ga_{0.5}In_{0.031}N$ and $Al_{0.593}Ga_{0.25}In_{0.031}N$) and the wurtzite $In_{0,125}Ga_{0,875}\,N$, $In_{0,375}Ga_{0,625}\,N$, $In_{0,625}Ga_{0,375}\,N$ and $In_{0,875}Ga_{0,125}\,N$, are suitable for the fabrications of the ultraviolet optoelectronic devices and solar cells.

Silicon has one big disadvantage for today's device layer growth by MOCVD, which requires temperatures above 1000 °C, its low thermal expansion coefficient. The contraction of the group-III-N layer is larger than that of Si leading to cracks in the group-III-N layer when cooling to room temperature already for layer thicknesses around 1 mm, too low for high-quality device fabrication. The inability to grow smooth surface of thick low temperature AlN (LT-AlN) between silicon and gallium nitride layer have limits the extension of research towards developing.

One type of characterization was done on the two-sample of the Solar cells involving the morphological and the structural properties of the topmost GaN layer grown under different growth parameter. In order to confirm the morphological structure of the sample, surface scanning was carried out using field effect scanning electron microscopy (FESEM) measurement.

After analyzing the characterization result of the structures involving both the nitridation layer and the aluminum nitride (AlN) nucleation layer, a new series of experiment will be conducted in the future to describe the solar cells efficiency and the effect of varying the number of period of Indium Gallium nitride/Gallium nitride ($InGaN/GaN$) MQW pairs on the quality of the topmost GaN layer.